KU LEUVEN

FACULTEIT WETENSCHAPPEN

Protecting graphene from atmospheric dopants with the use of an organic self-assembled monolayer

Lander VERSTRAETE

Promotor: Prof. S. De Feyter
KU Leuven

Begeleiders: Dr. K. Mali & Dr. J. Adisoejoso
KU Leuven

Proefschrift ingediend tot het
behalen van de graad van
Master of Science in Chemistry

Academiejaar 2014-2015

Preface

Guided by my interest in science, I decided to study chemistry at KU Leuven. The first two years of my bachelor I did in Kortrijk. Then, I came to Leuven to finish my bachelor program and to carry out my master. During these 5 years as a student, I experienced and enjoyed a lot of scientific and non-scientific activities. Finally, at this point, I present this thesis in fulfillment of the requirements for my master's degree.

First of all, I would like to thank my promotor Prof. S. De Feyter for giving me the opportunity to perform my thesis in this research group. It was a very enriching and nice experience, during which I acquired a better understanding of nano- and surface science. Of course, I would like to thank my two mentors Dr. Kunal Mali and Dr. Jinne Adisoejoso, who guided me throughout this project and who were always ready to help me when needed. Special thanks goes to Roald Phillipson for helping me with the graphene related experiments, to Hans Van Gorp for learning me how to properly use the Cypher AFM, to Joan Teyssandier for the AFM measurements on flakes, and to Peter Walke for the numerous Raman measurements. In general, I would like to thank everyone in the group for all the useful discussions and, most importantly, for the enjoyable stay in this group.

Big thanks goes to my friends for all the nice moments we shared during our studies, to my parents who provided me with the opportunity of an academic education and to my sister Hanne. In particular, I would like to thank my deceased mother, who will always have a special place in my heart. Great thanks also goes to my grandmother Maria, who raised me to the person I am today and on whom I can always fall back.

List of abbreviations and symbols

Abbreviation/ Symbol	***Full name***
°C	Degrees Celsius
μ	Charge carrier mobility
μm	Micrometer
2D	Two-dimensional
3D	Three-dimensional
Å	Ångström
a_0	Carbon-carbon distance in graphene
AFM	Atomic force microscopy
ALD	Atomic layer deposition
BLG	Bilayer graphene
C_{50}	Pentacontane
CCD	Charge-coupled device
cm	Centimeter
CNP	Charge neutrality point
C_{ox}	Oxide capacitance
CVD	Chemical vapor deposition
d_{Ch}	Channel length
DI water	Deionized water
DOS	Density of states
d_{ts}	Tip-sample distance
e	Elementary charge
E	Energy
EBL	Electron beam lithography
E_f	Fermi level
E_g	Band gap energy
EG	Epitaxial graphene
E_{HL}	HOMO/LUMO splitting
EtOH	Ethanol
eV	Electronvolt
FET	Field effect transistor
FFT	Fast Fourier transform
FLG	Few layer graphene
f_T	Cut-off frequency
FWHM	Full width at half maximum
GFET	Graphene field effect transistor
g_{mt}	Terminal transconductance
GNR	Graphene nanoribbon
h	Hour
h-BN	Hexagonal boron nitride
HMDS	Hexamethyldisilazane
HOMO	Highest occupied molecular orbital
HOPG	Highly oriented pyrolytic graphite
I_{2D}	Intensity of the 2D peak
IC	Integrated circuit
I_d	Drain current
I_D	Intensity of the D peak
I_G	Intensity of the G peak
I_{off}	Off-current
I_{on}	On-current
IPA	Isopropylalcohol
I_t	Tunneling current
ITO	Indium tin oxide

ITRS	International Technology Roadmap for Semiconductors
K	Kelvin
kΩ	KiloOhm
LUMO	Lowest unoccupied molecular orbital
m	Meter
M	Molar
MB	Migration barrier
meV	Millielectronvolt
min	Minute
mm	Millimeter
MOSFET	Metal-oxide-semiconductor field effect transistor
mV	Millivolt
n	Charge carrier density
nA	NanoAmpère
nm	Nanometer
OA	Oleylamine
ODA	Octadecylamine
OPA/ODPA	Octadecylphosphonic acid
p.p.m.	Parts per million
PHDA	Phosphonohexa-decanoic acid
PMMA	Poly(methylmethacrylate)
Pos(2D)	Position of the 2D peak
Pos(G)	Position of the G peak
R	Resistance
ref.	Reference
RF	Radiofrequency

RMS	Root mean square
rpm	Rounds per minute
s	Second
S	Subthreshold swing
SAM	Self-assembled monolayer
SLG	Single layer graphene
SPM	Scanning probe microscopy
STM	Scanning tunneling microscopy
THz	TeraHertz
t_{ox}	Oxide thickness
TPa	TeraPascal
TPA	Tetradecylphosphonic acid
UHV	Ultrahigh vacuum
U_t	Applied bias (STM)
V	Volt
V_d	Drain voltage
v_f	Fermi velocity
V_g	Gate voltage
V_{Th}	Threshold voltage
W_{Ch}	Channel width
W	Watt
α	Fine-structure constant
γ_0	Nearest neighbor overlap integral
$\Delta\mu$	Offset in chemical potential
ε	Relative permittivity
ε_0	Vacuum permittivity
ρ	Resistivity
σ	Conductivity

Table of contents

Chapter 1: Introduction

Every once in a while, there comes a scientist with a brilliant idea. Among them is Julius Edgar Lilienfeld, who formalized the first design of a field effect transistor (FET) back in the 1920’s [1]. Today, the FET is at the heart of all integrated circuits (IC), which are mainly silicon-based. The performance of these devices could systematically be improved by scaling down the size of electronic components, giving rise to the famous ‘Moore’s law’ [2]. However, owing to scaling challenges for current FET designs, the semiconductor industry is placing an increased emphasis on alternative materials and designs that may provide improved device performance.

One such material that holds promise to revolutionize modern nanotechnology is graphene, a two-dimensional (2D) allotrope of carbon. More than half a century before its discovery, graphene had already been described theoretically by Wallace, revealing its astounding electronic characteristics [3]. However, being a 2D material, it was believed to be thermodynamically unstable in a 3D world, as indicated by the theory of Peierls and Landau [4], [5]. Finally, in 2004, graphene revealed itself to the keen eye of Konstantin Novoselov and his promotor Andre Geim [6], for which they were awarded the 2010 Nobel Prize in Physics [7]. This discovery opened up an entirely new research field, in which thousands of researchers over the whole world try to unveil and understand all that graphene has to offer.

Along with the discovery of graphene came the first realization of a graphene FET (GFET) [6]. The most compelling features of graphene from a device perspective are its atomically flat nature and its excellent carrier mobility. Today, graphene has been included in the International Technology Roadmap for Semiconductors (ITRS), confirming the belief that graphene might play an important role in future electronic applications.

However, integration of graphene in FETs also elicits severe challenges, such as opening a sizeable and well-defined band gap. Moreover, long-term device stability and robustness during processing will be critical for the success rate of graphene in commercial applications. Unfortunately, graphene proves to be extremely sensitive to external conditions such as: ambient air, underlying substrate and fabrication related chemicals (*e.g.* organic solvents, resist residues), resulting in unintentional doping, reduced carrier mobility, and hysteretic behavior in transfer characteristics. Solving these issues will require the design of a proper substrate combined with a suitable surface passivation method for graphene.

This brings us to the current project, which is part of a collaboration between the De Feyter group of KU Leuven – University of Leuven and the 2D materials research group of IMEC (Interuniversity Microelectronics Center), Leuven. The aim of this thesis is to investigate if and how graphene can by passivated by using an organic self-assembled monolayer (SAM). The advantage of using a SAM as a surface passivation layer is the versatility of layers that can be employed, enabling us to choose a molecular system compatible with graphene, *i.e.* preserving the high quality pristine graphene characteristics. The expectation is that this approach will yield improved, long-term GFET performance.

This first chapter aims at providing the necessary background information needed to understand the context and significance of the addressed problem and to enable us to properly understand the approach followed and the experiments performed. The first section is an introduction to the structure and properties of graphene, highlighting its peculiar electronic properties. The second section then describes the basic operation of a FET, placing the emphasis on the implementation of graphene as a channel material. The third and penultimate section reveals the details of charge transfer doping of graphene, placed in the context of unintentional doping and other unintentional effects. Finally, the fourth section discusses functionalization of graphene, with a focus on surface passivation.

1.1 Introduction to graphene

Graphene is an atomically flat sheet of carbon atoms arranged in a honeycomb network. Due to its structure, it is considered to be the fundamental building block for all other graphitic material, such as graphite, carbon nanotubes, and fullerenes, as schematically depicted in Figure 1.1 [8]. As a result of its particular structure, graphene possesses some extraordinary characteristics such as its mechanical, thermal, optical and electronic properties, which seem to hold promise for many possible applications [8]–[10].

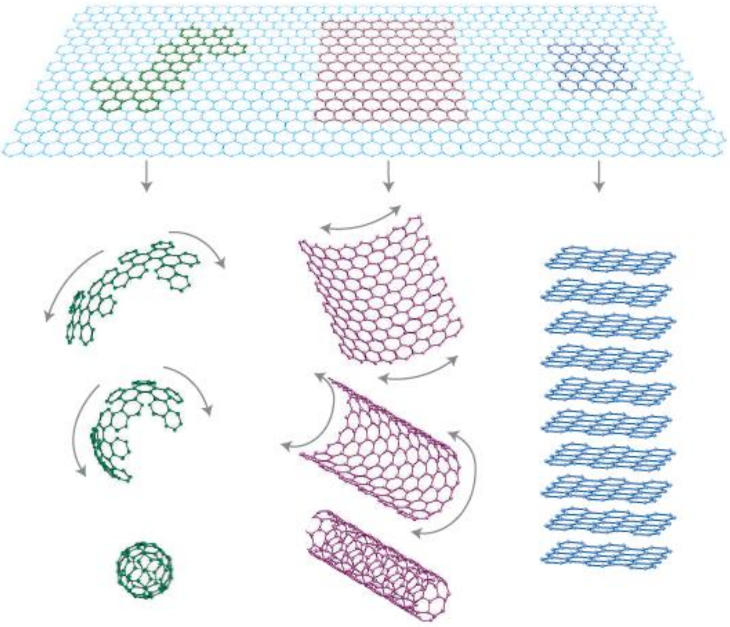

Figure 1.1. *Graphene, being a 2D network of carbon atoms, is considered as the fundamental building block for all other graphitic material. It can be wrapped up into fullerenes (left), rolled up into carbon nanotubes (middle) or several graphene layers can be stacked on top of each other forming graphite (right). (Adapted from ref.* [8]*)*

1.1.1 Atomic structure

Central to the understanding of the distinctive properties that are ascribed to graphene is its atomic structure. As was pointed out above, graphene is a 2D network of carbon atoms, often referred to as a honeycomb network. In fact, the atomic structure of graphene, as shown in Figure 1.1, is an idealized one, as perfect 2D crystals cannot exist in the free state [11]. This argument was worked out by Peierls and Landau more than 70 years ago [4], [5], showing that thermal fluctuations should result in melting of the 2D structure at any finite temperature. Therefore, a more realistic model of graphene's atomic structure is shown in Figure 1.2a, where the graphene sheet exhibits intrinsic microscopic corrugations that are essential for its thermodynamic stability.

The basic unit of this 2D network is a sp^2 hybridized carbon atom (Figure 1.2b). Three sp^2 orbitals lie in the XY-plane separated by an angle of 120° and perpendicular to this plane of sp^2 orbitals is the remaining p_z orbital. As a result of the tetravalency of carbon and because of electron promotion before hybridization of the orbitals, each of the three sp^2 orbitals as well as the p_z orbital contain one electron. The sp^2 hybridized orbitals of neighboring carbon atoms overlap in the XY-plane to form σ-type bonds that give rise to the carbon network with 6-fold symmetry. The p_z orbitals on the other hand form conjugated π-type bonds that give rise to a filled π-band (valence band) and an empty π*-band (conduction band), responsible for graphene's peculiar electronic properties.

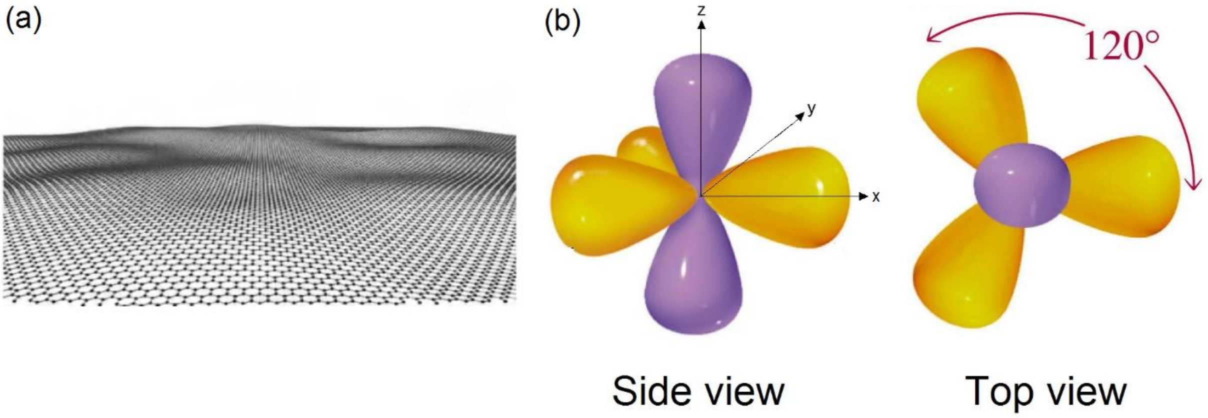

Figure 1.2. *(a) Atomic model of a corrugated graphene sheet. The out-of-plane deformations reach 1 nm. (Adapted from ref.* [11]*) (b) Orbital structure of a sp^2 hybridized carbon atom, showing the three sp^2 hybrid orbitals (yellow) and the remaining p_z orbital (purple). The top view clearly illustrates the angle of 120° separating the sp^2 orbitals.*

The hexagonal lattice structure of graphene is shown in Figure 1.3a. The unit cell of this lattice is a rhombus (grey) containing two non-equivalent carbon atoms (A and B). These non-equivalent carbon atoms can be considered as constituting two triangular sublattices (black and white lattice points). In Cartesian coordinates, the basis vectors of the unit cell can be written as:

$$\vec{a}_1 = \begin{pmatrix} \sqrt{3}a/_2 \\ a/_2 \end{pmatrix}, \qquad \vec{a}_2 = \begin{pmatrix} \sqrt{3}a/_2 \\ -a/_2 \end{pmatrix}, \qquad \text{Eq. (1)}$$

in which a = $\sqrt{3}$a$_0$, a$_0$ being the carbon-carbon distance in graphene (1.421 Å). The reciprocal lattice of graphene is shown in Figure 1.3b and the reciprocal basis vectors are given by:

$$\vec{b}_1 = \begin{pmatrix} 2\pi/_{\sqrt{3}a} \\ 2\pi/_a \end{pmatrix}, \qquad \vec{b}_2 = \begin{pmatrix} 2\pi/_{\sqrt{3}a} \\ -2\pi/_a \end{pmatrix}, \qquad \text{Eq. (2)}$$

in which the same convention for a is used as above. Figure 1.3b also shows the first Brillouin zone together with the high symmetry points Γ, M, K and K'. The reciprocal lattice is constructed in such a way that each lattice point of the reciprocal lattice corresponds to a specific set of lattice planes of the crystal in real space. This geometrical construction is of particular importance to describe diffraction patterns and is often used to depict the electronic band structure of a material.

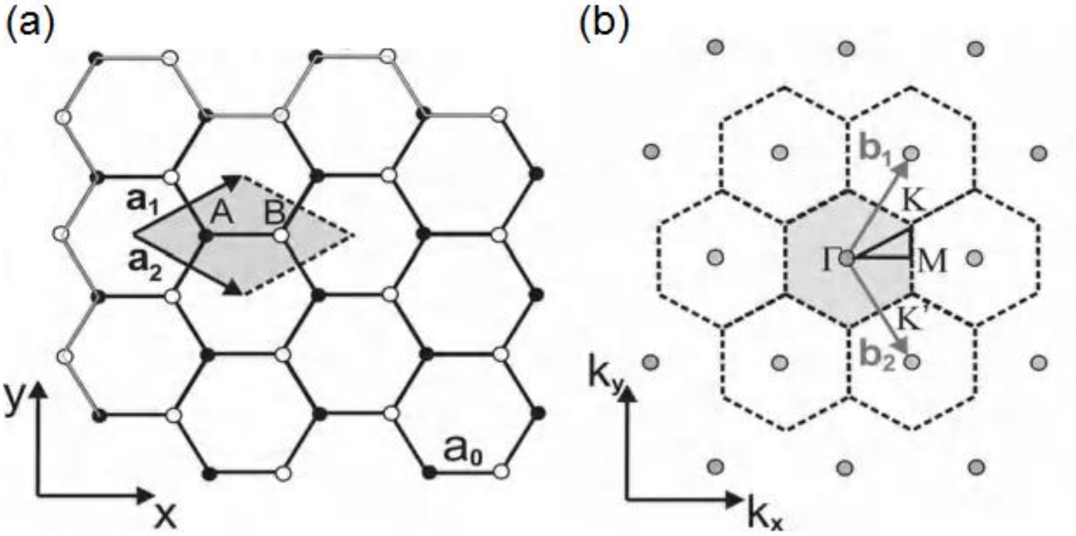

Figure 1.3. *(a) Hexagonal lattice structure of graphene showing the unit cell (grey) described by the basis vectors* $\vec{a}_1$*and* $\vec{a}_2$*. The unit cell contains two non-equivalent lattice points A and B that constitute two triangular sublattices (black and white lattice points). (b) Reciprocal lattice showing the reciprocal basis vectors* $\vec{b}_1$*and* $\vec{b}_2$*, the high symmetry points Γ, M, K and K' and the first Brillouin zone (grey). (Adapted from ref.* [12]*)*

1.1.2 Electronic structure

As mentioned above, the band structure of graphene consists of a filled π-band and an empty π*-band. An analytical description of this band structure can be obtained by using the nearest neighbor tight-binding approach in which the band structure is calculated considering one π-electron per atom and taking into account only interactions between π-electrons of nearest neighbors. This results in the following (approximate) dispersion relation [12]:

$$E^{\pm}(\vec{k}) = \pm\gamma_0 \sqrt{1 + 4cos\frac{\sqrt{3k_x a}}{2} cos\frac{k_y a}{2} + 4cos^2\frac{k_y a}{2}}, \qquad \text{Eq. (3)}$$

in which a is defined as above and γ_0 is the nearest neighbor overlap integral, obtained by fitting experimental data. The best description of the π- and π*-band at the K point is obtained for a fitted value of γ_0 between -2.5 and -3 eV [13]. The band structure described be Eq. (3) is plotted in Figure 1.4, which shows that graphene consists of a lower energy π-band and a higher energy π*-band meeting at the high symmetry K and K’ points of the reciprocal lattice (blue dots).

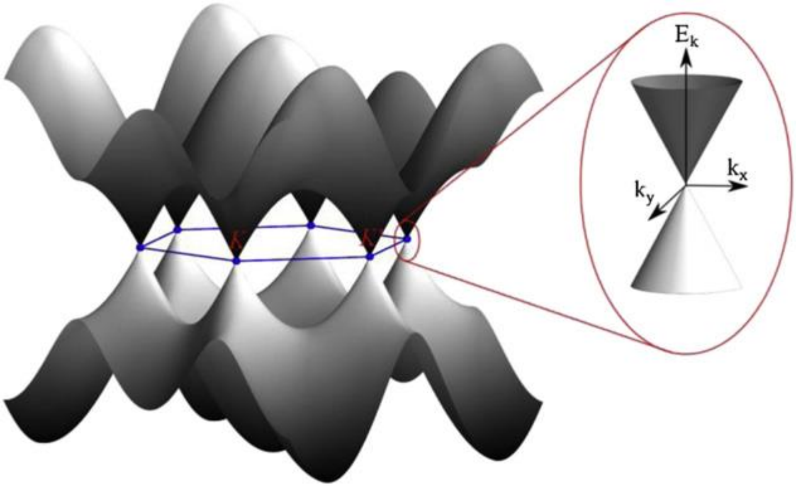

Figure 1.4. *Band structure of graphene calculated using the nearest neighbor tight-binding approach. The π- and π*-band meet at the high symmetry K and K’ points marked with a blue dot. The inset shows a magnification of the dispersion relation around a Dirac point indicating its linear nature at small values of $\vec{k}$. (Adapted from ref.* [12]*)*

In pristine graphene, each carbon atom contributes one electron to the π/π*-band structure which, at zero temperature, results in a completely filled π-band and an empty π*-band, called valence and conduction band respectively. Consequently, the Fermi level of graphene is situated at the point where the valence and conduction bands meet. These points are known as Dirac points or charge neutrality points (CNPs) and are characterized by a density of states (DOS) equal to zero. Graphene is therefore best described as a zero band gap semiconductor.

For small values of $\vec{k}$, the dispersion relation close to the Dirac points (K or K') can be expanded to:

$$E^{\pm}(\vec{k}) = \hbar v_F |\vec{k} - K|, \qquad \text{Eq. (4)}$$

in which $v_F = \sqrt{3}\gamma_0 \, {}^{a}\!/_{2\hbar}$ is the Fermi velocity given by a value of $v_F \cong 1 \cdot 10^6$ m/s. As indicated by Eq. (4) the dispersion relation close to the Dirac points is linear, as can also be seen in Figure 1.4. In this region of linear energy dispersion the band structure is described by two inequivalent Dirac cones situated at the high symmetry K and K' points of the reciprocal lattice.

1.1.3 Electronic properties

The worldwide interest in graphene mainly originates from the extraordinary electronic properties that are ascribed to this material. For high quality graphene, ballistic transport[1] of charge carriers over micron distances is reported [14]. In general, the electronic quality is assessed by the mobility, μ, of the charge carriers. The electron mobility (μ_e) is related to the electrical conductivity (σ) or resistivity (ρ) via:

$$\sigma = \rho^{-1} = ne\mu_e, \qquad \text{Eq. (5)}$$

in which n is the electron density and e is the elementary charge. This formula is only valid when the conduction is entirely due to electrons. When the charge is conducted by holes, the electrical conductivity is defined in an analogous manner simply by replacing μ_e by μ_h in Eq. (5) and by defining n as the hole density.

The actual mobility value for graphene differs significantly depending on the graphene source and/or external conditions (*e.g.* substrate, and temperature). For instance, for single layer graphene (SLG) on a SiO_2 substrate, values in the order of 10,000 cm^2/(V.s) are reported at low temperatures [15], for epitaxial graphene a value of 27,000 cm^2/(V.s) has been measured [16], using hexagonal boron nitride (h-BN) as a substrate, devices with mobilities of 60,000 cm^2/(V.s) have been achieved [17], and for suspended graphene values exceeding 200,000 cm^2/(V.s) are described [18].

---

[1] Ballistic transport refers to conduction of charge carriers through a medium with limited resistivity caused by scattering events. This is typically the case when the mean free path of the charge carriers is much longer than the effective dimensions of the medium (*e.g.* the channel length in a FET).

Systematically higher mobility values are obtained by reducing charge carrier scattering. The dominant scattering mechanism in graphene devices is most likely caused by Coulomb scattering at charged impurities situated near the interface between the graphene layer and the substrate [19], [20]. Furthermore scattering at substrate phonons adds to the fact that the mobility values for graphene residing on different substrates is limited. When eliminating the substrate, such as for freely suspended graphene, the mobility is only limited by intrinsic phonon scattering, which sets a fundamental limit to the mobility that can be obtained in graphene-based devices at room temperature [20], [21]. Other scatter sources are lattice defects and ripples in the graphene sheet.

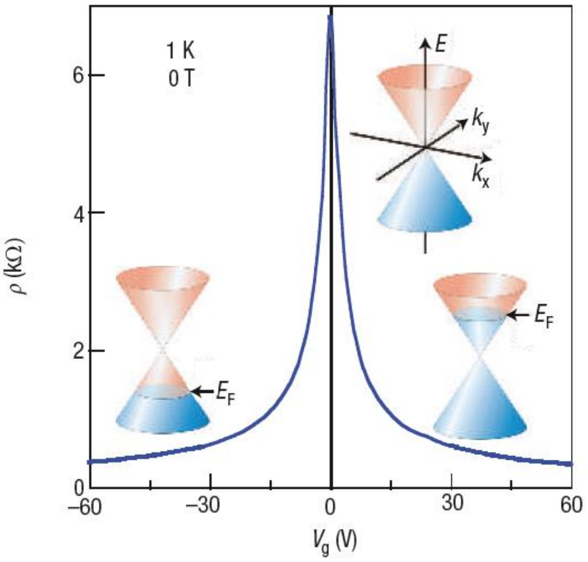

Figure 1.5. *Illustration of the ambipolar electric field effect in graphene. When a gate voltage (V_g) is applied to a graphene field effect device, the Fermi level (E_F) can be tuned into the valence band (left) or into the conduction band (right). In both cases the resistivity (ρ) decreases with increasing gate voltage due to a higher number of mobile charge carriers. (Adapted from ref.* [8]*)*

Of particular importance for graphene-based electronic devices is the so-called ambipolar electric field effect [6]. This effect refers to the fact that the nature and density of charge carriers in graphene field effect devices can be tuned by the gate voltage. This is illustrated in Figure 1.5, where the Fermi level is shifted either into the valence band (where charge is carried by holes) or into the conduction band (where charge is carried by electrons) depending on the particular gate voltage. The more the Fermi level is shifted away from the Dirac point, the higher the number of mobile charge carriers, and consequently the higher the conductivity or the lower the resistivity. Also, the perfect electron-hole symmetry originating from the conical band structure is remarkable.

It is noteworthy that when the Fermi level is at the Dirac point, the conductivity is at a minimum and it is not zero as one would expect based upon a DOS equal to zero. Several studies demonstrated a minimal conductivity on the order of a few $e^2/\hbar$ [22], [23]. However, there is still no consensus on whether this minimal conductivity is intrinsic to graphene or is due to technical limitations of the experiments.

1.1.4 From graphene to graphite

The electronic properties of graphene are strongly dependent on the number of graphene layers, evolving gradually from a zero band gap semiconductor for SLG to a semimetal with a band overlap of around 41 meV for graphite [24]. In general, a distinction is made between SLG, bilayer graphene (BLG) and few layer graphene (FLG). When the number of layers exceeds 10, the term graphite is used as the electronic properties become essentially the same as for bulk graphite.

Not only the number of layers determines the particular characteristics of the electronic band structure, but also the way in which these layers are stacked. Generally, three different stacking sequences can be discerned: simple hexagonal (AAA), so-called Bernal stacking (ABAB) and rhombohedral (ABC). Furthermore, the term turbostratic or disordered graphite is used for graphite with no preferred stacking order. The stacking sequence of Bernal and rhombohedral stacked graphene is shown in Figure 1.6.

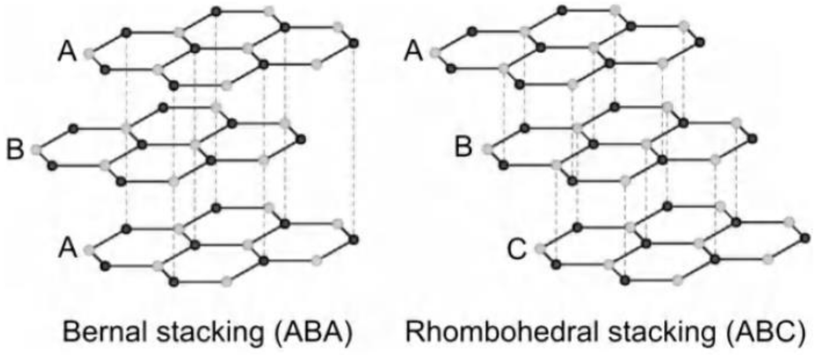

Figure 1.6. *Bernal stacking (left) and rhombohedral stacking (right). For the Bernal stacking sequence the third layer is positioned exactly above the first layer, while for rhombohedral stacking the third layer is displaced with respect to the two lower lying layers. (Adapted from ref.* [12]*)*

1.1.5 Other properties

From a chemical point of view graphene is relatively inert, as can be expected based on the strong conjugated carbon-carbon bonds. Chemical functionalization, however, is possible and one of the first examples was the conversion of graphene to graphane when exposed to atomic hydrogen [25]. The high bond strength in graphene also results in outstanding mechanical properties [26]. It can be stretched elastically up to more than 20 % and recently a Young's modulus as large as 1.48 TPa has been estimated using Raman scattering, exceeding values for every other material [27]. Furthermore, also the thermal and optical properties of graphene are remarkable, with for instance, a thermal conductivity up to 5000 W/(m.K) [28] and an optical absorption matching exactly $\pi\alpha \cong 2.3$ %, in which α is the fine-structure constant[2] [29]. The stunning characteristics of graphene are by no means limited to the aforementioned ones and the combination of all these striking properties in one material justify that graphene is considered as one of the most promising materials for the future of nanotechnology.

1.1.6 Applications

A number of different applications have been proposed taking advantage of the exceptional features of graphene**.** One of the important applications of graphene is its use as a channel material in FETs. Because of its low sheet resistance and high transmittance, graphene has also been suggested for transparent conductive electrodes in solar cells [30]. Currently an indium tin oxide (ITO) film is used for this purpose, but this material is becoming expensive because of shrinking supplies of In. The same is true for ITO based organic light emitting diodes [31]. Furthermore, due to its 2D nature, the properties of graphene are extremely sensitive to the environment. This attribute is particularly beneficial in sensor applications. Schedin *et al.* argued that graphene-based sensors exhibit ultrahigh sensitivity such that the adsorption of individual gas molecules could be detected [32]. Other possible applications include flexible electronics, supercapacitor devices for energy storage, interconnects and

---

[2] The fine-structure constant is a fundamental physical constant describing the electromagnetic interaction strength between elementary charged particles. It is a dimensionless constant with a contemporary accepted value of $7.29735257 \cdot 10^{-3}$.

many more. A good overview of proposed applications is given in ref. [10]. The following section describes the application of graphene in FETs.

1.2 (Graphene) field effect transistors

The first design of a FET dates back to 1925 when Julius Edgar Lilienfeld filed a patent for his transistor device [1]. Since then, the electronic industry has come a long way, and the FETs that are commonly produced now are called metal-oxide-semiconductor FETs (MOSFET). However, owing to scaling challenges for current MOSFET designs, the semiconductor industry is placing an increased emphasis on alternative materials such as for instance graphene, which holds a lot of promise because of its atomically flat nature and excellent carrier mobility.

1.2.1 Operation principle of a MOSFET

A MOSFET typically consists of a gate electrode, a channel region connecting source and drain electrodes and an insulating layer separating the gate from the channel (Figure 1.7). The operation principle is based on controlling the channel conductivity, and consequently the drain current, by applying a voltage between the gate and the source [33]. In this way the MOSFET basically acts as a current switch.

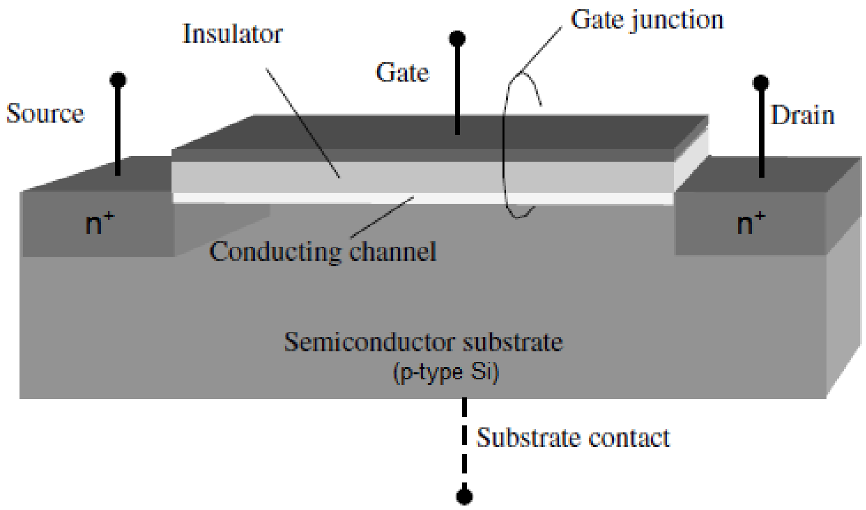

Figure 1.7. *Schematic representation of n-channel Si MOSFET. The main features comprise two terminal electrodes, source and drain, embedded in a p-type Si substrate. The gate is electrically isolated from the substrate by an insulator (gate oxide). When the applied gate voltage exceeds the threshold voltage a conductive channel of minority carriers is formed. (Adapted form ref.* [34]*)*

Figure 1.7 shows the basic design of a conventional n-channel Si MOSFET. Here, source and drain are made of heavily n-doped Si regions, embedded in a p-type Si substrate. The gate oxide used to be a native SiO_2 layer, but as its thickness has decreased steadily over the years in order to increase the gate capacitance, it is nowadays more convenient to employ high-κ dielectrics which allow for less leakage current. When a positive voltage is applied to the gate, holes are repelled from the gate oxide – substrate interface and a depletion region is formed underneath the gate oxide. By applying systematically higher gate voltages, at some point, a situation is reached where the electron concentration exceeds the doping density in the semiconductor, *i.e.* strong inversion regime [34]. In this regime a significant conducting sheet of inversion charge is formed underneath the gate, which is called the channel. The voltage at which this strong inversion regime is entered is called the threshold voltage (V_{Th}), and can be regarded as the voltage at which the MOSFET is on the verge of switching on [33]. In short, the possibility to create and modulate a sheet of minority carriers at the gate oxide – substrate interface is the basis for operation of a MOSFET.

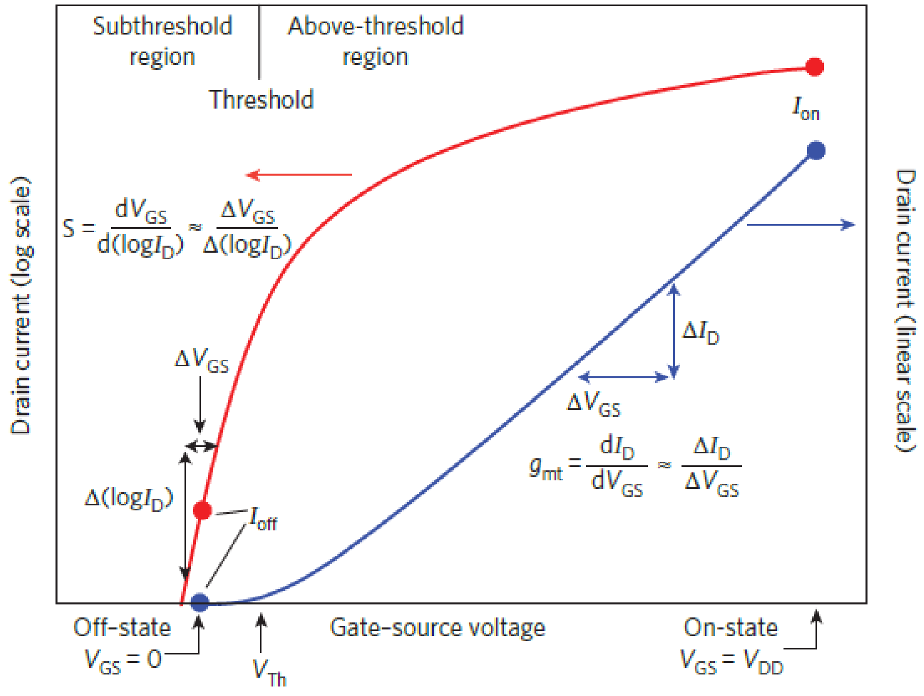

Figure 1.8. *Transfer characteristics for a MOSFET showing the drain current (I_D) as a function of applied gate voltage (V_{GS}). When no voltage is supplied to the gate, the transistor is said to be in the off-sate, where only a small leakage current (I_{off}) flows between source and drain. When the maximum voltage (V_{DD}) is supplied to the gate, the transistor is in the on-state and a large current (I_{on}) flows. At intermediate gate voltage, the threshold voltage (V_{Th}) defines the onset of strong inversion. The*

subthreshold swing (S) defines the switch-on characteristics and the terminal transconductance (g_{mt}) characterizes the change in I_D for a given change in V_{GS}. (Adapted from ref. [33]*)*

Figure 1.8 shows the typical transfer characteristics of a MOSFET, indicating the subthreshold and above-threshold regime. For operating logic processes, a transistor is typically switched between the on-state (characterized by a large on-current, I_{on}, and $V_{GS} = V_{DD}$, where V_{DD} is the maximum voltage supplied to the gate) and the off-state (characterized by a small off-current, I_{off}, and $V_{GS} = 0$ V) [33]. Useful measures to assess the switching behavior between these two regimes are the sub-threshold swing (S) and the terminal transconductance (g_{mt}), which are defined as in Figure 1.8. These two measures also reflect the different dependence of drain current on gate voltage on either side of the threshold voltage. In the subthreshold regime, the drain current increases exponentially with increasing gate voltage. Above the threshold voltage, on the other hand, the drain current scales linearly with gate voltage. Another important measure of transistor characteristics is the on/off ratio (I_{on}/I_{off}). For Si MOSFETs an on/off ratio between 10^4 and 10^7 is required, and any successor to the Si-based devices should at least have comparable values [35].

In the preceding paragraph we have discussed FETs for use in digital logic, where the on-off switching behavior is at the heart of performing logic operations. Alternatively a FET transistor can also be used as an analogue amplifier for radiofrequency (RF) applications. In this mode of operation a small RF-signal that is to be amplified is supplied to the gate of a FET in the on-state and in this way modulates the channel current. This current is subsequently converted to a voltage signal on passing through a load resistor [36]. As a consequence, switch-off is not a prerequisite for RF applications [33]. A useful and often reported measure for the performance of these devices is the cut-off frequency, f_T, which is defined as the frequency at which the current gain reaches unity and which is actually the highest frequency at which the FET is useful in RF applications [33].

1.2.2 Graphene field effect transistors

The first realization of a GFET was demonstrated by Novoselov *et al.* in their pioneering paper of 2004 [6]. Their design consisted of a back-gated FET structure on a 300 nm SiO_2 substrate layer (Figure 1.9a). Although such back-gated designs are useful for proof of concept, they are impractical for realistic applications because of large parasitic capacitances and poor gate control [36]. Alternatively, top-gated devices

(Figure 1.9b) are much more convenient and the first top-gated GFET was demonstrated in 2007 [37]. The deposition of a top-gate initially resulted in a significant degradation of carrier mobility, but recent reports of top-gated graphene devices show that high mobilities can also be achieved for top-gated GFETs [38].

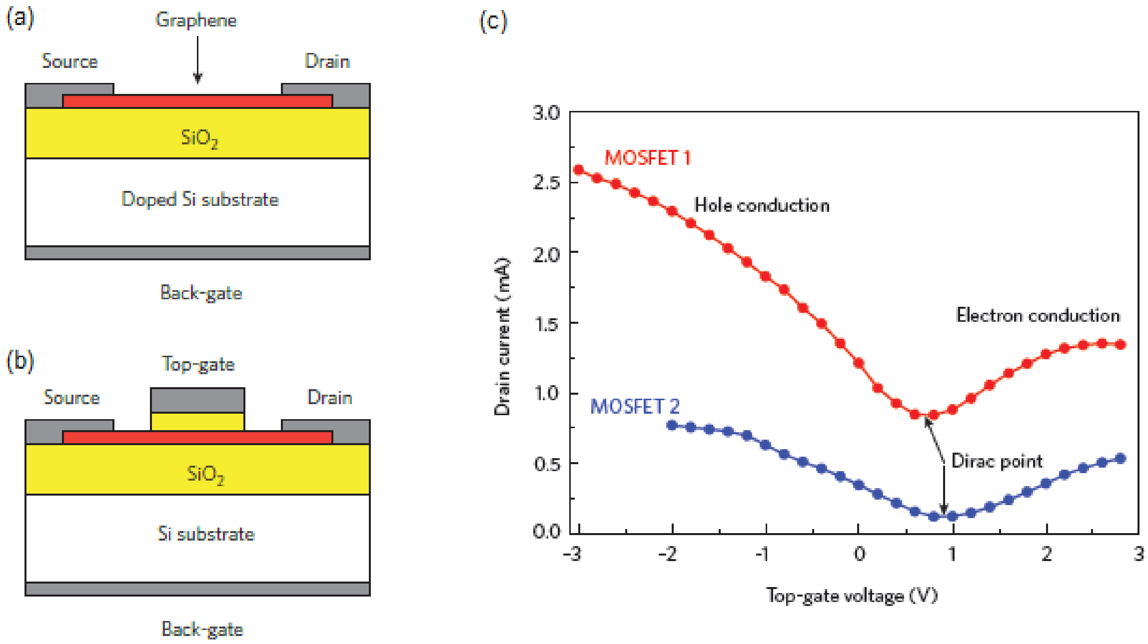

Figure 1.9. *(a) Schematic representation of a back-gated GFET. (b) Schematic representation of a top-gated GFET. (c) Transfer characteristics for two large-area-graphene MOSFETs. At large positive gate voltages charge is transported by electrons, whereas at large negative gate voltages the charge carriers are holes. At intermediate gate voltage the Dirac point or CNP is situated. (Adapted from ref.* [33]*)*

Although the design of a GFET as presented above shows some similarities to conventional MOSFETs, its operation principle is rather different. The introduction of mobile charge carriers in the graphene channel does not rely on the formation of an inversion sheet of minority carriers, but instead the gate voltage is used to modulate the number and type of majority charge carriers. Because of the peculiar band structure of graphene, large-area-graphene transistors exhibit a typical transfer characteristic as shown in Figure 1.9c, clearly reflecting the ambipolar field effect characteristic [33]. This unique transfer characteristic also illustrates that switching of GFETs is restricted and on/off ratios for large-area-graphene FETs are typically in the range of 2-20 [33]. It is also important to note that the exact position of the CNP strongly depends on the doping level of graphene.

A considerable issue in the use of graphene in FETs is its zero band gap nature, which prevents transistors from being switched off and consequently hinders the introduction of graphene as a channel material in logic devices. For proper switching of the transistor, a band gap of about 0.4 eV is required [35]. Fortunately, it has been shown that the band structure of graphene can be modified to a certain extent and that it is possible to open a band gap. The best-known strategy for this purpose is the production of graphene nanoribbons (GNRs), in which the dimensions of the graphene sheet are confined in the lateral direction [39]. The band gap in such a GNR is, to a good approximation, inversely proportional to its lateral width. It was demonstrated that for GNRs with a lateral width below 10 nm, on/off ratios above 10^7 can be achieved [40]. However, the main limitation of this approach is the production of GNRs with well-defined edges and constant, narrow lateral widths. Other methods to introduce a band gap in graphene are biasing bilayer graphene or applying strain to graphene, but these methods also suffer from serious limitations [33]. A more fundamental problem associated with the introduction of a band gap in graphene is the intrinsic decrease in carrier mobility with increasing band gap. In fact, after introduction of a band gap similar to that of Si (1.1 eV), graphene no longer offers an improved carrier mobility compared to conventional Si based FETs [33].

While the presence of a band gap is essential for logic transistors, it is less obligatory for RF transistors. For these applications, high mobility of the charge carriers in the channel combined with a very thin channel material are the main conditions for device performance [41]. Graphene-based RF transistors with a cut-off frequency reaching the THz region have been described for a sub-100 nm channel length [42].

1.3 Adsorption of molecules on graphene

Molecules in the surroundings of graphene can have a drastic impact on its electronic characteristics. On the one hand, the adsorption of molecules on graphene generally results in charge transfer doping, increasing the number of mobile charge carriers in pristine graphene. On the other hand, they form an additional source of charged impurity scatterers, decreasing the mobility of the charge carriers. The relative importance of the two effects is still under debate [43].

1.3.1 Ultrasensitive graphene gas sensors

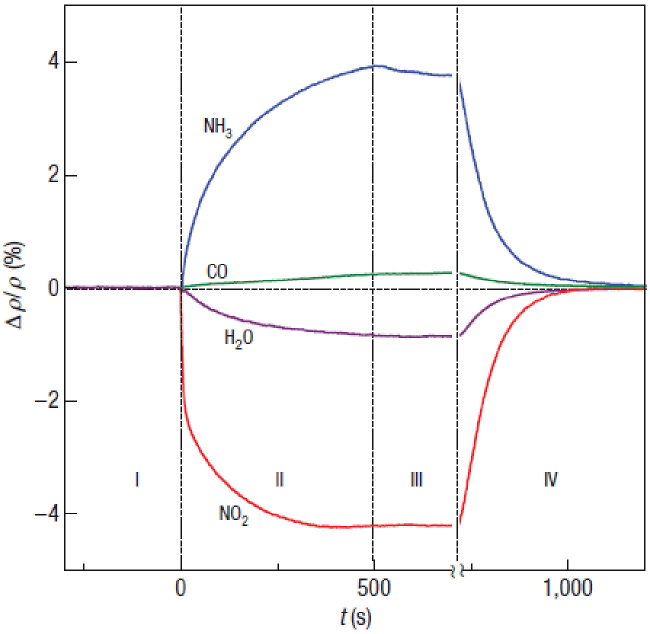

Figure 1.10. *Changes in resistivity of graphene devices exposed to various gases diluted in concentrations of 1 p.p.m. The positive (negative) sign of the change in resistivity is arbitrarily chosen to indicate electron (hole) doping. In region I, the devices are in a vacuum chamber. Next, upon exposure to various gases an initial fast response is observed (region II) that gradually decreases leading to a saturation regime (region III). Annealing in UHV at 150 °C recovers the pristine graphene characteristics (region IV). (Adapted from ref.* [32]*)*

The aforementioned effects enable the production of extremely sensitive graphene-based gas sensors. In 2007, Schedin *et al.* presented, for the first time, a graphene-based sensor capable of detecting single gas molecules [32]. The species under investigation were NO_2, NH_3, CO and H_2O. Figure 1.10 shows the changes in resistivity as a function of time when the devices were exposed to various gases in concentrations of 1 part per million (p.p.m.). Upon exposure, an initial rapid response is observed for all investigated species, which gradually decreases with time because a saturation regime is entered (region II). Evacuating the gaseous species from the chamber did not lead to major changes in resistivity, indicating that these species are strongly adsorbed onto the surface (region III). Interestingly, upon annealing at 150 °C in ultrahigh vacuum (UHV), the pristine graphene characteristics could be recovered (region IV) and repetitive exposure/annealing steps did not lead to a decrease in the device performance.

The ultrahigh sensitivity of this sensor can be understood by a combination of (1) graphene is a surface-only material, having its whole ‘volume’ exposed to the environment, (2) graphene is highly conductive and has therefore low Johnson noise[3] and (3) pristine graphene is free of mobile charge carriers and, consequently, a small increase in charge carriers causes major changes in conductivity [43].

1.3.2 Physisorption *vs.* chemisorption

In general, two classes of adsorption processes on graphene can be discerned: physisorption and chemisorption [43]. In the case of physisorption, the newly formed bond is relatively weak (10-100 meV) and long (> 2.5 Å). Because of this weak bonding, physisorbed molecules have a low migration barrier (MB), which enables them to almost freely stroll around over the graphene surface (MB < 0.1 eV). Chemisorption, on the other hand, is characterized by much stronger (> 0.5 eV) and shorter (1 – 2.5 Å) bonds. Consequently, the MB for chemisorbed molecules is significantly higher (MB > 0.5 eV) and chemisorbed molecules are strongly fixed to their adsorption site [43].

There is a rather clear distinction between both mechanisms as chemisorption on graphene requires rehybridization of one carbon atom from sp^2 to sp^3. This results in a carbon atom bumping out of the basal graphene plane, disrupting the conjugated sp^2 network. Chemisorption on graphene, therefore, costs a lot of energy and only very few reagents are able to overcome this energy cost. In the following we will focus on physisorption of molecules on graphene.

1.3.3 Various ways of molecular doping of graphene

Doping is a well-known phenomenon in semiconductor industries, where, for instance, silicon atoms in the crystal structure of bulk silicon are replaced by atoms having one fewer or one extra valence electron, resulting in an increased charge carrier concentration. However, such substitutional doping of graphene with *e.g.* boron or nitrogen atoms has proven to induce a strong perturbation of the local atomic and electronic structure [44]. A milder method of doping graphene can be achieved by bringing graphene in contact with molecules at its surface. This results in an exchange

---

[3] Johnson noise refers to the electronic noise generated by thermal agitation of the charge carriers in a conductor, regardless of the applied voltage.

of electrons between graphene and the adsorbates. Therefore, this doping mechanism is referred to as surface charge transfer doping.

1.3.3.1 Doping across the solid-solid interface

Doping across the solid-solid interface is the most general case of surface charge transfer doping of graphene. Here, two different mechanisms can be distinguished: (1) direct charge transfer as a result of the relative position of the HOMO/LUMO of the adsorbate with respect to the DOS of graphene and (2) charge transfer resulting from orbital mixing (hybridization) between the HOMO/LUMO of the adsorbate and orbitals of graphene [45].

The first mechanism can be schematically visualized as in Figure 1.11. Here, n-type doping of graphene occurs when the HOMO of the adsorbate is located above the graphene Fermi level. In this way graphene provides low energy empty states, which are accessible for electrons present in the HOMO of the adsorbate. As a result, electrons will flow from the adsorbate to graphene leading to n-type doping of graphene. In an analogous manner, p-type doping results when the LUMO of the adsorbate is below the graphene Fermi level.

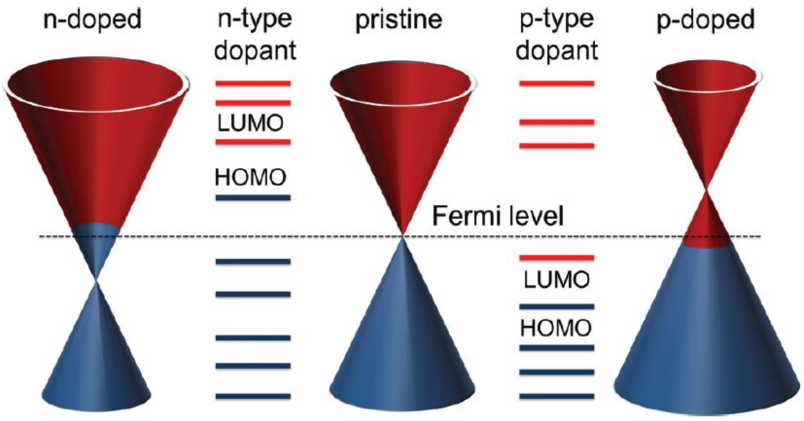

Figure 1.11. *Schematic representation of direct charge transfer in graphene-adsorbate (dopant) systems, resulting from the relative position of the HOMO/LUMO of the adsorbate with respect to the DOS of graphene. The Fermi level refers to the graphene Fermi level only and not to that of the dopant. (Adapted from ref.* [46]*)*

Based upon this model, a distinction is often made between open-shell adsorbates and closed-shell adsorbates [43], [47]. The former have, by definition, partially occupied valence orbitals, which strongly increases their doping potential.

Thus, open-shell adsorbates are in general expected to be stronger dopants than their closed-shell counterparts.

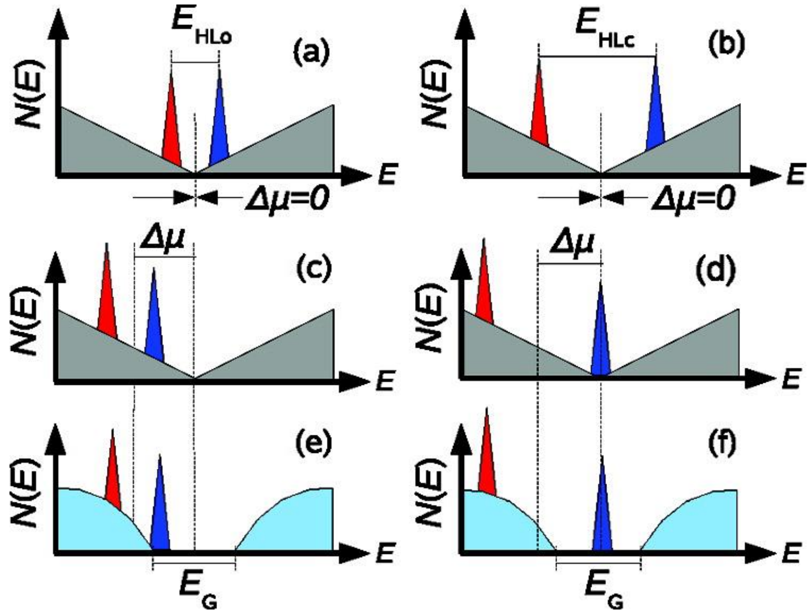

Figure 1.12. *Schematic representation illustrating the different doping potential of open-shell adsorbates with a small HOMO/LUMO splitting (E_{HLo}, left) compared to closed-shell adsorbates with a large HOMO/LUMO splitting (E_{HLc}, right). (a), (b) DOS of an open-shell and closed-shell structure, respectively, superimposed on the DOS of graphene (grey), not taking into account an offset in chemical potential (Δμ). (c) For open-shell structures, only a small offset in chemical potential creates active donor or acceptor levels leading to direct charge transfer ($|\Delta\mu| > 0.5E_{HLo}$). (d) A much larger offset in chemical potential is required to create active donor or acceptor levels in the case of closed-shell structures ($|\Delta\mu| > 0.5E_{HLc}$). (e), (f) For classical semiconductors the minimal offset in chemical potential required to create active donor or acceptor levels is always higher than for graphene because of the presence of a band gap ($|\Delta\mu| > 0.5(E_g + E_{HL})$). (Adapted from ref.* [47]*)*

In open-shell adsorbates, the occupied and unoccupied electron states are separated by a Hund exchange energy of the order of 1 eV [43]. Looking at Figure 1.12, one can now easily see that only a small offset in chemical potential between the adsorbate and graphene is enough to create a situation where direct charge transfer is possible. Closed-shell adsorbates, on the other hand, are characterized by a HOMO/LUMO splitting of the order of 5-10 eV [43]. Therefore, a much larger offset in chemical potential is required to create active donor or acceptor levels. It is furthermore interesting to expand this reasoning to classical semiconductors, where the presence of a band gap inherently requires a larger offset in chemical potential compared to graphene. Therefore, graphene-based gas sensors are more sensitive than sensors based on classical semiconductors.

From the foregoing discussion, it is clear that the relative position of the HOMO/LUMO of the adsorbate with respect to the DOS of graphene is critical to induce strong, direct charge transfer doping. However, even when the offset in chemical potential is too small to create active donor or acceptor levels, *e.g.* for closed-shell adsorbates, charge transfer is not excluded [43]. In that case, orbital mixing between the HOMO and LUMO of the adsorbate with graphene orbitals can still lead to a small amount of charge transfer. The degree of this orbital mixing scales with the geometrical overlap between the involved orbitals and with the inverse of their energy difference [45].

1.3.3.2 Electrochemical doping

A different doping mechanism arises when a water layer is present at the graphene surface. This electrochemical type of doping was first introduced by Chakrapani *et al.* to explain the unexpected conductance that was observed for hydrogenated diamond samples in air [48]. Their assumption was that an aqueous redox couple, created by H_2O and O_2 from air, set the appropriate conditions for electrochemical doping of the hydrogenated diamond. The involved half reactions are:

$$O_{2(g)} + 4H^+{}_{(aq)} + 4e^- \rightleftharpoons 2H_2O_{(l)}, \qquad \text{Eq. (6)}$$

$$O_{2(g)} + 2H_2O_{(l)} + 4e^- \rightleftharpoons 4OH^-{}_{(aq)} \qquad \text{Eq. (7)}$$

Which one of the two proposed half reactions is dominant depends on the specific acidity of the medium, where the presence of CO_2 can play an important role. The electrochemical potential of the two half reactions described above equals -5.66 eV and -4.83 eV, respectively. Figure 1.13 plots the electrochemical potential range of the aqueous redox couple together with the electron energies of hydrogenated diamond (work function equals -5.2 eV) and graphene (work function equals -4.5 eV). From this figure it is clear that it is energetically favorable for electrons in hydrogenated diamond or graphene to be transferred to the aqueous redox couple. Therefore, under ambient conditions graphene is expected to be p-doped [49].

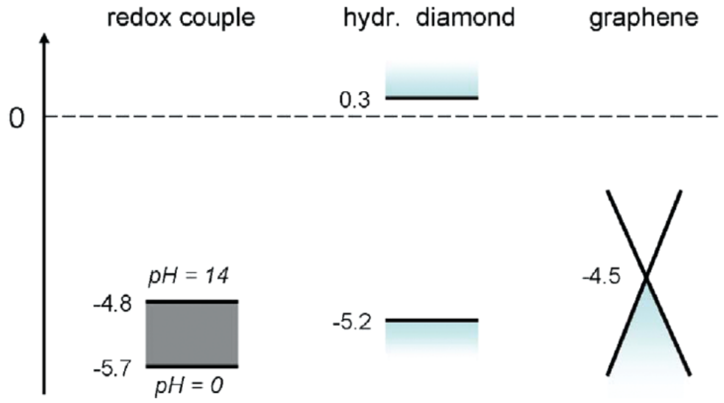

Figure 1.13. *Electrochemical potential of the H_2O/O_2 redox couple (left) displayed next to the electronic band structure of hydrogenated diamond (center) and graphene (right). Depending on the specific acidity of the aqueous phase, the electrochemical potential of the redox couple can span a range of energies. The energies are expressed in eV with respect to the vacuum level. (Adapted from ref.* [43]*)*

Note that this mechanism requires the formation of a water layer near the hydrophobic graphene surface. When graphene is residing on hydrophilic substrates such as *e.g.* SiO_2, it is very likely that this water layer forms at the graphene-substrate interface. Alternatively, but less likely, such a water layer might form on top of the graphene surface. In this context, recent work has revealed that graphene might not be as hydrophobic as was first believed [50]. Moreover, based on the theory of partial wetting transparency, the underlying substrate might influence the hydrophobicity of the basal graphene plane [50].

1.3.4 Limited stability of GFETs

Whenever graphene is exposed to ambient conditions, it is expected that atmospheric species such as O_2 and H_2O cause unintentional doping. This phenomenon was already acknowledged by Novoselov *et al.* in their pioneering graphene paper in 2004 [6]. They observed that without electric field doping, graphene was a hole-metal, which they attributed to unintentional doping by adsorbed water. This assumption was supported by the fact that annealing the devices in vacuum shifted the peak in resistivity to zero gate voltages. Detailed investigations have led to the contemporary accepted assumption that it is not water as such that is responsible for the inherent p-doping of graphene under ambient conditions, but rather the O_2/H_20 redox couple [49], as discussed above.

In this context, Levesque *et al.* performed an important work [49]. They did not only acknowledge, for the first time, the O_2/H_2O redox couple as the primary source of atmospheric doping of graphene, they also demonstrated that the substrate exerts a crucial role in the occurrence of this phenomenon. Both graphene-SiO_2 FETs and graphene-parylene[4] FETs were produced and atmospheric hole doping was only observed for the former as illustrated in Figure 1.14. This was attributed to the hydrophilic nature of SiO_2 substrates, which is critical for the formation of a water layer at the interface. Moreover, the O_2/H_2O redox reaction creates reactive intermediates such as the superoxide anion, peroxide and hydroxyl radical. These species are prone to form traps at the SiO_2 surface, fixing a net negative charge that stabilizes positive charges (holes) in the graphene layer.

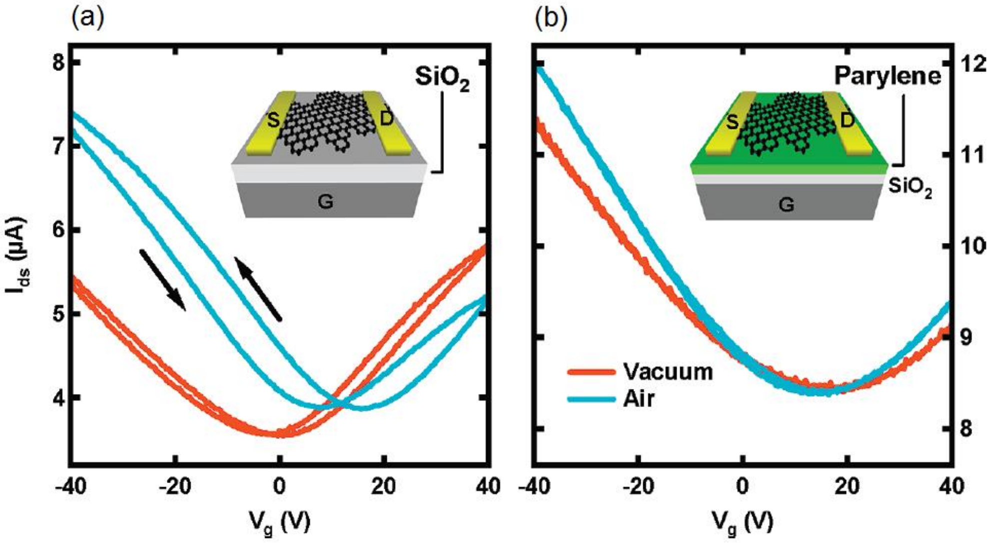

Figure 1.14. *The effect of air exposure on the transfer characteristics of GFETs with different substrates: (a) graphene-SiO_2 FET and (b) graphene-parylene FET. Red: transfer characteristics measured at room temperature following 4 h anneal in vacuum at 400 °C; blue: transfer characteristics measured at room temperature following 30 min of air exposure. The arrows indicate the direction of the back-gate (G) voltage sweep. (Adapted from ref.* [49]*)*

Typically, the unintentional doping of graphene in ambient conditions is accompanied with hysteretic behavior in transfer characteristics[5], as can for instance be observed in Figure 1.14a. The origin of this hysteretic behavior has been attributed to the electrostatic screening of the gate field by charges accumulated at the surface. Here, charge traps at the graphene-substrate interface play a significant role. Again, the presence of a hydrophilic SiO_2 substrate greatly increases the effect and the main

---

[4] Parylene is the trade name for a variety of poly(para-xylylene) polymers.

[5] Hysteretic behavior in transfer characteristics refers to the observation that the conductivity value between source and drain contacts depends on the direction of the back-gate voltage sweep.

source of charge traps is believed to be the aforementioned O_2/H_2O couple [51], [52]. Alternatively, this hysteretic behavior has been attributed to the presence of dipolar adsorbates, typically H_2O, at the graphene surface, which invert their orientation upon sweeping the back-gate voltage [53].

As indicated above, the performance limitations of graphene-based devices in air are strongly dependent on the particular substrate used. Typically, oxidized silicon substrates are used because of their well-established value in semiconductor industries. However, because of their polar nature, these substrates might not be preferred. Another issue that must be considered when optimizing the substrate is charge transfer between the graphene layer and the substrate itself. This effect is well-known for epitaxial graphene (EG) grown on SiC(0001), where a well-ordered epitaxial relationship is responsible for an intrinsic n-doping effect up to carrier concentrations of 1×10^{13} cm^{-2} [54]. Such unintentional n-type doping by the substrate has also been observed for graphene supported by Si/SiO_2 [55]. Experimental results showed an intrinsic electron doping up to carrier concentrations of $\sim 4 \times 10^{12}$ cm^{-2}, which was explained by a low workfunction of SiO_2 relative to graphene. Moreover, these observations were corroborated by theoretical calculations [55], [56]. However, there is no consensus on the type of doping exerted by SiO_2 as most experimental observations indicate p-type doping. Possibly, this p-type doping can be attributed to dangling oxygen bonds in the oxide or to substrate impurities [57], but most probably, the answer to this paradox lies in the subtle interplay between the substrate, the graphene sheet and the atmosphere. Finally, for graphene transferred to h-BN no doping effect by substrate has been observed, approving that higher quality graphene can be obtained on h-BN substrates [17].

When considering the effect of the substrate on the graphene sheet, it is also useful to evaluate substrate roughness. Despite the intrinsic corrugations needed for the thermodynamic stability of graphene [11], it is generally accepted that graphene suspended on *e.g.* SiO_2 partially conforms to the surface corrugation of the underlying substrate, leading to a distortion of the hexagonal lattice symmetry and inducing strain [58]. The extent to which this effect occurs is dependent on the specific interaction strength between graphene and the underlying substrate and can be enhanced by thermal annealing [59].

Finally, it must be noted that another source of graphene contamination stems from the different processing steps needed for the production of functional devices. For instance, transfer of chemical vapor deposited (CVD) graphene grown on transition metal substrates to dielectric substrates results in polymer residues, typically poly(methylmethacrylate) (PMMA), which have shown to exhibit a p-type doping effect on graphene [60]. In addition, graphene devices are typically fabricated using electron beam lithography (EBL), leaving behind photoresist residues [58], [61]. Many different cleaning procedures have been proposed such as *e.g.* wet-chemical treatment [62], thermal annealing [58], [61], electrical current annealing [63], and plasma cleaning [64]. Despite these different strategies, it remains to date very challenging to produce clean devices.

To summarize, graphene has proven to be extremely sensitive to its environment, making it an ideal candidate for ultrasensitive sensors, but also posing severe challenges to (re)produce long-lived, stable GFETs. Charge transfer doping by atmospheric species, underlying substrate, or process related chemicals has been identified as the main cause of device instability, resulting in a shift of the Fermi level away from the Dirac point such that the ambipolar properties of graphene can no longer be exploited. In addition, this unintentional doping is typically accompanied by hysteretic behavior in the transfer characteristics and a reduction in charge carrier mobility.

1.4 Towards stable, tunable devices

In order to implement graphene in everyday devices, it will be necessary to address and solve the issues related to unstable device characteristics that were discussed above. This will require the design of a proper substrate combined with a suitable surface passivation method for graphene. Also, depending on the particular application in mind, it will be useful to have control over the electronic properties of graphene. Here, chemical functionalization with the intention to induce charge transfer doping of graphene will be crucial.

1.4.1 Design of a proper substrate

It needs no further explanation that the substrate plays a key role in the device stability. In general Si/SiO$_2$ substrates are used for the production of GFETs, but it might be more appropriate to employ hydrophobic substrates. As discussed earlier, Levesque *et al.* showed improved device stability in air when using a hydrophobic parylene substrate [49]. In the same context, Mattevi *et al.* compared the long-term stability of graphene-SiO$_2$ FETs and graphene-Hyflon[6] FETs in air [65]. Figure 1.15 displays the evolution of the Dirac point potential as a function of time as determined by electrical measurements. For graphene-SiO$_2$ FETs a rapid shift of the Dirac point is observed immediately after exposure to air. The graphene-Hyflon FETs, on the other hand, show an improved stability in air and a lower extrinsic p-doping. Furthermore, the Hyflon-based devices also show negligible operating hysteresis, a larger carrier mobility and better on/off switching characteristics.

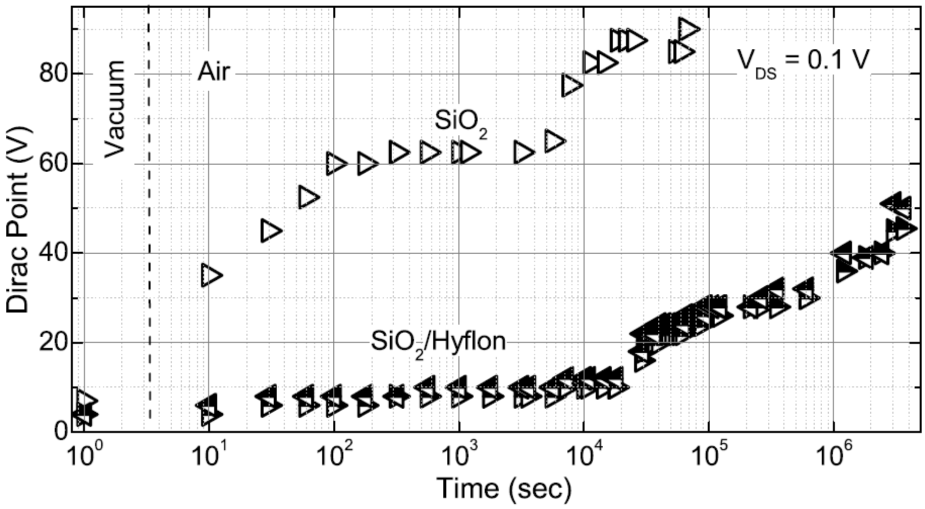

Figure 1.15. *Evolution of the Dirac point potential as a function of time for graphene-SiO$_2$ and graphene-Hyflon FETs exposed to air. Upon leaving the vacuum chamber, a rapid shift of the Dirac point is observed for the graphene-SiO$_2$ FETs, while graphene-Hyflon FETs show a prolonged stability. (Adapted from ref.* [65]*)*

Despite the improved performance of graphene-Hyflon FETs over classical graphene-SiO$_2$ FETs, they still require a relatively large operating voltage. Therefore, the authors explored the use of ultrathin (2-3 nm) organic SAMs as gate dielectric. In

---

[6] Hyflon AD is an amorphous perfluoropolymer, consisting of a copolymer of tetrafluoroethylene and a dioxole.

particular, two different SAM molecules have been investigated: octadecylphosphonic acid (ODPA) and phosphonohexadecanoic acid (PHDA). The structure of both molecules is shown in Figure 1.16. For both molecules, the GFETs displayed hysteresis free operation, lower extrinsic p-doping than graphene-Hyflon FETs, larger on/off ratios and, most importantly, low operating voltages (typically < $|1.5|$ V). Comparing both SAMs led to the conclusion that ODPA-based devices show higher charge carrier mobilities than PHDA-based FETs. This last observation again demonstrates that hydrophobic substrates lead to improved device characteristics.

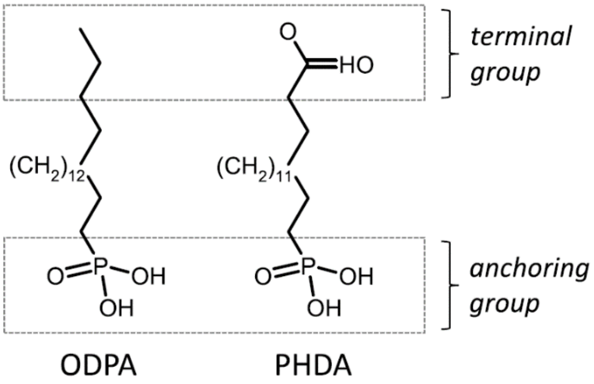

Figure 1.16. *Molecular structure of ODPA and PHDA. Both molecules contain a phosphonic acid group for anchoring to the Al/AlO$_x$ electrode, a linear alkane spacer group and a specific terminal group which determines the surface properties of the particular SAM. (Adapted from ref.* [65]*)*

Similar studies have focussed on using a self-assembled layer of hexamethyldisilazane (HMDS) [53] or phenylsilane [66] to modify the existing Si/SiO$_2$ substrates. These studies demonstrated improved device performance compared to bare Si/SiO$_2$ substrates, analogous to what has been discussed above.

1.4.2 Surface passivation of graphene

To obtain long-term device stability, it will not be enough to only optimize the substrate, but also a proper surface passivation method will be needed. Several studies have been directed towards this purpose.

A first possible approach is to cover the graphene sheet with a polymer layer. This was achieved by Shin *et al.* who demonstrated improved device stability in air when using a PMMA protection layer [67]. The evolution of the Dirac point potential as a function of time in air is depicted in Figure 1.17. The authors of this work claim that the PMMA layer on top of the graphene does not cause charge transfer doping of graphene. However, this is in contradiction with other studies [60]. Therefore, it might be better to explore other types of polymers.

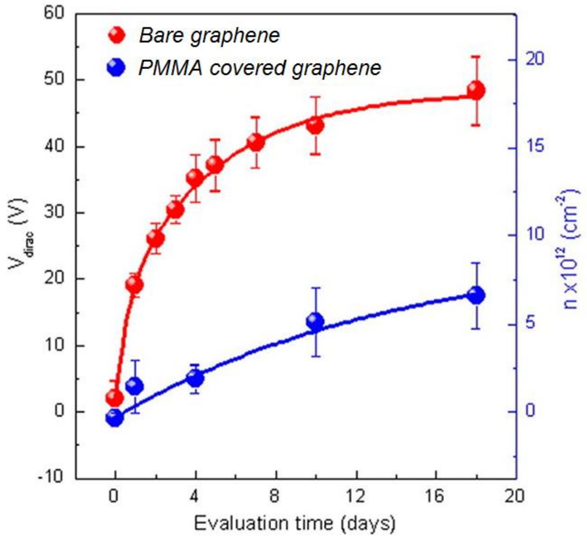

Figure 1.17. *Evolution of the Dirac point potential (left) and the net charge density (right) as a function of time in air for bare graphene devices and graphene devices covered with a PMMA protection layer. The devices covered with a PMMA protection layer clearly show an improved long-term stability compared to the bare graphene devices. (Adapted from ref.* [67]*)*

Kang *et al.* reported the deposition of an aluminium oxide (Al_2O_3) layer as a surface passivation method for graphene, using low temperature atomic layer deposition (ALD) [68]. This approach led to improved stability of the devices in air, combined with reduced hysteresis and larger electron mobilities compared to uncovered GFETs. However, hysteresis free operation was not obtained. According to Sagade *et al.* [69], this residual hysteresis must be assigned to an imperfect encapsulation of the graphene channel due to a lack of nucleation sites on the graphene basal plane, resulting in inhomogeneous growth of the Al_2O_3 layer. In order to overcome this issue, they deposited an extra Al seed layer on top of the graphene sheet prior to ALD growth of Al_2O_3. As evidenced by Figure 1.18, this led to a significant improvement of the long-term device characteristics. Moreover, the robustness of this passivation layer against chemicals and heat treatments was demonstrated.

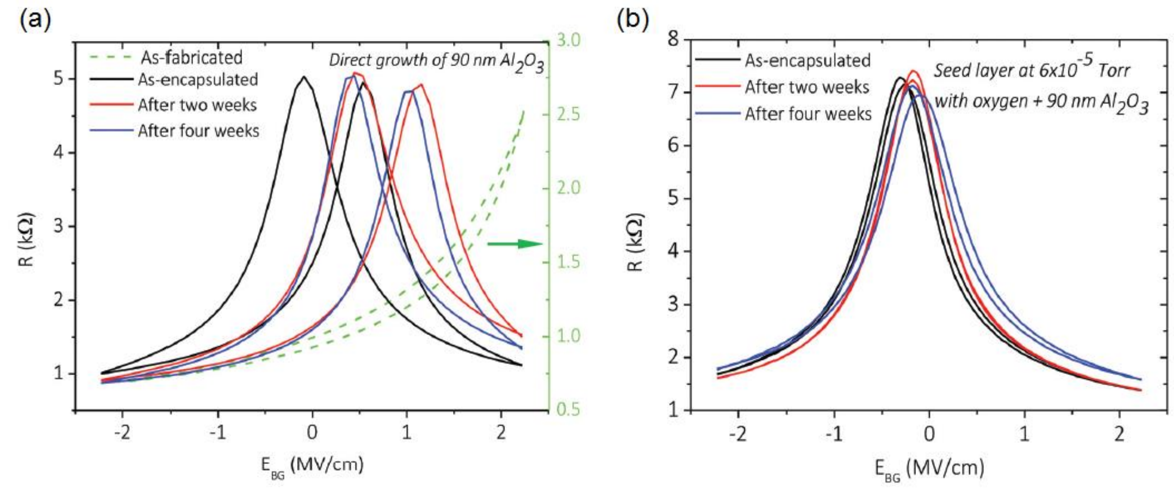

Figure 1.18. *Resistance (R) as a function of the applied electric field (E_{BG}) for (a) GFETs passivated by direct ALD growth of Al_2O_3 and for (b) GFETs passivated by an Al seed layer followed by ALD growth of Al_2O_3. Long-term device stability is obtained only when an extra Al seed layer is deposited prior to the ALD growth of Al_2O_3. (Adapted from ref.* [69]*)*

Lee *et al.* reported the passivation of graphene with a 30 nm thick plasma-enhanced chemical vapor deposited Si_3N_4 layer [70]. To prove the robustness of this passivation method, the devices were immersed in water, green tea, warm coffee and thick milk, mimicking unexpected real life situations. It was shown that the devices maintain their electrical functionality after exposure to these harsh conditions. However, the charge carrier mobility dropped as much as 40 % after exposure to warm coffee.

Another approach was suggested by Wang *et al.* [71]. Using Raman spectroscopy, they showed that high quality and environmentally stable graphene could be obtained for graphene in a h-BN/graphene/h-BN sandwich structure. Though, the formation of a sandwich structure of multiple flakes does not allow for a large-scale production process.

More closely related to the work performed in this thesis, is the passivation of graphene with organic molecules. Jee *et al.* studied the deposition of a 15 nm thick pentacene layer on the graphene surface [72]. They showed that there is no strong interaction between pentacene and graphene, such that the pristine electronic properties of graphene are preserved. Moreover, it was demonstrated that such a pentacene layer on graphene exposed to air can be easily removed by a vacuum annealing step, leaving the original unmodified graphene sheet. In another study, Long *et al.* investigated the functionalization of graphene with a self-assembled 1-aminodecane layer as a potential route towards surface passivation [73]. They showed that the functionalization of GFETs with such a 1-aminodecane layer leads to improved stability of the devices in air compared to bare devices. In addition, the functionalized devices showed a higher mobility, as evidenced in Figure 1.19 by a sharper resistance peak around the Dirac point. The main problem associated with the use of 1-aminodecane as a surface passivation layer is the significant n-type doping induced by the amino-groups, altering the electronic structure of graphene.

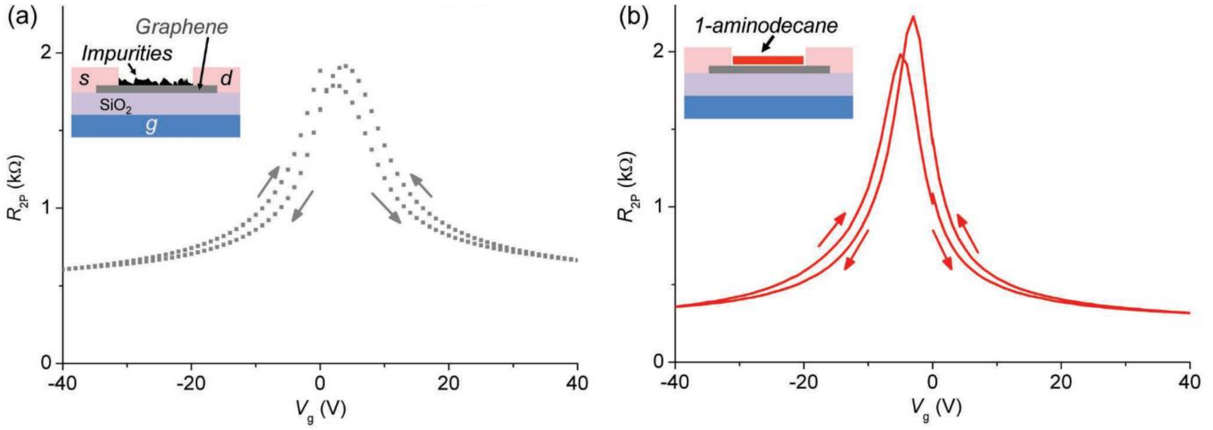

Figure 1.19. *Resistance (R_{2P}) as a function of back-gate voltage (V_g) for (a) a bare GFET and (b) the same GFET functionalized with a self-assembled 1-aminodecane layer following thermal annealing to remove adsorbed contaminants. It is clear that after functionalization of the device with 1-aminodecane, the resistance peak shifts to negative gate voltage and becomes sharper, indicating n-type doping and higher carrier mobility, respectively. (Adapted from ref.* [73]*)*

1.4.3 Intentional charge transfer doping of graphene

Up to now, we have focussed on preserving the pristine electronic properties of graphene. However, to exploit the full potential of graphene, it will be useful to have control over the precise doping level of graphene. In view of this, chemical functionalization with the intention to induce charge transfer doping offers a versatile and facile method to achieve this. Different molecules have been investigated in order to shift the Fermi level to the desired position [46]. In general n-type doping of graphene is more challenging than p-type doping because of its relatively low work function (-4.6 eV).

One type of molecules that have been utilized to p-dope graphene are alkylphosphonic acids. Prado *et al.* have investigated the self-assembly and doping effect of octadecylphosphonic acid (OPA) and tetradecylphosphonic acid (TPA) on mono- and multilayer exfoliated graphene on SiO_2 [74]. Atomic force microscopy (AFM) measurements revealed that both molecules self-assemble on top of graphene in rippled domains (Figure 1.20a for OPA). These ripples consist of dimers, in which the alkylphosphonic acids are oriented head-to-head. The doping effect of OPA on graphene was investigated using Raman spectroscopy (Figure 1.20b). Comparison of the Raman spectrum before and after deposition of OPA shows that after OPA deposition the G peak has shifted to larger wavenumber and has a smaller full width at half-maximum (FWHM). Furthermore, the intensity ratio I_{2D}/I_G has dropped significantly (about 60 %). These findings indicate an effective p-type doping of graphene induced by the OPA adlayer. Noteworthy is also that no D peak appears after OPA deposition, indicating that the deposition process does not induce structural disorder in the graphene lattice.

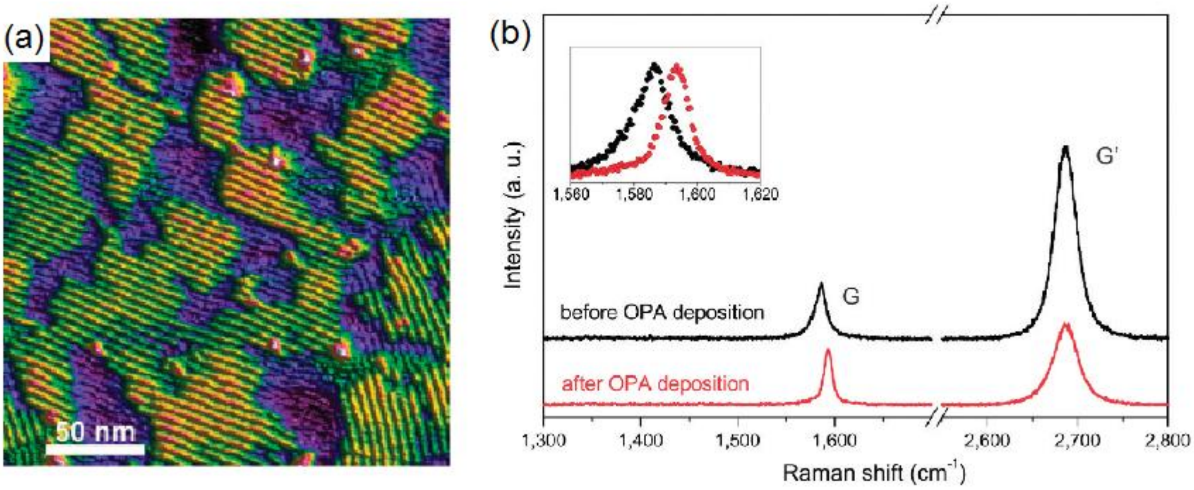

Figure 1.20. *(a) AFM-topography image of OPA (green-yellow) on multilayer exfoliated graphene (purple), showing the formation of rippled domains. (b) Raman spectrum of a monolayer exfoliated graphene flake before and after deposition of OPA. The inset shows a magnification around the position of the G peak. (Adapted from ref.* [74]*)*

Next to p-type doping, also n-type doping of graphene has been reported. An illustrative example of n-type doping of graphene by self-assembly at its surface is provided by Li *et al.* [75]. In this study the self-assembly of oleylamine (OA) on graphene was investigated and doping levels were monitored by electrical measurements in FET configurations. AFM measurements of OA on highly oriented pyrolytic graphite (HOPG) and EG/SiC revealed the formation of well-organized domains with a periodic lamellar pattern (Figure 1.21a,b). Room temperature scanning tunneling microscopy (STM) images of OA on HOPG confirmed the formation of lamellae in which the molecules adopt a head-to-head non-interdigitating configuration (Figure 1.21c,d). Using exfoliated graphene transferred to SiO_2, back-gated FETs were produced and electrically characterized (Figure 1.21e). This indicated n-type doping of the graphene channel by adsorption of OA. A second deposition of OA led to an increased n-type doping effect. Further deposition of OA no longer affected the doping level, indicating that charge transfer is saturated after two deposition steps. Interesting is that afterwards the pristine electronic device characteristics could be recovered by sonicating the device in a hexane solution, proving the reversible nature of physisorption.

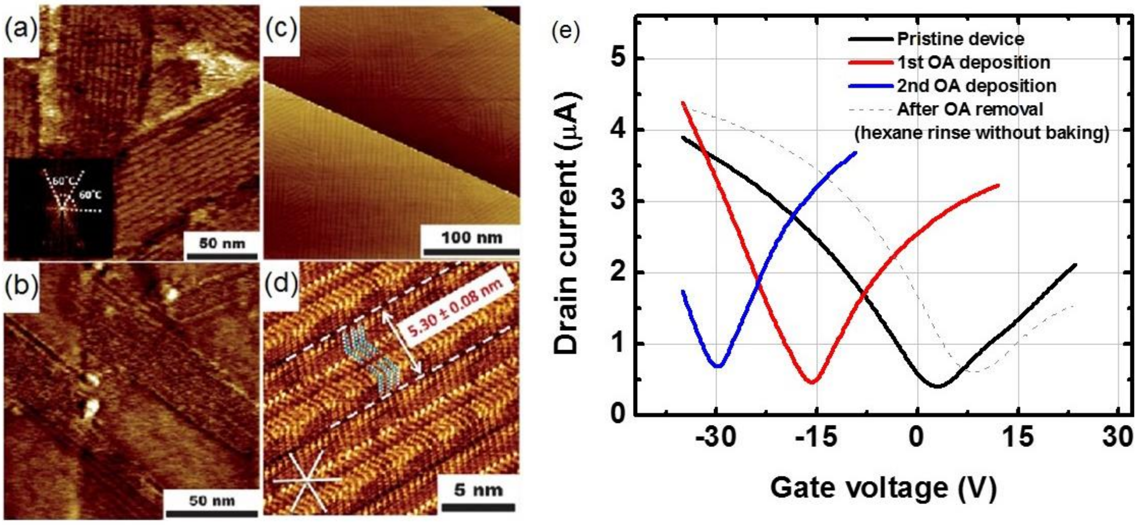

Figure 1.21. (a) AFM phase image of OA on HOPG showing the formation of well-defined domains with a lamellar pattern. (b) AFM phase image of OA on EG/SiC demonstrating the formation of lamellar structured domains similar to those on HOPG. (c) Large scale STM image of self-assembled OA on HOPG, indicating the formation of lamellar structures. (d) High resolution STM image of OA on HOPG showing molecular details of the lamellae. The molecules self-assemble in a head-to-head non-interdigitating configuration and form dimers. (e) Transfer curves of a FET device functionalized with no (black), a single deposition of (red) and a double deposition of (blue) OA. Functionalization with OA leads to n-type doping of graphene, saturating after two deposition steps. Sonication in hexane restores the pristine device characteristics (dashed curve). (Adapted from ref. [75]*)*

1.5 Aim and outline of the thesis

This work investigates the surface passivation of graphene with the use of an organic SAM in order to improve the stability of graphene-based field effect devices in air. In particular, n-pentacontane ($n\text{-}C_{50}H_{102}$ or simply C_{50}) is studied as a potential surface passivation layer. C_{50} is chosen because (1) C_{50} is known to form stable, self-assembled layers on HOPG [76], (2) linear alkanes have been successfully employed as ‘buffer layers’ for diverse purposes [76]–[78], and (3) charge transfer doping of graphene by linear alkane molecules has not been reported, indicating that C_{50} will very likely preserve the pristine electronic properties of graphene.

The first objective is to characterize the formation of a self-assembled C_{50} monolayer on HOPG. Special attention is paid to the formation of a homogeneous C_{50} monolayer, comprising ultra-large C_{50} domains. The formation of such large domains is desired because it is believed that at the boundary of adjacent C_{50} domains the surface passivation potential is lower. Once a high quality C_{50} film has been established, the second objective is to evaluate the self-assembly behavior of octadecylamine (ODA) on a C_{50}-functionalized HOPG surface and to compare this with the self-assembly of ODA on bare HOPG. The information gathered by the experiments on HOPG is believed to be essential for the correct evaluation of the shielding potential of a C_{50} layer on graphene against (atmospheric or, in the case of ODA, deliberately added) dopants.

The second part of experiments involves surface passivation of graphene with a C_{50} layer. To assess the feasibility of this approach, the surface passivation of graphene will be tested in two different ways: (1) C_{50}-functionalized and bare graphene flakes are compared as a function of time in order to see the potential of a C_{50} layer to eliminate atmospheric doping; (2) ODA is deposited on top of both C_{50}-functionalized and bare graphene flakes and the doping of graphene is compared. ODA is chosen because amine-based molecules are known to cause strong n-type doping of graphene [73], [75], and in this way allow to assess the robustness of the C_{50} layer against strong, deliberately added dopants

The outline of this thesis follows the more classical scheme: the second chapter briefly discusses the operation principle of the different characterization techniques and experimental approaches that have been employed, the third chapter discusses the performed experiments and results, and finally, in chapter 4 a conclusion is made and future work is discussed.

Chapter 2: Materials and methods

Several methods and techniques have been used throughout this work. This chapter provides background information on the main techniques that were used and describes in detail how graphene field effect devices were produced starting from bulk graphite.

2.1 Deposition techniques

2.1.1 Drop-casting

Drop-casting is the transfer of a small amount of a solution containing the molecules to be deposited to the desired substrate using a pipette. Once the solution is released on the surface, self-assembly takes place at the liquid-solid interface. Depending on the boiling point of the solvent, the solvent either evaporates faster or slower. In the case of fast evaporation, self-assembly processes might be kinetically trapped.

2.1.2 Dip-coating

Dip-coating is the controlled immersion and withdrawal of a substrate into a solution containing the molecules or particles to be deposited. In fact, dip-coating is a widely used deposition technique for both academic and industrial purposes. Figure 2.1a schematically represents the process.

During the period of immersion, molecules diffuse to the surface where self-assembly can take place. The imposed effect of substrate withdrawal is somewhat more complicated. Figure 2.1b illustrates the different driving forces that act during withdrawal of the substrate. According to Grosso, the relative importance of these driving forces strongly depends on the speed of withdrawal [79]. As a result, three different regimes can be discerned, as illustrated in Figure 2.1c for the deposition of mesoporous silica. At low withdrawal speed, the deposition process is governed by capillary forces and evaporation effects. On the other hand, the process is mainly determined by drag forces at high withdrawal speed. At intermediate speed, both effects counterbalance each other and the thinnest film is formed.

Figure 2.1c also illustrates the predicted effects of ambient temperature and concentration on the film thickness. Increasing the temperature speeds up the evaporation process and consequently leads to thicker films. On the other hand, thinner films are formed in more diluted solutions.

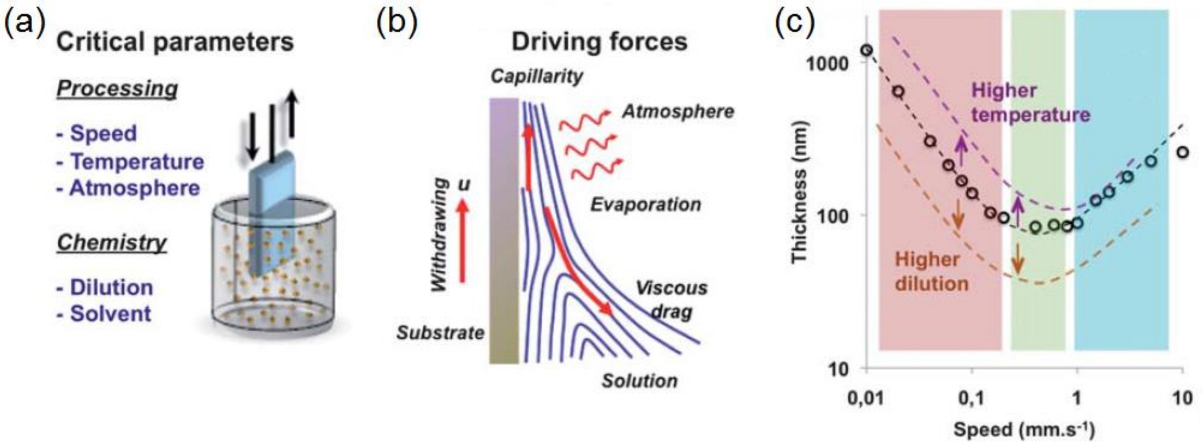

Figure 2.1. (a) Schematic representation of the dip-coating process highlighting the critical parameters that influence the final film characteristics. (b) Illustration of the different driving forces governing the deposition process during withdrawal of the substrate. (c) Plot of thickness vs. speed showing the three different deposition regimes. The open circles correspond to experimental data obtained for the deposition of a mesoporous silica film. At low withdrawal speed capillary forces and evaporation effects govern the deposition process (pink). At high withdrawal speed, the deposition process is mainly determined by a viscous drag (blue). Both effects counterbalance each other at intermediate speed, yielding the thinnest film (green). Also the predicted effect of higher ambient temperature and higher dilution is illustrated. (Adapted from ref. [79]*)*

It must be noted that evaluating self-assembly of molecules deposited by a dip-coating process is actually a *contradictio in terminis* as self-assembly implies the spontaneous formation of molecular superstructures without external guidance. Though, dip-coating induces a flow during immersion/withdrawal that can affect the characteristics of the final structure, thereby ‘directing’ the self-assembly process. However, this being said, the term self-assembly will be used throughout the rest of this thesis, irrespective of the deposition technique.

The dip-coating parameters used for the experiments performed in this work are: uncontrolled immersion, 30 min residence in solution (15 ml) before withdrawal and withdrawal at 0.5 mm/min, unless stated otherwise. All dip-coating processes were conducted at room temperature.

2.2 Scanning probe microscopy

The invention of the STM in the early 1980’s by Rohrer and Binnig at IBM Zurich [80] gave birth to a whole new class of real-space imaging instruments known as scanning probe microscopes (SPM). These microscopes make use of a physical probe to scan the surface under investigation, providing information about the surface topography and/or other surface properties. The strongly localized nature of the probe enables to image the surface with very high lateral resolution ranging up to atomic dimensions. These instruments are therefore very convenient for imaging self-assembled structures at surfaces.

2.2.1 Scanning tunneling microscopy

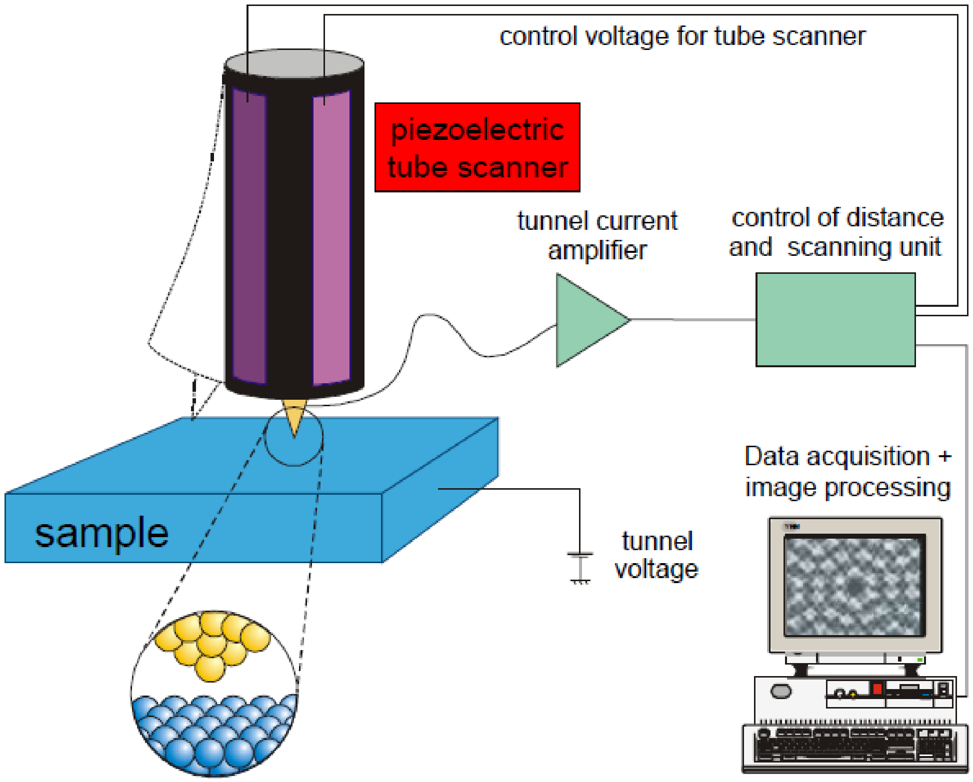

Figure 2.2. Schematic representation of the STM showing its most important features. (Adapted from ref. [81]*)*

Central to the operation of STM is a sharp conductive tip which is brought extremely close to a conductive substrate. The essential parts of the STM are shown in Figure 2.2. The combination of a coarse positioner and a z-piezo allow to bring the scanning tip and the sample to within a few ångström of each. In such a close proximity the electron wavefunctions of the sample and the tip overlap and upon applying a voltage bias, this results in an electrical current. As there is no real physical contact between the sample and the tip, this is not a classical current, but a tunneling current. The achievement of atomic resolution in STM images derives from the fact that the tunneling current is exponentially decaying with increasing tip-sample distance according to:

$$I_t \sim U_t \cdot e^{-Cd_{ts}}, \qquad \text{Eq. (8)}$$

where I_t is the tunneling current, U_t is the applied voltage bias, C is a constant (which includes the workfunctions for the tip and sample) and d_{ts} is the tip-sample distance [82].

A current amplifier is used to amplify the tunneling current and convert it to a voltage. This voltage in turn is compared to a reference value and the difference is again amplified to drive the z-piezo. In this way a feedback is established and the tunneling current is maintained at a fixed value. Driving the x- and y-piezo allows the tip to raster scan[7] over the sample surface and a contour plot of the equal tunneling current surface is obtained and stored. The interpretation of the equal tunneling current surface is somewhat more complicated. On surfaces with uniform electronic properties the image obtained corresponds to a true topographic image. On surfaces that are electronically inhomogeneous, however, the changes in tunneling current upon moving the tip laterally depend not only on the surface topography, but also on the local electronic structure [83]. Regions of greater electron DOS result in an increase of the tunneling current, independent of the surface topography. This is a typical feature of STM images and must always be kept in mind when analyzing these images.

All STM experiments in this work were performed at room temperature using a PicoLE (Agilent) or PicoSPM (Molecular Imaging) STM operating in constant current mode. Tips were mechanically cut from a Pt/Ir (80%/20%) wire. Analysis of images was performed with SPIP 5.1.4 (Image Metrology A/S) or WSxM 5.0 Develop 7.0 (Nanotec Electronica S.L.) software. All images were plane fitted and flattened, unless stated otherwise.

---

[7] Raster scanning is a technique in which an image is formed line by line. This line-by-line scanning systematically covers the total area to be scanned and can be used to reconstruct a raster image of the area. In the specific case of SPM the y-piezo is driven from left to right and back again, while the x-piezo progresses much more slowly.

2.2.2 Atomic force microscopy

With the invention of STM a new era in surface science was introduced, allowing to image surfaces and interfaces with atomic resolution. However, the applicability of STM is limited to conductive substrates only. In order to image all sorts of substrates Binnig invented the AFM, only a few years after the inception of the STM [84]. The main components of a typical AFM instrument are schematically depicted in Figure 2.3a, and contain a microfabricated cantilever with a sharp tip at its end, a piezo scanner that supports the sample, an optical laser and position-sensitive quadrant photodetector and an electronic circuit to establish a feedback loop.

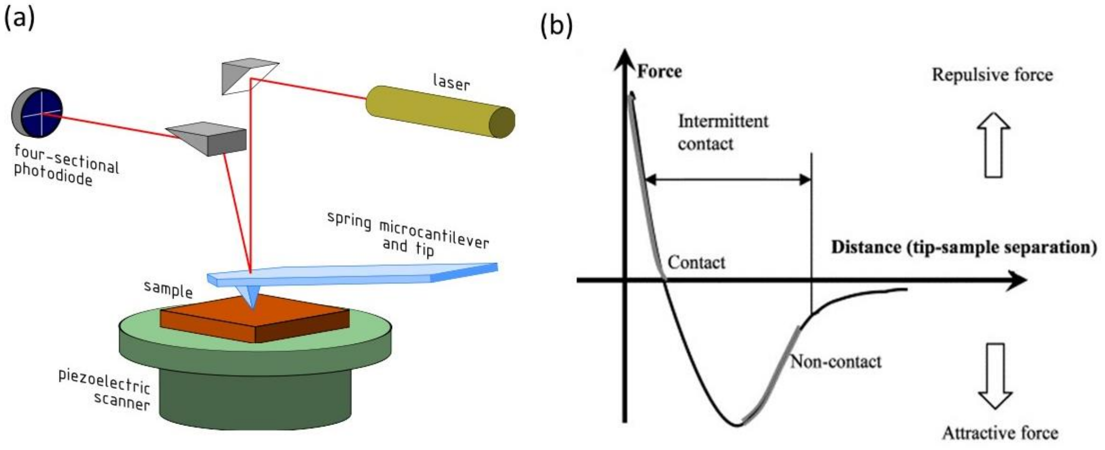

Figure 2.3. *(a) Schematic representation of the AFM showing its most important features. (Adapted from ref.* [85]*) (b) Force-displacement curve depicting the interaction forces that act between tip and sample when they are brought in close proximity of each other. At relatively large tip-sample separations the interaction force is attractive. At smaller separations, however, a repulsive force starts to play because of repelling electron clouds. Eventually this repulsive force completely cancels the attractive forces resulting in complete repulsion upon contact. (Adapted from ref.* [86]*)*

When the tip is brought in close proximity of the sample surface, forces start to act on the cantilever which results in a deflection of the cantilever from its initial position. It is this deflection that is monitored by the photodetector and that provides information on the surface properties. The interaction forces that act between the tip and the surface can be identified in a force-displacement curve as shown in Figure 2.3b. At relatively large tip-sample distances, weak attractive forces are generated that increase in magnitude upon lowering the interatomic distance. At a certain tip-sample distance, where the tip is in very close proximity to the sample surface, the electron clouds start to repel each other. This repulsive force increases rapidly upon further reducing the tip-sample distance and when the interatomic distance is only a few ångström the repulsive force completely cancels the attractive forces.

Typically, the AFM systems can be operated in three different modes depending on which regime of the force-displacement curve is exploited: contact mode, non-contact mode and tapping mode. In contact mode the tip is in mechanical contact with the sample and the interaction force is repulsive. Upon scanning the surface the cantilever experiences deflections because of varying surface properties and a feedback loop is employed to keep the interaction force constant [86]. This feedback signal is usually used to map the surface topography. Alternatively, the AFM can be employed in non-contact mode. In this operation mode the cantilever is vibrated at or near its resonance frequency, with an amplitude of less than 1 nm [87]. The dynamics of such a vibrating tip link to the tip-surface interactions by the amplitude, the resonance frequency and the phase shift of the oscillation and any of these features could be used to drive the feedback loop and therefore to map the surface topography [88]. Very analogue to non-contact mode is tapping mode. In tapping mode the cantilever is also vibrated at or near its resonance frequency but with a much larger amplitude (> 100 nm) [87]. In this way the tip alternates between contact and non-contact and both repulsive and attractive forces influence the imposed oscillation. The advantage of non-contact and tapping mode compared to contact mode is that reduced mechanical contact with the sample results in less damage caused to the sample by the presence of the tip during the scanning process. Therefore, these operation modes are preferred to image 'soft' samples such as physisorbed SAMs.

All AFM experiments in this work were performed at room temperature using a Cypher ES (Asylum Research, Oxford Instruments) or SmartSPM-1000 (AIST-NT) AFM in tapping mode. Analysis of images was performed with WSxM 5.0 Develop 7.0 (Nanotec Electronica S.L.) software. All images were plane fitted and flattened, unless stated otherwise.

2.3 Production of graphene flakes

In this work, mechanically exfoliated graphene flakes on Si/SiO_2 (90 nm of oxide) have been used. The production of these flakes consisted of 2 different parts. First the Si/SiO_2 substrates were subjected to the following cleaning protocol:

- DI water cleaning
- Isopropylalcohol (IPA) dipping
- Hot acetone (50 °C) cleaning for 1 h
- 3 min sonication in acetone
- IPA dipping
- N_2 blow drying
- Thermal annealing in forming gas (95% N_2/5% H_2) (20 min, 300 °C)

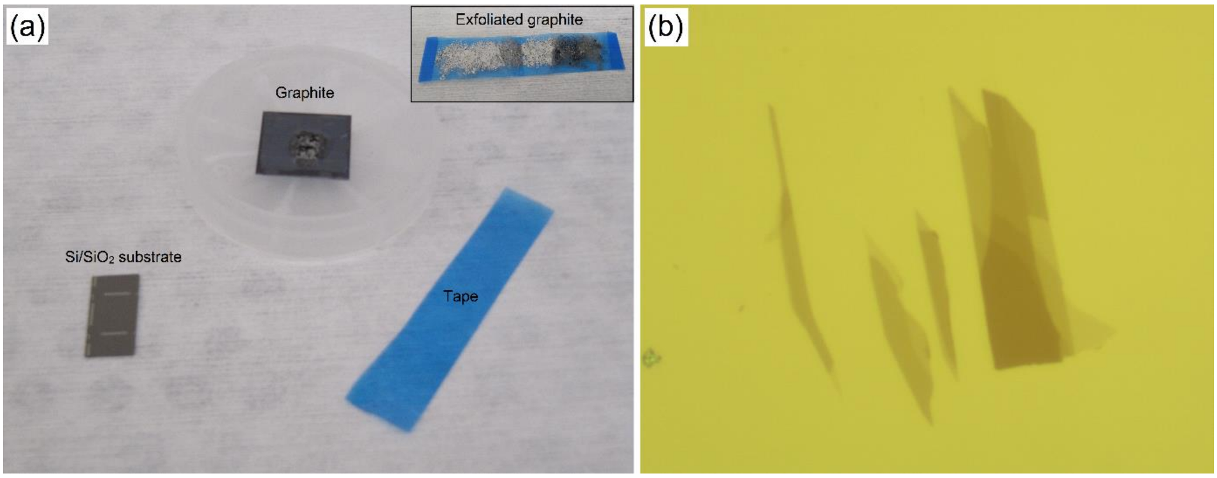

Figure 2.4. *Illustration of the production process of exfoliated graphene flakes. (a) Using adhesive tape, graphite is exfoliated from a bulk graphite sample. Once the graphite has been thinned and spread out over the entire tape surface, the tape is pressed firmly to a Si/SiO$_2$ substrate. (b) Using an optical microscope, the position of the transferred flakes can be determined and the optical contrast difference allows to identify the number of graphene layers.*

Next, graphene flakes were mechanically exfoliated from graphite with adhesive tape and subsequently transferred to the pre-cleaned Si/SiO$_2$ substrates (Figure 2.4). This leaves one to a few layers of graphene on the surface. In order to remove tape residues, the flakes were subsequently cleaned in toluene (room temperature, ± 70 h) and annealed in forming gas (9 h at 300 °C and 7×10^{-5} bar, ramp up = 1 °C/min, cool down = 4 °C/min). As shown in Figure 2.5, the flakes are relatively clean after this cleaning procedure. For reference, AFM images of HOPG are added in Figure 2.5 and a comparison of the RMS roughness values immediately illustrates that graphene flakes are much more rough than HOPG. This increased roughness is attributed to the fact that graphene flakes on SiO$_2$ partially conform to the underlying substrate. As a result, it is expected that (visualization of) self-assembly will be more challenging on graphene flakes than on HOPG. Finally, it should be noted that this cleaning procedure results in strongly p-doped flakes, as discussed in Appendix 1.

The finding and identification of the graphene flakes afterwards may be the most challenging part of the method. Fortunately, it is shown that SLG and FLG on a Si/SiO_2 substrate with the appropriate oxide thickness (90 nm or 300 nm) can be observed and identified using optical microscopy [89]. Depending on the number of layers a subtle color difference is perceived in the optical images, as illustrated in Figure 2.4b. To determine the exact number of layers, Raman spectroscopy was employed [90].

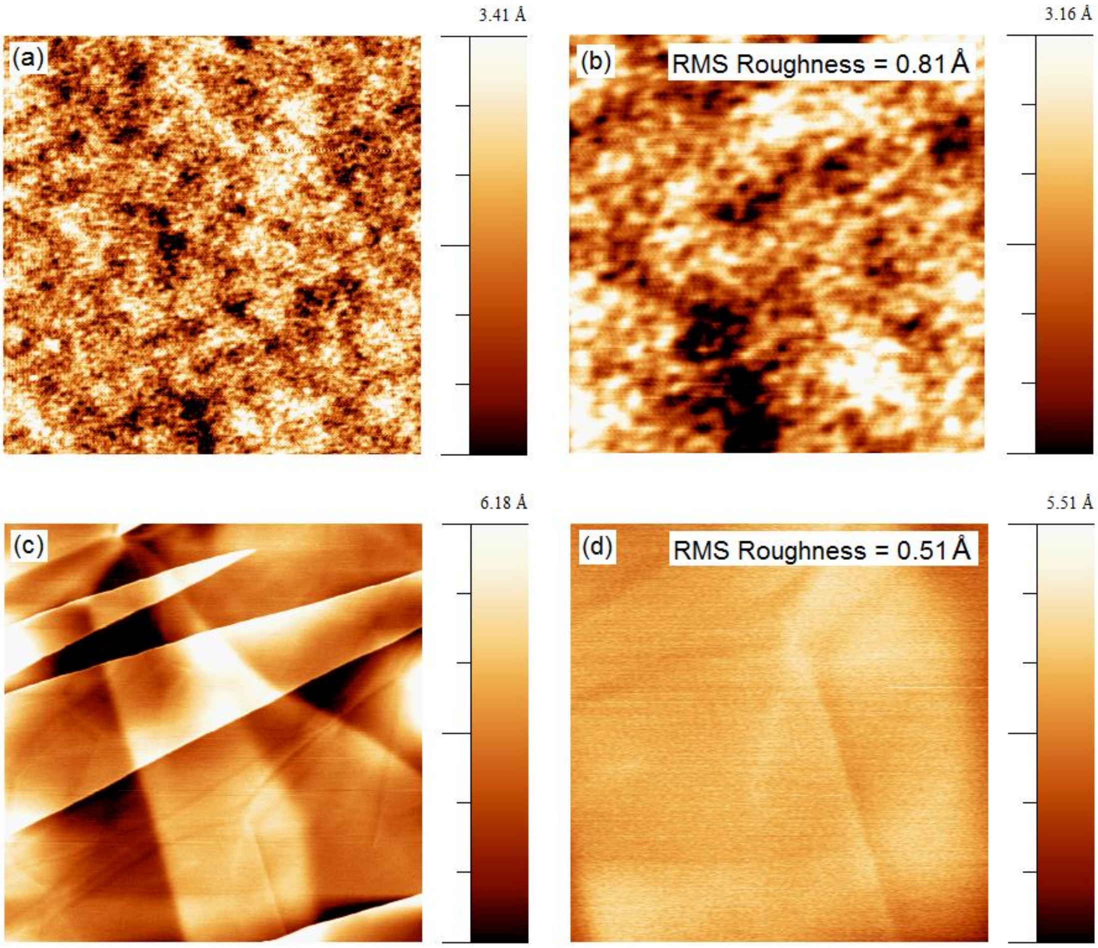

Figure 2.5. *(a) 1.5 x 1.5 μm² AFM topography image of a graphene flake after cleaning. (b) 500 x 500 nm² AFM topography image of a graphene flake after cleaning. (c) 1.5 x 1.5 μm² AFM topography image of HOPG. (d) 500 x 500 nm² AFM topography image of HOPG. Comparison of the RMS roughness demonstrates that graphene flakes are more rough than HOPG.*

2.4 Raman spectroscopy

Raman spectroscopy provides information about the vibrational properties of a system, by detecting and analyzing inelastically scattered light following its excitation by monochromatic laser light. Unlike classical absorption processes, scattering of light does not require matching of the incident radiation to the energy difference between ground and excited states of the molecules [91]. In scattering processes, the light interacts with the molecule and polarizes the electron cloud around the nuclei to form a short-lived state (*i.e.* a virtual state). As the energy level of this virtual state is classically not allowed, the photon is almost instantaneously reradiated. One can now distinguish different types of scattering mechanisms depending on the initial and final vibrational state of the molecule, as illustrated in Figure 2.6. Most probably, the light is reradiated at the same frequency of the incoming beam and this process is referred to as elastic scattering (also called Rayleigh scattering). However, it occasionally happens that the reradiated light is of lower (higher) frequency than the excitation frequency and the molecules are left behind in a higher (lower) vibrational state. This type of scattering is referred to as inelastic scattering (also called Raman scattering) and a further distinction is made between Stokes and anti-Stokes scattering for light scattered at lower and higher frequencies, respectively. Since anti-Stokes radiation requires that the molecule was originally in an excited vibrational state, this type of radiation is generally less intense than Stokes radiation [92]. However, the total radiation scattered inelastically is extremely small (one in every 10^6 - 10^8 scattered photons [91]), and sensitive instruments are needed for its study.

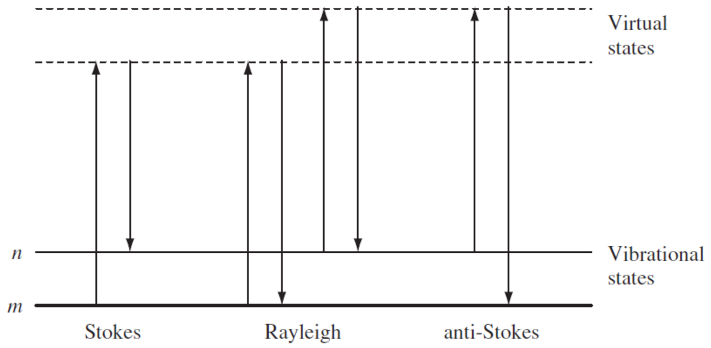

Figure 2.6. *Diagram showing the different scattering processes when a substance is irradiated with monochromatic light. Most often, light is scattered elastically, a process referred to as Rayleigh scattering. Alternatively, light can be scattered inelastically (Raman scattering), leaving the molecules behind a higher (Stokes scattering) or lower (anti-Stokes scattering) vibrational state. (Adapted from ref.* [91]*)*

To increase the efficiency of the scattering process, one can adjust the frequency of the incoming laser beam to match the frequency of an electronic transition in the substance (*i.e.* resonance Raman scattering). In this way, the scattering is generally enhanced by a factor of 10^3 – 10^4 [91]. Fortunately, Raman scattering in graphene is always resonant because of the linear E($\vec{k}$) dispersion relation (Eq. (4)) around the Dirac points [93]. In fact, Raman spectroscopy is one of the most powerful techniques to characterize graphene as it yields an unique fingerprint of the graphene material properties and in this way can be used to assess the number of layers, strain, doping and disorder of graphene.

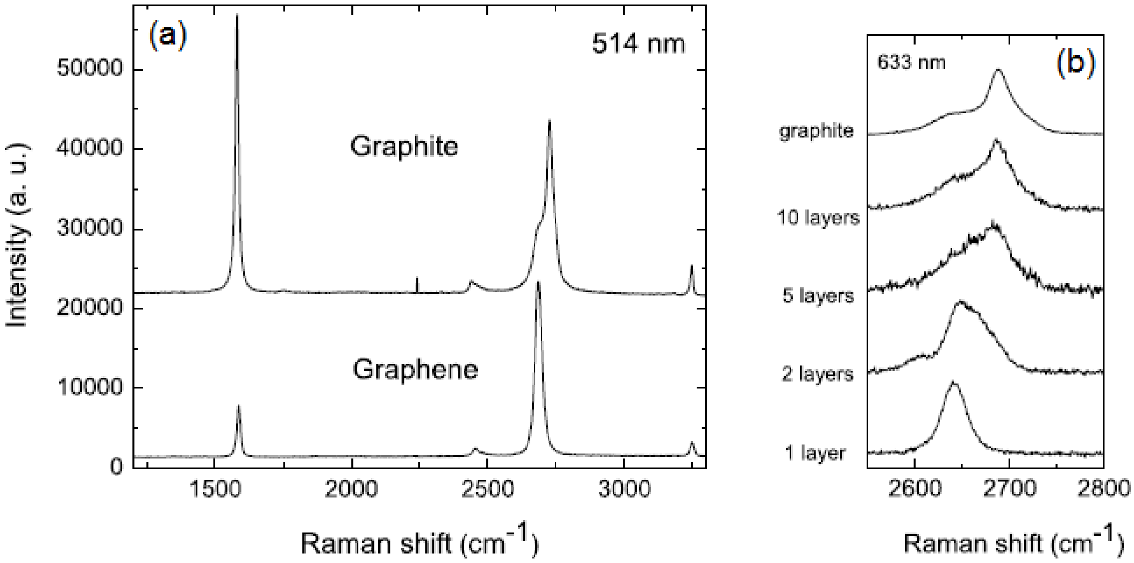

Figure 2.7. *(a) Typical Raman spectrum for SLG and bulk graphite, recorded with an excitation wavelength of 514 nm. Both spectra are normalized to have the same intensity of the 2D peak. (b) Evolution of the 2D-peak with the number of layers, recorded with an excitation wavelength of 633 nm. (Adapted from ref.* [90]*)*

Typically, the Raman spectrum of graphene contains three distinct peaks [94]. First, there is the so-called G peak which shows a narrow band around 1580 cm^{-1} and is attributed to the stretching modes of the sp^2 carbon bonds. Second, there is a very sharp peak around 2630 cm^{-1} which is referred to as the 2D peak and originates from the breathing modes of the sp^2 carbon bonds. These breathing modes also give rise to a third peak, which is the D peak and which typically appears in the spectrum around 1315 cm^{-1}. In fact, the 2D peak is the second-order of the D peak and is always present in graphene, while the D peak only appears when disorder is extant in the graphene lattice. The intensity ratio of the D peak over the G peak (I_D/I_G) is therefore often used as a measure of the crystalline quality of the graphene sheet [94]. The 2D peak on the other hand exhibits a particular shape depending on the number of interacting graphene layers and can therefore be employed to determine the number of layers [90], [95]. The latter is well illustrated in Figure 2.7.

Another purpose for which Raman spectroscopy can be employed is to monitor doping of graphene [96], [97]. In general, the G peak shifts towards larger wavenumbers and sharpens for both electron and hole doping. The 2D peak, on the other hand, shows a different response to electrons and holes. For electron doping the position of the 2D peak does not shift significantly. For large n-type doping levels, however, a shift of the 2D peak towards smaller wavenumbers is observed. For p-type doping the peak shifts to larger wavenumbers, even for moderate doping levels. Remarkable is also the strong dependence of the 2D peak intensity on electron or hole doping, while the intensity of the G peak is much less dependent on doping levels. Therefore, the intensity ratio I_{2D}/I_G is a sensitive parameter to monitor doping levels in graphene

The G and 2D Raman mode are also highly sensitive to strain in the graphene sheet. Unfortunately, strain is often uncontrollably introduced during various processing steps needed for the production of graphene flakes or graphene devices, thus complicating the correct interpretation of doping effects. Lee *et al.* suggested a simple approach to overcome this issue [98]. Their method is based on a plot of the position of the 2D peak (Pos(2D)) *vs.* the position of the G peak (Pos(G)) and graphically allows one to separate strain from doping. The underlying explanation is the following:

- For strain the slope of Pos(2D) vs. Pos(G) is 2.2 ± 0.2 for uniaxial strain and between 2.25 and 2.8 for biaxial strain
- For hole doping the slope of Pos(2D) *vs.* Pos(G) is 0.70 ± 0.05
- For electron doping the relationship of Pos(2D) *vs.* Pos(G) becomes more nonlinear for high charge density

This is well illustrated in Figure 2.8 for three different graphene flakes before and after thermal annealing in vacuum. Before annealing, the data points for each flake form a line, corresponding to variations expected under uniaxial strain. Thermal annealing resulted in hole doping of the flakes due to an increased coupling with the Si/SiO_2 substrate, as a result of which the data points have moved along a line corresponding to variations in hole concentration. After thermal annealing, the data points are again on a line corresponding to variations under uniaxial stress. The authors also claim that thermal annealing removes native tensile strain and induces compressive strain.

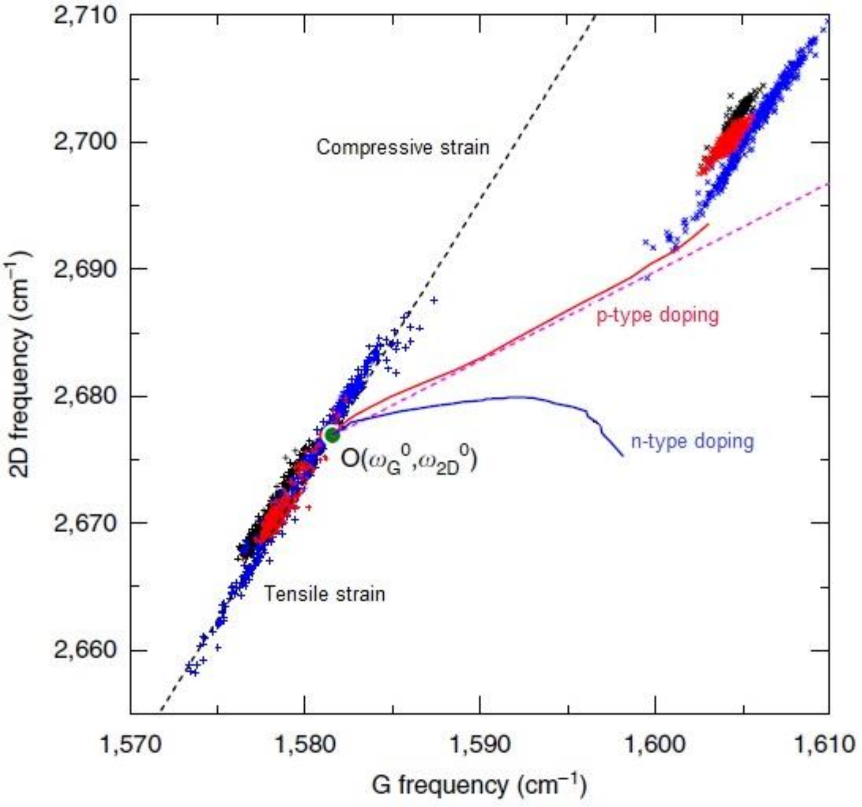

Figure 2.8. *Plot of Pos(2D) vs. Pos(G) for three different graphene flakes (blue, red and black) before (+) and after (x) thermal annealing at 400 °C. The green dot was obtained for freely suspended graphene and corresponds to unstrained, charge-neutral graphene. The black dashed line corresponds to the expected trend under uniaxial strain. The pink and blue solid line represent the experimental evolution of strain-free graphene for hole and electron doping, respectively. The pink dashed line corresponds to an average of experimental data points obtained for strain-free graphene under different hole doping levels. (Adapted from ref.* [98]*)*

All Raman spectra in this work were obtained in a backscattering geometry in ambient conditions using a 100x objective lens (numerical aperture = 0.7). A He/Ne laser (JDSU) operated at a wavelength of 633 nm was used as the excitation source. Scattered light was captured with a CCD detector cooled at -100 °C (Andor Technology). Data were analyzed with Matlab 8.3 and OriginPro 8.

2.5 Graphene field effect devices

Field effect devices were produced in order to electrically characterize the doping level of graphene. The production and characterization of these devices is described below.

2.5.1 Production process

Graphene field effect devices were produced using a standard photolithography procedure. Because the main objective is to characterize doping levels, no shaping of the graphene was performed. Instead flakes were chosen with an elongated shape (Figure 2.9a). The photolithography procedure used to deposit the metal contacts consisted of the following steps:

- Spincoating a positive photoresist (IX 845) at 4000 rpm for 30 s
- Annealing the photoresist for 1 min at 120 °C
- Selective irradiation of the photoresist with UV light, using an appropriate mask. The alignment is performed with a Karl Suss MA6 machine.
- Development of the applied pattern using a positive photoresist developer (OPD 5262) for 60 s. Afterwards the sample is cleaned in DI water.
- Deposition of Ti(1 nm)/Pd(50 nm) metal contacts.
- Lift-off in acetone at 50 °C for ± 8 h, then in acetone at room temperature for ± 2 days.
- IPA cleaning for 10 min at room temperature

Optical microscopy images of a device after fabrication are shown in Figure 2.9. As can be seen, four probe structures were deposited. The major drawback of this photolithography procedure is the direct deposition of a photoresist on the graphene flakes, which results in unclean graphene devices because of photoresist residues. In an attempt to clean the devices, they were subjected to a forming gas treatment (20 h at 300 °C and 7×10^{-5} bar, ramp up = 1 °C/min, cool down = 1 °C/min). However, as illustrated in Appendix 1, thermal annealing results in p-type doping of the graphene flakes because of an increased interaction with the substrate.

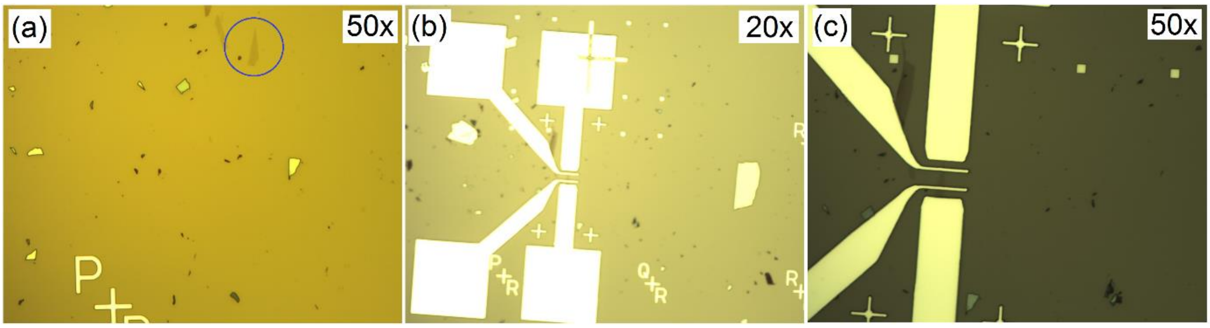

Figure 2.9. *(a) Graphene flake with an elongated shape (highlighted by a blue circle). (b),(c) Graphene flake shown in (a) after device fabrication.*

2.5.2 Electrical characterization

Although four probe structures were fabricated, only two probe measurements were performed on the inner two contacts. As shown in Figure 2.10 these inner contacts form a transistor structure with a channel length (d_{Ch}) of 10 µm.

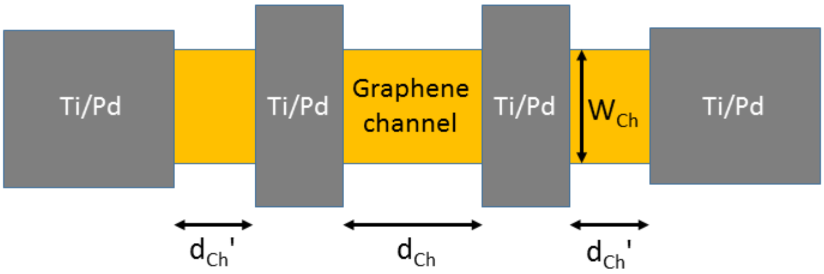

Figure 2.10. *Schematic representation of the graphene field effect devices as measured in this work.*

In a two probe measurement, the drain current (I_d) is measured as a function of back-gate voltage[8] (V_g) in order to extract the transfer characteristic. This transfer characteristic allows to extract the CNP and the mobility of the charge carriers. The CNP corresponds to the back-gate voltage where the drain current is at a minimum. According to the parallel plate capacitor model, the charge carrier concentration (n) can be deduced from the position of the CNP according to:

$$n = \frac{\epsilon \cdot \epsilon_o}{t_{ox} \cdot e} \cdot V_{g,CNP} = \frac{C_{ox}}{e} \cdot V_{g,CNP}, \qquad \text{Eq. (9)}$$

in which ϵ and ϵ_o are the relative permittivity of SiO_2 and the vacuum permittivity, respectively, t_{ox} is the thickness of the SiO_2 layer, e is the elementary charge, and C_{ox} is the capacitance of the SiO_2 layer.

The mobility (µ) can be extracted from the transfer characteristic according to:

$$\mu = \frac{d_{Ch}}{C_{ox} \cdot W_{Ch} \cdot V_d} \frac{dI_d}{dV_g}\bigg|_{max}, \qquad \text{Eq. (10)}$$

in which d_{Ch} and W_{Ch} are the length and width of the channel, respectively, and V_d is the drain voltage. However, because in this work no shaping of the graphene was performed, the channel width (W) is ill-defined. Thus, quantitative mobility values cannot be extracted. Nevertheless, it is possible to compare the relative mobilities before and after functionalization of a flake.

---

[8] Back-gate voltage and drain voltage are always expressed with respect to the source.

All measurements were performed with a Keithley 4200-SCS device under N_2 atmosphere and a drain voltage of 100 mV was applied. Data were analyzed with OriginPro 8.

2.6 Chemicals

Table 2.1 gives a list of chemicals that were used throughout this work. All chemicals were used without any further purification. Issues related to safety, health and environmental effects are discussed in Appendix 2.

Table 2.1. *List of chemicals used throughout this work.*

Name	Formula	Supplier	Purity
1-Phenyloctane	$C_6H_5C_8H_{17}$	Sigma-Aldrich	98 %
Acetone	CH_3COCH_3	KMG Electronic Chemicals, Inc.	n.a.
Ethanol	C_2H_5OH	Merck KGaA	≥ 99.9 %
Isopropylalcohol	$CH_3CHOHCH_3$	KMG Electronic Chemicals, Inc.	n.a.
IX 845	n.a.	JSR Micro NV	n.a.
Octadecylamine	$n\text{-}C_{18}H_{37}NH_2$	Sigma-Aldrich	≥ 99.9 %
OPD 5262	n.a.	Fujifilm	n.a.
Pentacontane	$n\text{-}C_{50}H_{102}$	Sigma-Aldrich	≥ 97.0 %
Toluene	$C_6H_5CH_3$	Sigma-Aldrich	≥ 99.9 %
		Sigma-Aldrich	≥ 99.7 %

Chapter 3: Results and discussion

3.1 Self-assembly on HOPG

To find the optimal conditions for the deposition of a high quality pentacontane (C_{50}) layer on graphene, self-assembly of C_{50} on HOPG is first investigated. Once the conditions for the deposition of C_{50} on HOPG are optimized, self-assembly of octadecylamine (ODA) on both bare and C_{50}-functionalized HOPG is studied. Comparison of the self-assembly behavior of ODA on these different substrates will give information on the effect of the substrate and will allow to get an idea of the coverage of ODA on C_{50}-functionalized HOPG.

3.1.1 Pentacontane on HOPG

The self-assembly behavior of C_{50} on HOPG was investigated using room temperature STM. C_{50} was dissolved in toluene and subsequently dropcasted on a freshly cleaved HOPG surface. Toluene was chosen over the more classical STM solvents (such as *e.g.* 1-phenyloctane) because toluene readily evaporates, leaving behind a dry surface as required for practical graphene devices. This eliminates the need for a washing step in which the excess solvent is rinsed away.

Figure 3.1 shows typical STM images obtained at different scales. Figure 3.1a is a high resolution STM image revealing sub-molecular details. The image was drift corrected using an image of the graphite lattice obtained immediately after the original image. Figure 3.1b illustrates how the C_{50} molecules assemble in parallel lamellar structures. The C_{50} molecules are oriented perpendicular to the lamellar direction in an all-trans conformation. The inset in Figure 3.1a shows the high symmetry axes of the underlying graphite lattice, indicating that the lamellae align along the high symmetry graphite axes. The lamellar width (unit cell parameter a), as obtained from this image, equals 6.77 ± 0.04 nm, what is in good agreement with ref. [78]. Figure 3.1c confirms the self-assembly motif of C_{50} on HOPG. Interesting are the structures oriented at an angle of 90° with respect to the main lamellar direction. These structures are typically observed at higher concentrations. It is suggested in ref. [99] that these structures are bilayer structures in which the C_{50} molecules of the upper layer are rotated over 90° with respect to those of the lower layer. According to symmetry considerations this arrangement is only possible when the carbon backbone plane of the lower C_{50} layer is oriented perpendicular to the graphite basal plane. Alternatively, when the carbon backbone plane of the lower C_{50} layer is parallel to the graphite basal plane, the upper C_{50} layer is oriented at typical angles of 120° with respect to the lower C_{50} layer. Figure 3.1d is a larger scale STM image showing the formation of different domains consisting of parallel lamellae. Typically an angle of 60° is observed between adjacent domains, consistent with the trigonal symmetry of the underlying graphite lattice.

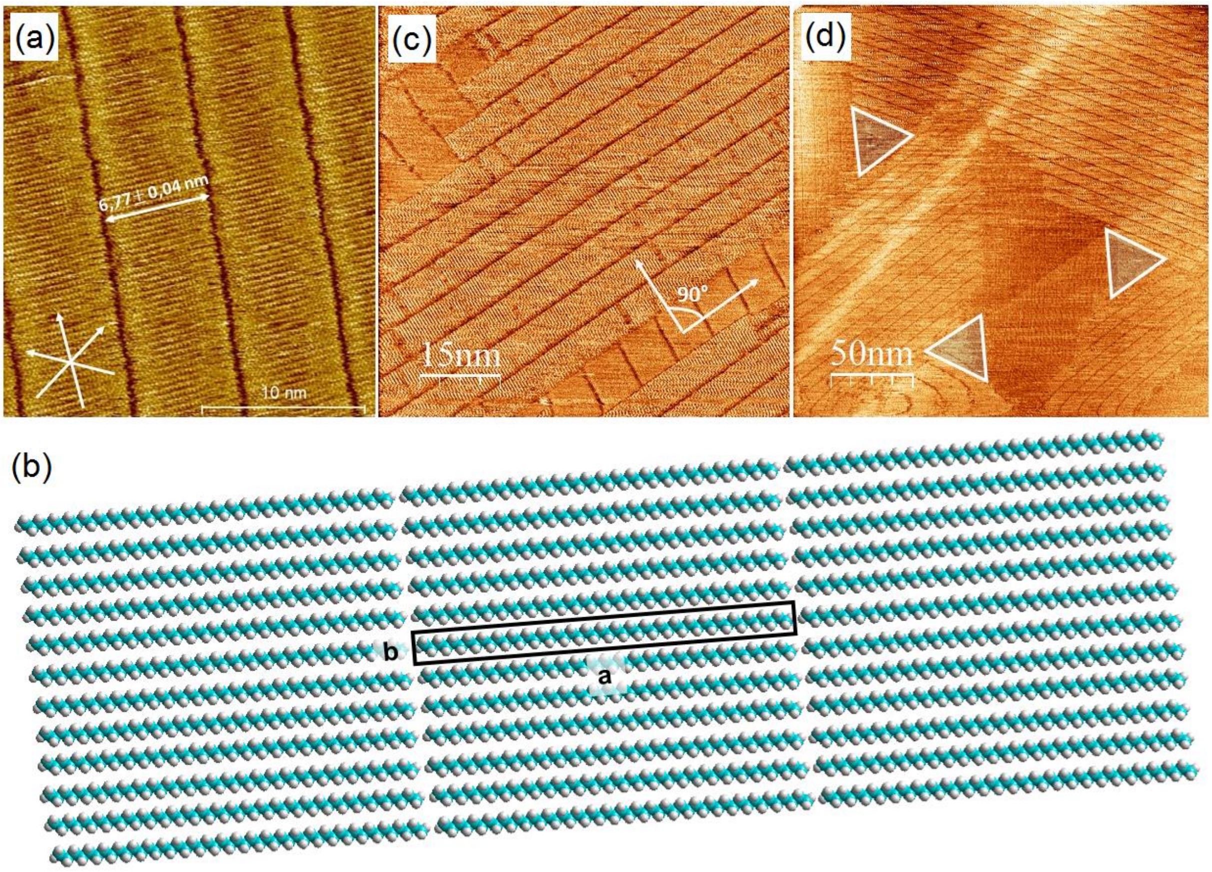

Figure 3.1. *Room temperature STM images of C_{50} dropcasted on a freshly cleaved HOPG surface. (a) 20 x 20 nm^2 high resolution image revealing sub-molecular details. (Concentration = 10x dilution of a saturated toluene solution; $U_{t,sample}$ = -0.65 V; I_t = 0.155 nA). (b) Molecular model illustrating how the C_{50} molecules in (a) self-assemble in parallel lamellae. The unit cell is indicated by a black box. (Green = carbon; white = hydrogen). (c) 75 x 75 nm^2 image showing the formation of structures perpendicular to the main lamellar orientation. (Concentration = saturated toluene solution; $U_{t,sample}$ = 0.95 V; I_t = 0.180 nA). (d) 250 x 250 nm^2 image showing the formation of different domains. The superimposed triangles clearly demonstrate the angle of 60° between adjacent domains. (Concentration = saturated toluene solution; $U_{t,sample}$ = 0.95 V; I_t = 0.180 nA).*

Optimization of the C_{50} layer was performed by comparing the domain sizes that were obtained when using different deposition techniques and concentrations. More specifically, drop-casting from a saturated toluene solution[9], drop-casting from a 10x dilution of a saturated toluene solution and dip-coating in a 10x dilution of a saturated toluene solution were compared. Figure 3.2 shows representative STM images obtained under the aforementioned conditions. Comparing Figure 3.2a to Figure 3.2b illustrates that fewer domains are formed when C_{50} is drop-casted from a more diluted solution. This observation is perfectly reasonable because at lower concentration fewer nucleation events happen, leading to fewer and larger domains after domain growth. Figure 3.2b and Figure 3.2c were obtained for a drop-casted and dip-coated C_{50} layer, respectively. Comparison of these two images reveals that dip-coating leads to larger domain sizes compared to drop-casting. The explanation for this observation is not clear. It could be that the structures formed by drop-casting are kinetically trapped because solvent evaporation was too fast. Alternatively (or in addition), the flow induced during withdrawal of the substrate, when dip-coating, can lead to a preferred orientation of the lamellae, resulting in fewer and larger domains. It is, for instance, well-known that flow can affect the orientation of self-assembled structures [100].

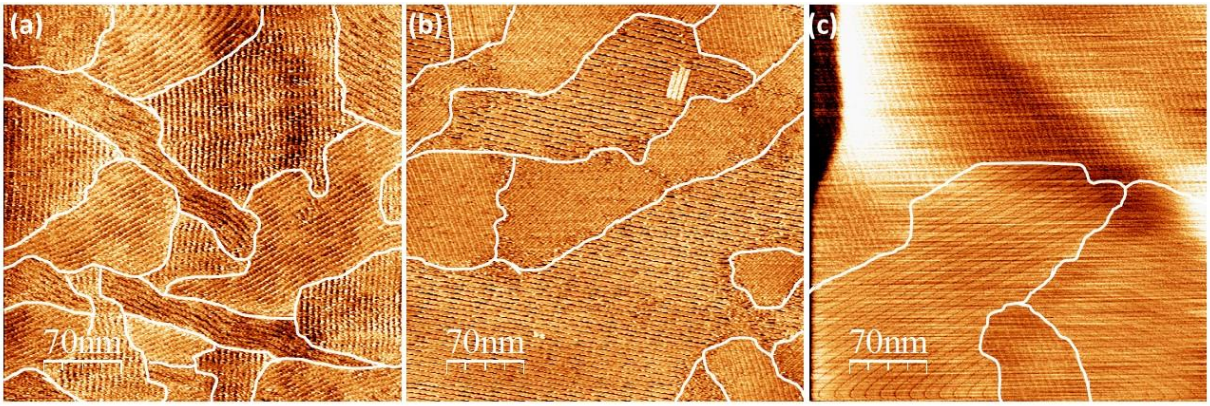

Figure 3.2. *Effect of concentration and deposition method on domain size. (a) 350 x 350 nm^2 STM image obtained by drop-casting C_{50} from a saturated toluene solution. ($U_{t,sample}$ = -0.85 V; I_t = 0.100 nA). (b) 350 x 350 nm^2 STM image obtained by drop-casting C_{50} from a 10x dilution of a saturated toluene solution. ($U_{t,sample}$ = -0.35 V; I_t = 0.255 nA). (c) 350 x 350 nm^2 STM image obtained by dip-coating C_{50} from a 10x dilution of a saturated toluene solution. ($U_{t,sample}$ = 0.90 V; I_t = 0.180 nA). Fewer and larger domains are formed at lower concentrations and for dip-coated samples.*

In order to statistically support the observation made in Figure 3.2, a series of images were compared for each of the aforementioned conditions. All images were obtained at a 350 x 350 nm^2 scale and the domain sizes were indirectly compared by

---

[9] The concentration of a saturated toluene solution is estimated to be ~ 10^{-4} M.

counting the number of domains present in each image. Thus, the fewer domains that are present, the larger the domain sizes. The results are shown in Figure 3.3, clearly indicating that the largest domains are formed when lower concentrations are used and when dip-coating is used instead of drop-casting.

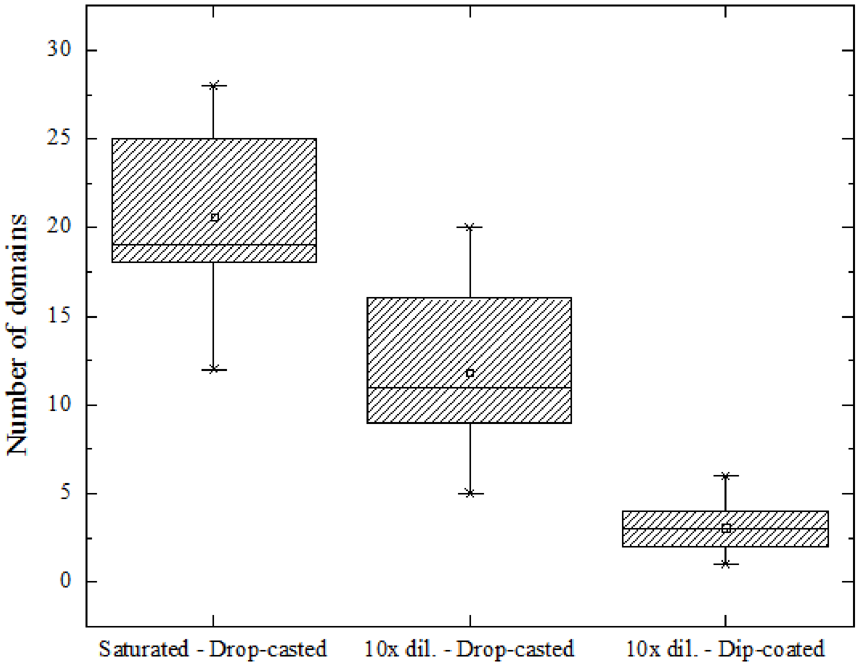

Figure 3.3. *Boxplot diagram representing the number of domains on a 350 x 350 nm^2 STM image obtained for different concentrations and deposition techniques. It is clear that the fewest domains are present for the lowest concentration and for the dip-coating method.*

In order to reach the largest possible domain sizes, dip-coating in more diluted solutions was investigated. The C_{50} domains obtained in this way became that large that STM was no longer the most suited imaging technique. Instead, AFM was employed to get an idea of the domain sizes and uniformity of the C_{50} layer on a larger scale. Figure 3.4 shows representative AFM images obtained by dip-coating a freshly cleaved graphite substrate in a 500x and 1000x dilution of a saturated toluene solution. The lamellae are hardly visible in the topography images due to the large scan size. However, they can readily be observed in the corresponding phase images. Moreover, the fast Fourrier transform (FFT) of the phase images indicates a periodicity of ~ 6.8 nm, corresponding well to the lamellar width of C_{50} as previously obtained with STM (~ 6.77 nm). These images demonstrate that dip-coating in very diluted solutions leads to a homogeneous C_{50} film, comprising extremely large domains extending over

> 1 μm. In fact, it appears that the main factor limiting domain sizes is the presence of step-edges and defects on the HOPG surface.

It must be noted that a 1000x dilution resulted in incomplete coverage when the sample was withdrawn after only 10 min residence in the solution and at a slightly higher speed (1 mm/min). This indicates that a 1000x dilution is the very limiting case where still a continuous C_{50} layer can be formed. Therefore, a 500x dilution has been chosen as the optimal concentration to deposit a high quality C_{50} passivation layer on graphene.

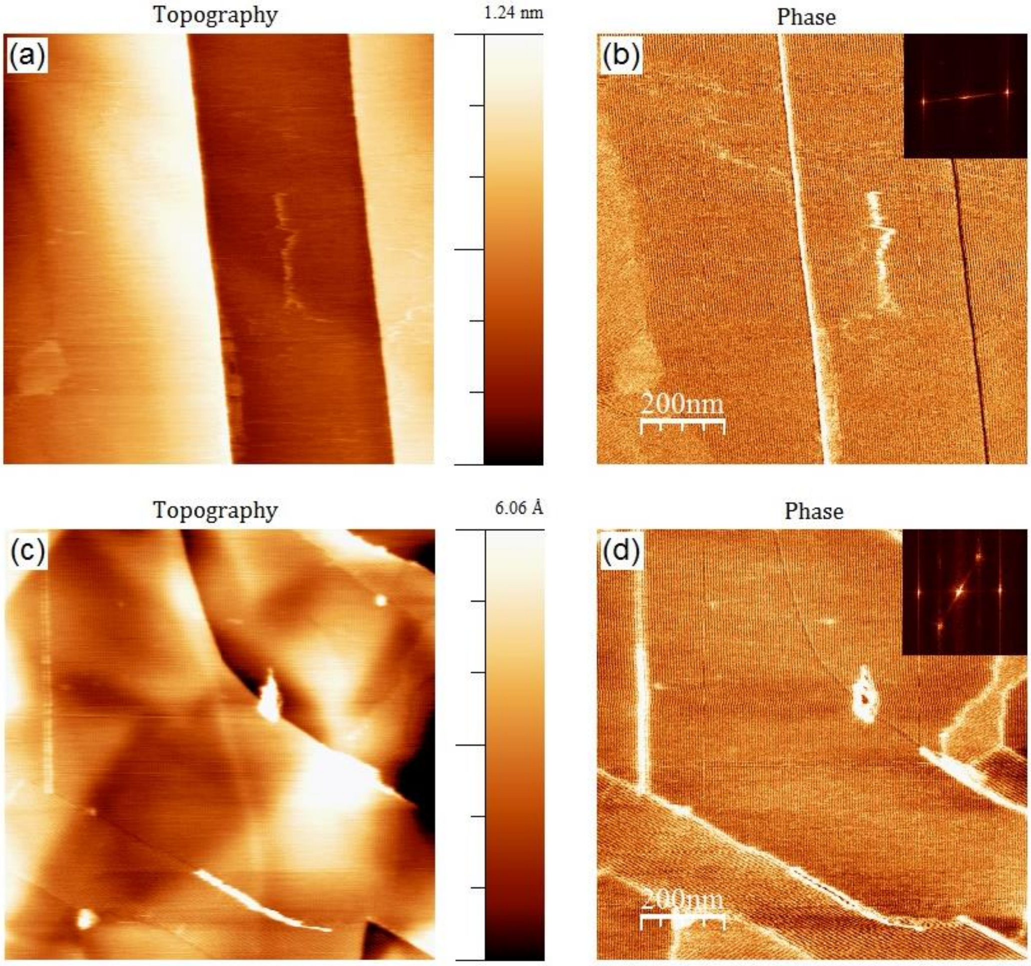

Figure 3.4. *1 x 1 μm² AFM images of (a),(b) C_{50} dip-coated from a 500x dilution of a saturated toluene solution and (c),(d) C_{50} dip-coated from a 1000x dilution of a saturated toluene solution. Topography images are shown on the left and the corresponding phase images are shown on the right. The inset in the phase images indicates a periodicity of ~ 6.8 nm.*

3.1.2 Octadecylamine on HOPG

To assess the self-assembly behavior of ODA on graphene, self-assembly on HOPG was first investigated using room temperature STM. ODA was dissolved in 1-

phenyloctane (3.7×10^{-2} M) and subsequently drop-casted on a freshly cleaved HOPG surface. Figure 3.5a displays a high resolution STM image revealing sub-molecular details. Figure 3.5b illustrates how the ODA molecules assemble parallel to each other, forming extended lamellar structures in which the carbon backbone adopts an all-trans conformation. Next to Van der Waals stabilization between the carbon backbones, the molecules are stabilized by a hydrogen bonded network between adjacent amino groups. Hence, the molecules self-assemble in a head-to-head/tail-to-tail type arrangement, giving rise to alternating rows of brighter (→) and darker contrast (→). According to ref. [101] the brighter regions are to be attributed to the amino groups and the darker regions are due to deep troughs separating adjacent carbon chains. After a proper drift correction, the lamellar width (lattice cell parameter a) was determined to be 4.87 ± 0.09 nm.

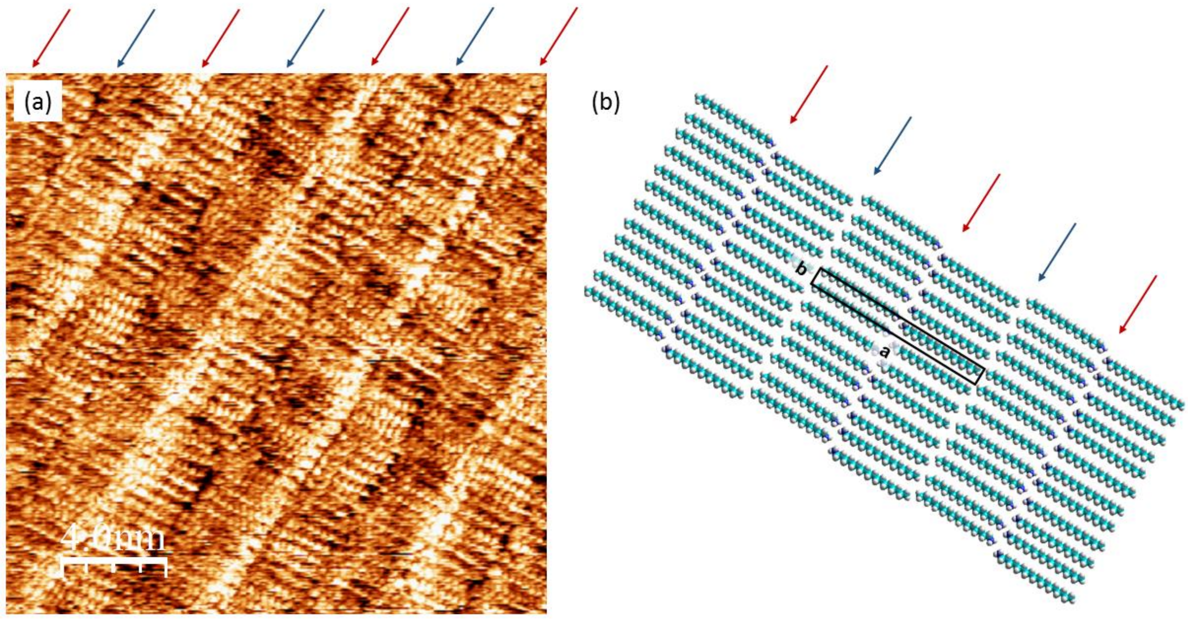

Figure 3.5. *(a) 20 x 20 nm^2 high resolution STM image of ODA on HOPG, dropcasted from a 3.7×10^{-2} M solution in 1-phenyloctane. ($U_{t,sample} = 0.90$ V; $I_t = 0.040$ nA). (STM image courtesy of J. Teyssandier) (b) Molecular model illustrating how the ODA molecules self-assemble in a head-to-head/tail-to-tail type arrangement forming hydrogen bonds between adjacent amino groups. Consequently, alternating rows of brighter (amino groups; →) and darker (troughs; →) contrast can be discerned. The unit cell is indicated by a black box. (Green = carbon; white = hydrogen; blue = nitrogen).*

Next, AFM measurements were performed to evaluate the self-assembly behavior of ODA on larger scales and because ODA proved difficult to visualize with STM. For these and the following experiments involving ODA, ethanol was chosen as the solvent because ethanol easily evaporates, creating a dry surface as required for practical graphene devices. Moreover, in view of future experiments in which ODA will be deposited on a C_{50} layer, ethanol has the main advantage that it does not dissolve C_{50}. Consequently, depositing ODA from ethanol on a C_{50} layer is expected to leave the C_{50} layer intact. Figure 3.6 shows the AFM images obtained for dip-coating a freshly cleaved HOPG substrate in ethanol solutions of ODA at different concentrations. A comparison of these images learns that dip-coating in more concentrated solutions leads to an increased surface coverage, yielding monolayer coverage at 5 x 10^{-5} M. Taking a FFT, as shown in Figure 3.6d, indicates a periodicity of ~ 4.9 nm, which is comparable to the lamellar width of ODA as previously obtained with STM (~ 4.87 nm).

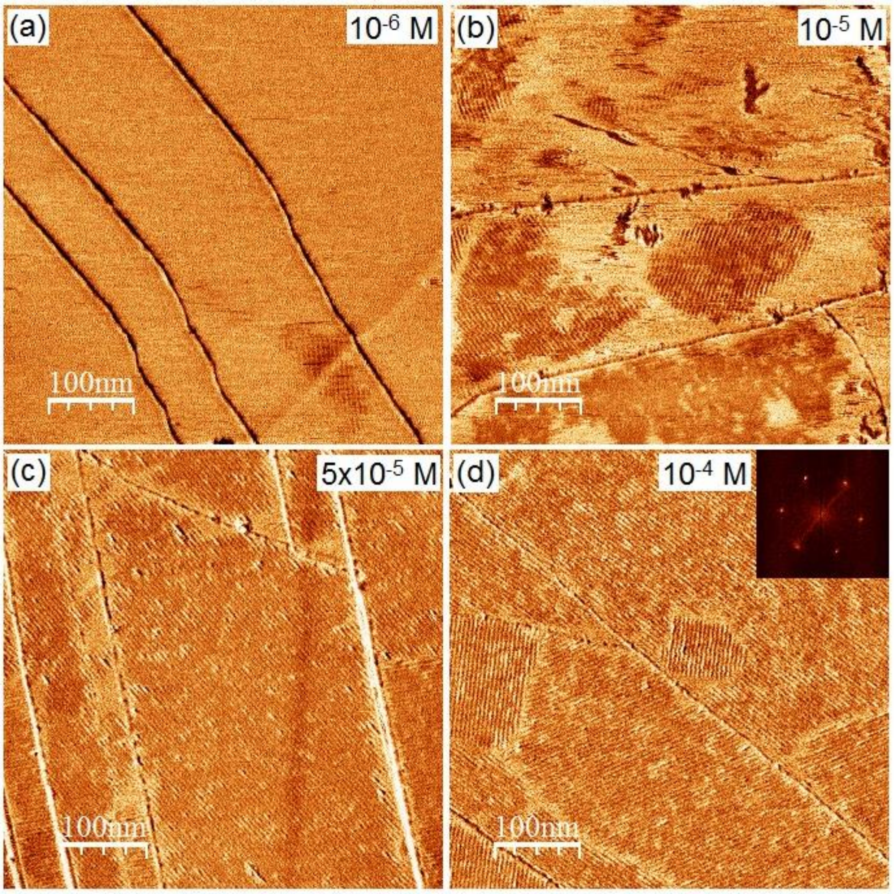

Figure 3.6. *500 x 500 nm^2 AFM phase images of ODA on HOPG, dip-coated from an ethanol solution at concentrations of (a) 10^{-6} M, (b) 10^{-5} M, (c) 5 x 10^{-5} M and (d) 10^{-4} M. Dip-coating from more concentrated solutions results in a higher surface coverage, yielding monolayer coverage at 5 x 10^{-5} M. The inset in (d) shows the FFT from which a lamellar width of ~ 4.9 nm was deduced.*

3.1.3 Octadecylamine on C_{50}-functionalized HOPG

In order to understand the self-assembly behavior of ODA on a C_{50}-functionalized graphene surface, control experiments assessing self-assembly of ODA on a C_{50}-

functionalized HOPG surface were first conducted using room temperature STM. A freshly cleaved HOPG substrate was first dip-coated in a 1000x dilution of a saturated C_{50} in toluene solution. Next, ODA was deposited by dip-coating the C_{50}-functionalized HOPG substrate in a 10^{-5} M ODA in ethanol solution. To facilitate imaging, one drop of 1-phenyloctane was added. Figure 3.7 shows two STM images of ODA on C_{50}, obtained from consecutive scans. It is apparent that the C_{50} layer can be resolved, but the ODA adlayer appears hazy. Moreover, comparing Figure 3.7a to Figure 3.7b demonstrates that the ODA adlayer can be slightly moved in between consecutive scans. These results indicate that ODA is only weakly adsorbed on the C_{50} layer. Therefore, the inability to image a resolved structure of ODA on C_{50} could be due to the fact that ODA molecules are too mobile on the C_{50} surface. Also, the fact that both C_{50} and ODA are non-conductive molecules might hamper imaging with STM.

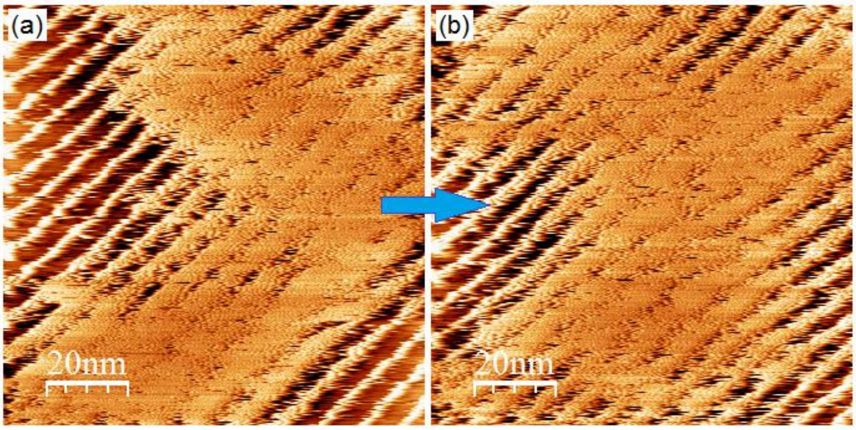

Figure 3.7. *100 x 100 nm^2 STM images of ODA on a C_{50} layer. The images were obtained during consecutive scans as indicated by the blue arrow. The C_{50} layer can readily be resolved, while the ODA adlayer appears hazy and can be moved in between consecutive scans. This indicates that ODA is only weakly adsorbed on the C_{50} layer. C_{50} was deposited by dip-coating a freshly cleaved HOPG substrate in a 1000x dilution of a saturated toluene solution. ODA was deposited by dip-coating from a 10^{-5} M ethanol solution. One drop of 1-phenyloctane was added to facilitate imaging. ($U_{t,sample}$ = -0.950 V; I_t = 0.180 nA)*

Next, AFM measurements were performed to investigate the self-assembly of ODA on a C_{50}-functionalized HOPG surface on larger scales. The samples were again prepared by two subsequent dip-coating steps: first in a 1000x dilution of a saturated C_{50} in toluene solution, and then in a ODA in ethanol solution of varying concentration. Figure 3.8 shows that the surface coverage of ODA on a C_{50}-functionalized HOPG surface increases when the sample is dip-coated in more concentrated solutions. It is important to notice that the C_{50} layer is still intact after dip-coating in the ODA solution, as proven by the fact that the C_{50} lamellae are still visible in the background of the phase images (*e.g.* Figure 3.8f). Taking a FFT of Figure 3.8f yields a periodicity of ~ 6.5 nm, confirming that the lamellae in the background are due to the C_{50} layer and not due to ODA. However, there is a striking difference when these images are compared to those in Figure 3.6: while monolayer coverage of ODA on HOPG was achieved for dip-coating in a 5 x 10^{-5} M solution, the coverage of ODA on C_{50}-functionalized HOPG is much lower, even when dip-coated in much more concentrated solutions. This means that ODA has a much lower affinity to self-assemble on C_{50} than on graphite. Moreover, looking at the height profile in Figure 3.8e demonstrates that ODA preferably forms multi-layered structures, even more so when dip-coating in more concentrated solutions. Again, this demonstrates the low affinity of ODA to self-assemble on C_{50}. Instead, ODA prefers to stack on top of other ODA molecules forming multi-layered clusters. Based on these observations, the following sequence of affinity of ODA for different surfaces can be deduced: HOPG > ODA > C_{50}, meaning that ODA shows the highest affinity to self-assemble on HOPG and will try to preclude self-assembly on C_{50} by stacking on molecules of its one kind.

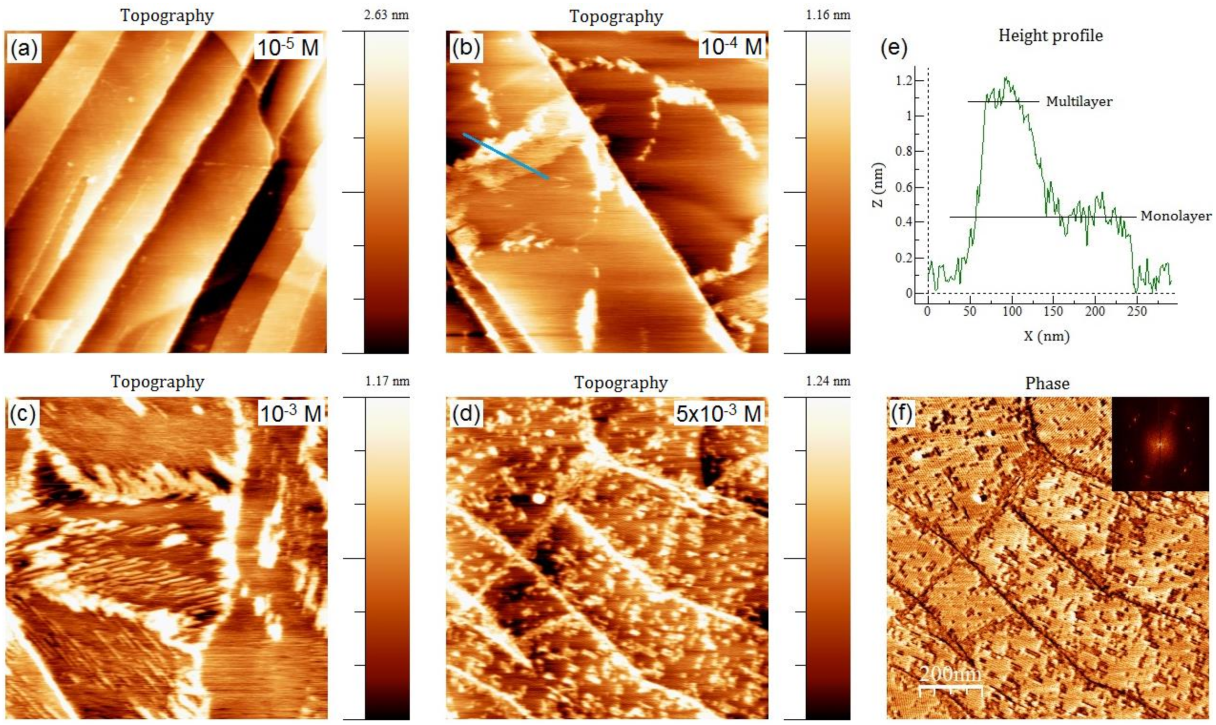

Figure 3.8. *1 x 1 µm^2 AFM topography images of a C_{50}-functionalized HOPG surface dip-coated in ODA in ethanol solutions of varying concentration: (a) 10^{-5} M, (b) 10^{-4} M, (c) 10^{-3} M, and (d) 5 x 10^{-3} M. Dip-coating in more concentrated ODA solutions leads to increased surface coverage. (e) Height profile along the blue line in (b). Next to monolayer, ODA preferably forms multi-layered structures. (f) Phase*

image of (d) showing the presence of lamellae in the background. The inset shows a FFT indicating a periodicity of 6.5 nm, clearly proving that the lamellae in the background are due to C_{50}.

While STM failed to image the specific structure formed by ODA on a C_{50}-functionalized HOPG surface, in some particular cases, where monolayer structures of ODA on C_{50} were present, it was possible to image the structure with AFM. This is illustrated in Figure 3.9, which was obtained for dip-coating a C_{50}-functionalized HOPG substrate in a 10^{-4} M ODA in ethanol solution. Taking the FFT of Figure 3.9b shows that lamellae with two different periodicities are present. The smallest periodicity corresponds to ~ 5.7 nm and the largest periodicity equals ~ 7.0 nm, which must be attributed to ODA and C_{50}, respectively. This indicates that when ODA self-assembles on C_{50} it does so by forming lamellae similar to what was observed on bare HOPG. Interestingly, it is observed that the ODA lamellae follow the direction of the underlying C_{50} lamellae.

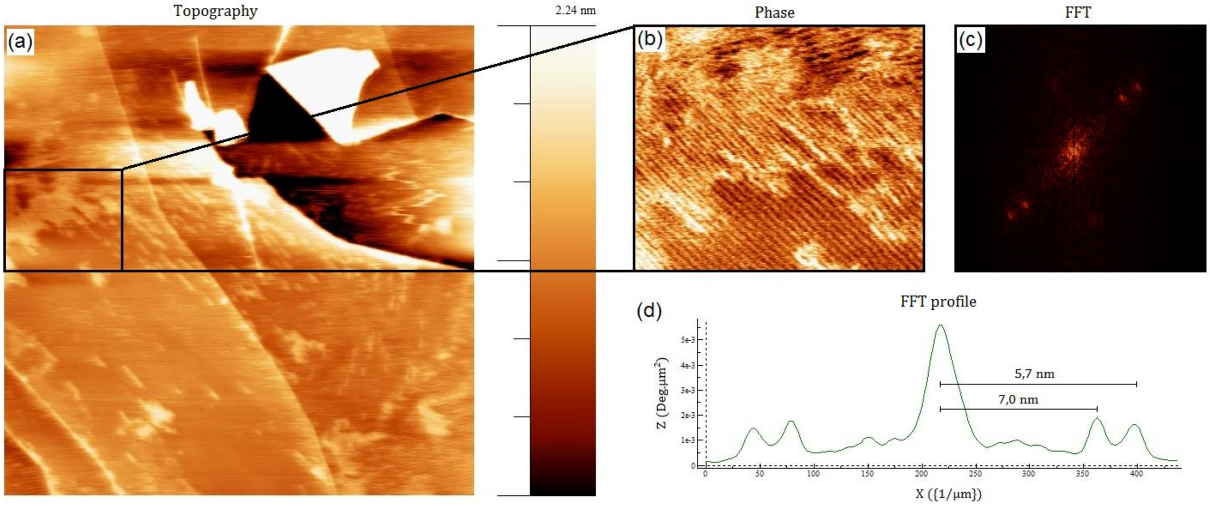

Figure 3.9. *(a) 1 x 1 µm² AFM topography image obtained by dip-coating a C_{50}-functionalized HOPG surface in a 10^{-4} M ODA in ethanol solution. (b) AFM phase image corresponding to the region in (a) marked by a black box. (c) FFT transform of (b) showing the presence of two different periodicities. (d) Cross section of the FFT in (c) indicating the presence of a periodicity corresponding to 7.0 nm and another periodicity corresponding to 5.7 nm. These periodicities are attributed to C_{50} and ODA, respectively.*

Finally, it must be noted that the maximum obtained coverage of ODA on a C_{50}-fuctionalized HOPG surface, as shown in Figure 3.8d, is relatively low. Dip-coating in more concentrated ODA in ethanol solutions was, however, not possible due to solubility issues. One way to overcome this issue is using the drop-casting technique to deposit ODA, instead the dip-coating method. Doing so, the ODA molecules are forced to self-assemble on the surface. Figure 3.10 depicts images obtained after drop-casting 4 drops of a 5 x 10^{-5} M ODA in ethanol solution on a C_{50}-functionalized HOPG surface. These images prove that in this way a higher surface coverage of ODA on C_{50} can be obtained than what was previously achieved using dip-coating. Therefore, this deposition technique will be used to assess the shielding potential of a C_{50} layer on graphene. Another advantage of drop-casting is that a specific amount of molecules are deposited on the surface, irrespective of whether that surface is bare graphene or C_{50}-functionalized graphene. This allows for comparison of doping effects. However, one must keep in mind that ODA shows a higher affinity for graphite-like surfaces than for C_{50}-functionalized surfaces, meaning that even though the same amount of molecules are deposited, they will probably be distributed less homogeneously on a C_{50}-functionalized surface (*i.e.* multi-layered clusters of ODA will preferably be formed on C_{50}-functionalized surfaces). Also, when defects are present in the C_{50} layer (*i.e.* incomplete coverage), it is expected that the ODA molecules will adsorb in these defected sites in order to avoid the C_{50} layer.

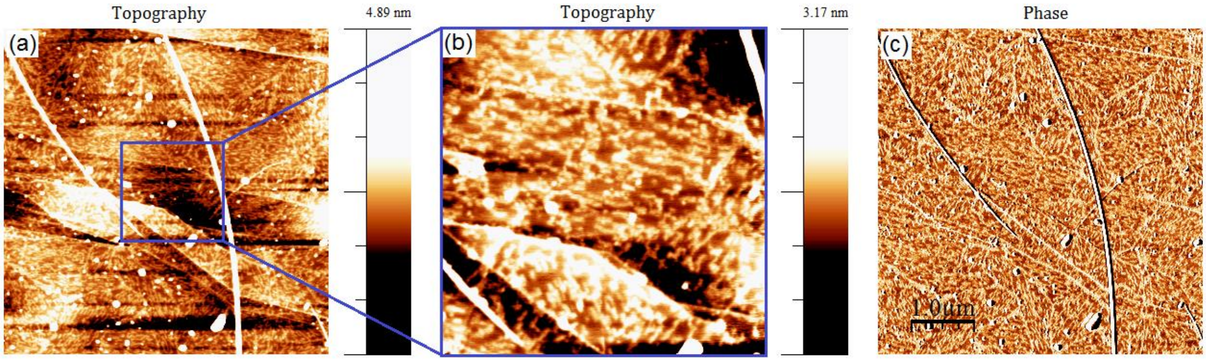

Figure 3.10. *(a) 5 x 5 µm^2 AFM topography image obtained by drop-casting 4 drops of ODA from a 5 x 10^{-5} M solution in ethanol on a C_{50}-functionalized HOPG surface. (b) 1.5 x 1.5 µm^2 zoom-in corresponding to the region in (a) marked by a blue box. (c) 5 x 5 µm^2 phase image corresponding to (a). These images show that by drop-casting ODA on a C_{50}-functionalized surface, a higher surface coverage can be achieved than when ODA is deposited with the dip-coating method.*

3.2 Surface-passivation of graphene

Now that the optimal conditions for the deposition of a high quality C_{50} layer have been established and that the self-assembly behavior of ODA on both bare HOPG and C_{50}-functionalized HOPG has been elucidated, we focus on exploiting this knowledge to investigate the potential of a C_{50} layer to shield graphene from atmospheric/deliberately added dopants.

3.2.1 Raman characterization

3.2.1.1 Atmospheric doping

In a first experiment, atmospheric doping as a function of time was studied for both bare and C_{50}-functionalized graphene flakes. Because the standard cleaning procedure resulted in strong p-doped flakes (see Appendix 1), the graphene flakes used for this experiment were subjected to a modified cleaning procedure, *i.e.* only a toluene clean was performed and no forming gas anneal. This should allow us to observe changes in p-doping level more readily. Right before the functionalization/1st measurement, the flakes were annealed under mild conditions (1 h at 150 °C under N_2 atmosphere) to remove all adsorbed water and oxygen. It must be noted that due to technical limitations the samples had been exposed to ambient conditions for ~ 10 min before the functionalization/1st measurement was performed. This is important because the atmospheric doping effect shows a logarithmic time dependence, meaning that the effect is most pronounced during the first hours, as evidenced in Figure 1.15 and Figure 1.17. In between different measurements the samples were stored in a desiccator, of which the bottom was filled with water. The temperature during storage was 22.1 ± 0.4 °C and the relative humidity was 74 ± 14 %. This artificially high humidity should accelerate/increase the atmospheric doping effect exerted on the flakes.

Figure 3.11 shows the evolution of the G peak position as a function of time for both bare and C_{50}-functionalized graphene flakes (two flakes per sample). For p-doping, one expects a gradual blueshift of the G peak position over time. However, partly due to a low precision of the measurements, no significant shift of the G peak position over time can be observed for either of the samples. P-type doping should further translate in a decrease of the FWHM of the G peak, a decrease of the intensity ratio I_{2D}/I_{G}, and a blueshift of the 2D peak position. However, as shown in Figure 3.12, Figure 3.13 and Figure 3.14, none of these trends can clearly be observed in the Raman spectra. This indicates that Raman spectroscopy is not sensitive enough for the detection of atmospheric doping or that atmospheric doping was already saturated after 10 min.

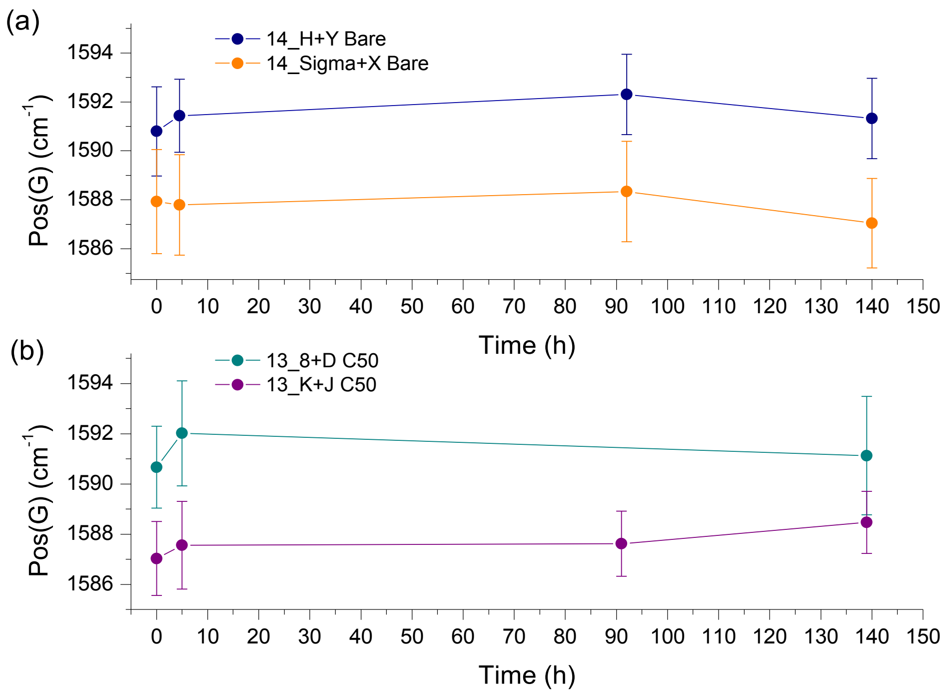

Figure 3.11. *Evolution of the G peak position as a function of time for (a) bare and (b)* C_{50}*-functionalized graphene flakes. Each of the samples contains two different flakes as indicated in the corresponding legends. Data points are averages of a Raman map on each flake.*

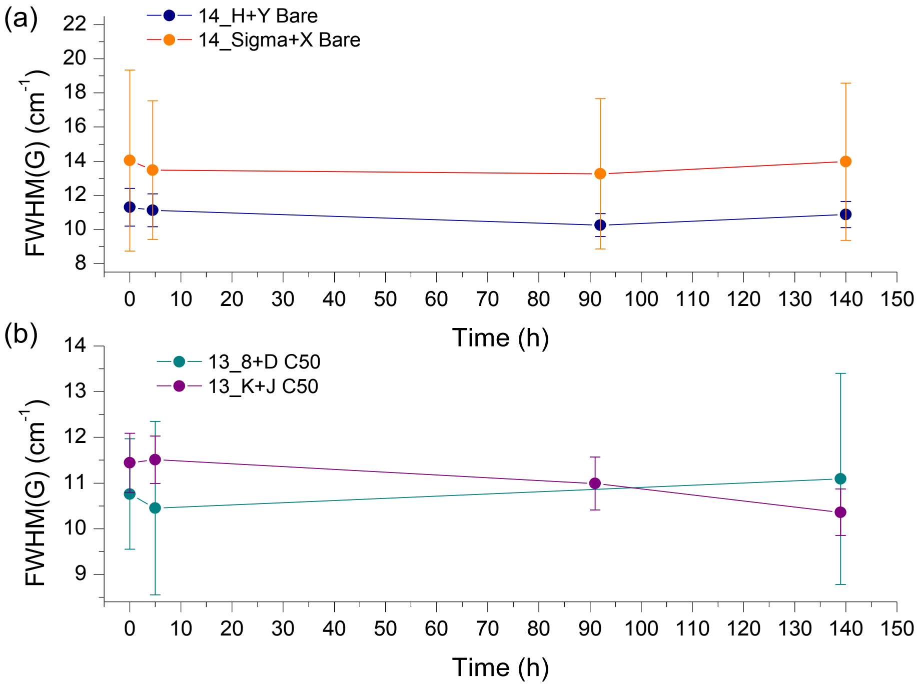

Figure 3.12. *Evolution of the FWHM of the G peak as a function of time for (a) bare and (b)* C_{50}*-functionalized graphene flakes. Each of the samples contains two different flakes as indicated in the corresponding legends. Data points are averages of a Raman map on each flake.*

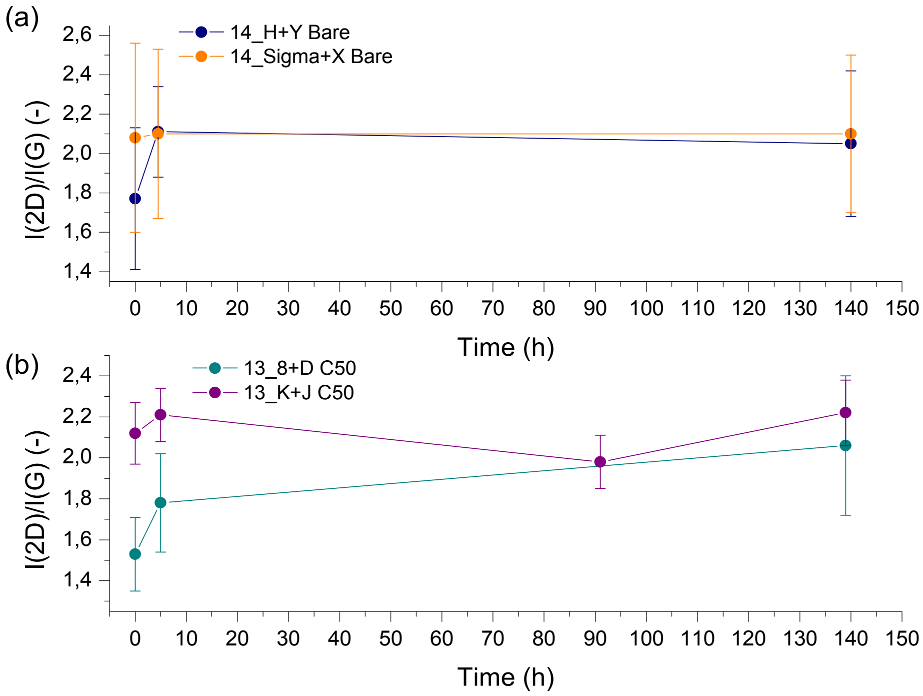

Figure 3.13. *Evolution of the intensity ratio I_{2D}/I_G as a function of time for (a) bare and (b) C_{50}-functionalized graphene flakes. Each of the samples contains two different flakes as indicated in the corresponding legends. Data points are averages of a Raman map on each flake.*

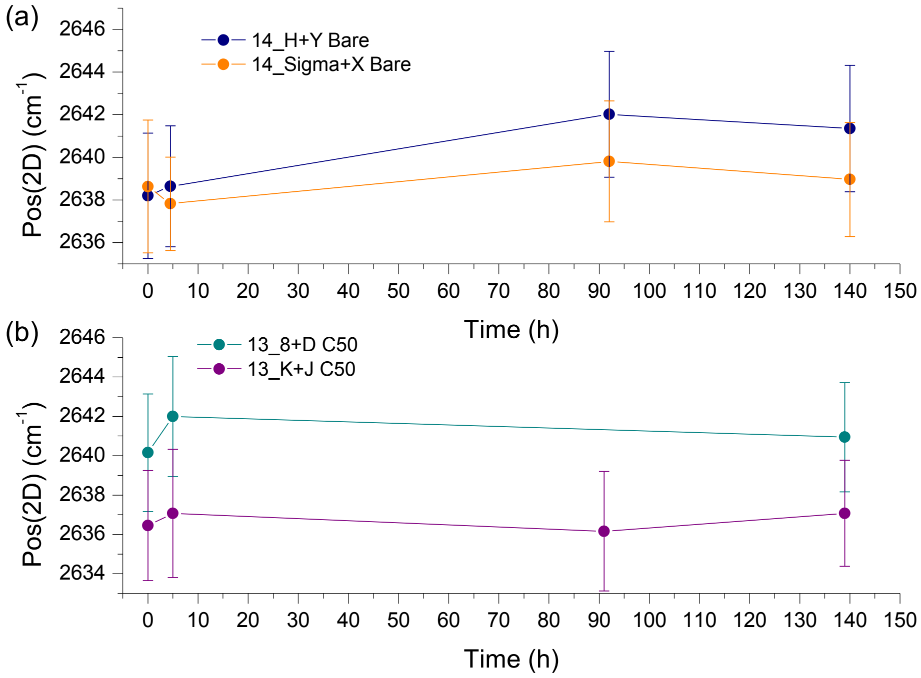

Figure 3.14. *Evolution of the 2D peak position as a function of time for (a) bare and (b) C_{50}-functionalized graphene flakes. Each of the samples contains two different flakes as indicated in the corresponding legends. Data points are averages of a Raman map on each flake.*

3.2.1.2 Doping by octadecylamine

In a second set of experiments, doping exerted by ODA on both bare and C_{50}-functionalized flakes was investigated. Because ODA is drop-casted from ethanol, the effect of ethanol on graphene flakes was evaluated prior to the actual experiment. In a previous study n-doping by ethanol was reported [32], thus in order to extract the net doping effect of ODA on the flakes, this control experiment is believed to be essential.

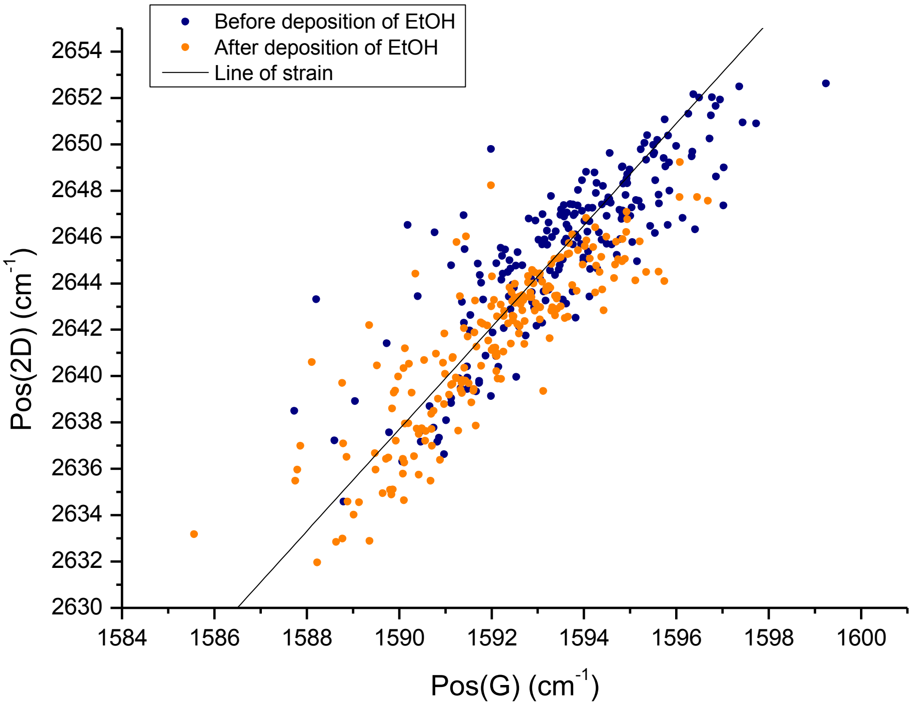

Figure 3.15. *Plot of Pos(2D) vs. Pos(G) for a total of 4 graphene flakes before and after drop-casting 4 drops of ethanol. The plot shows a redshift of the G peak and 2D peak along the line corresponding to changes in strain.*

Raman maps of 4 flakes were taken before and after addition of ethanol. Ethanol was deposited by drop-casting 4 drops and subsequently drying the sample under Ar for 5 min. The results are summarized in Table 3.1. After addition of ethanol, a redshift of the G peak and 2D peak is observed. To separate strain from doping effects, a plot of the 2D peak position *vs.* the G peak position is given in Figure 3.15. This plot shows that the observed redshift occurs along the line corresponding to variations in strain, thus indicating that the changes in the Raman spectrum after addition of ethanol are due to changes in strain rather than due to doping effects. More specifically, the changes in strain can be attributed to a release of compressive strain. It is important to note that this observation has been reproduced by a group member who dip-coated a sample containing graphene flakes in ethanol. The strain releasing effect observed after dip-coating in ethanol was larger compared to the effect observed after drop-casting. This is reasonable because with dip-coating the flakes are in contact with the solvent for a longer time.

The reason for this strain releasing effect is not really clear. The most obvious assumption is that ethanol intercalates between the graphene sheet and the Si/SiO$_2$ substrate, thereby releasing the compressive strain, which was induced during annealing of the flakes. However, as shown in Appendix 1, thermal annealing induces not only compressive strain, but also strong p-type doping, which is attributed to an increased coupling of the flakes to the substrate. Thus, if one assumes that EtOH intercalates between the graphene flake and the substrate, thereby diminishing the degree of substrate coupling, then a reduction of p-type doping is expected as well. Clearly this is not observed in Figure 3.15 and a clear interpretation of the strain releasing effect induced by ethanol is lacking.

Now that the effect of ethanol on the flakes is known, doping exerted by ODA on the flakes was investigated. Raman maps of two flakes were taken before and after addition of ODA. ODA was deposited by drop-casting 4 drops of a 5×10^{-5} M solution in ethanol. After deposition, the sample was dried under Ar for 5 min. Table 3.1 summarizes the changes that were observed in the Raman spectra. To extract the net doping effect by ODA, a correction for ethanol was carried out based on the results described earlier in this section. It must be noted that this correction must be interpreted with some precaution. It is, for instance, expected that the strain releasing effect that was observed after ethanol deposition depends on the initial strain level of the flakes. Therefore, no quantitative conclusions should be drawn from these corrected data. However, the correction for ethanol is based on data from 4 different flakes and is therefore believed to give good qualitative results. Looking at the corrected data, it is clear that a strong redshift of the G peak and 2D peak, together with a broadening of the G peak and an increase in the I_{2D}/I_G ratio is induced by ODA. These changes in the Raman spectra are in perfect agreement with a reduction of p-type doping, *i.e.* n-type doping by ODA. This is further confirmed in Figure 3.16, where a clear shift of the (corrected) data points along the line corresponding to variations in hole doping is observed (redshift, thus a reduction in p-type doping). These results confirm that amine-based molecules are n-type dopants, as was reported in earlier studies [73], [75].

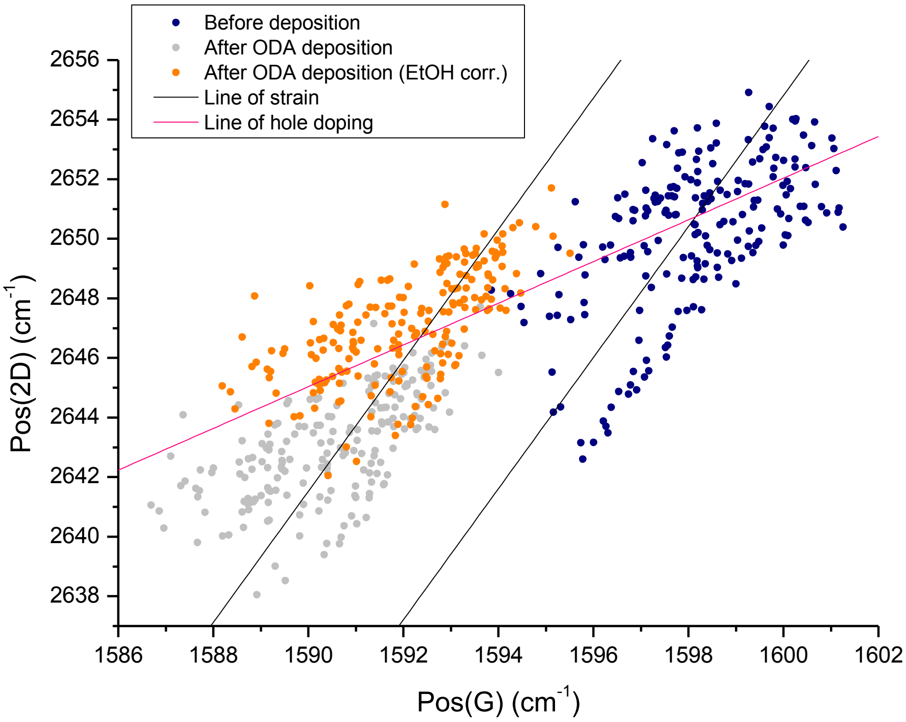

Figure 3.16. *Plot of Pos(2D) vs. Pos(G) for a total of 2 graphene flakes before and after drop-casting 4 drops of 5 x 10^{-5} M ODA in ethanol. The plot shows a redshift of the (ethanol corrected) data along the line corresponding to hole doping, i.e. a reduction in p-type doping an thus n-type doping by ODA.*

Next, the effect of toluene on graphene flakes was studied. This control experiment was done because in the following a C_{50} layer is deposited from toluene. Thus, in order to know if a C_{50} layer preserves the graphene characteristics, it is necessary to know the effect of toluene on the flakes. Raman maps were taken on one flake before and after deposition of toluene. Toluene was deposited by drop-casting 4 drops of toluene and subsequently drying the sample under Ar for 5 min. The Raman results are summarized in Table 3.1. Only minor changes in the Raman spectra are observed, except for a significant increase in the I_{2D}/I_G ratio. The increased $I_{2D/G}$ ratio possibly indicates a reduction in p-type doping, caused by a cleaning or intercalation effect of toluene. A plot of the 2D peak position *vs.* the G peak position is given in Figure 3.17, but the shifts in the Raman spectra are too small to conclude on a reduced hole concentration. Finally, it is instructive to compare these data to the data obtained after deposition of ethanol under the same conditions: while for ethanol a strain releasing effect was observed, this is not observed for toluene. In contrary, a reduction of p-doping seems more likely to be caused by toluene.

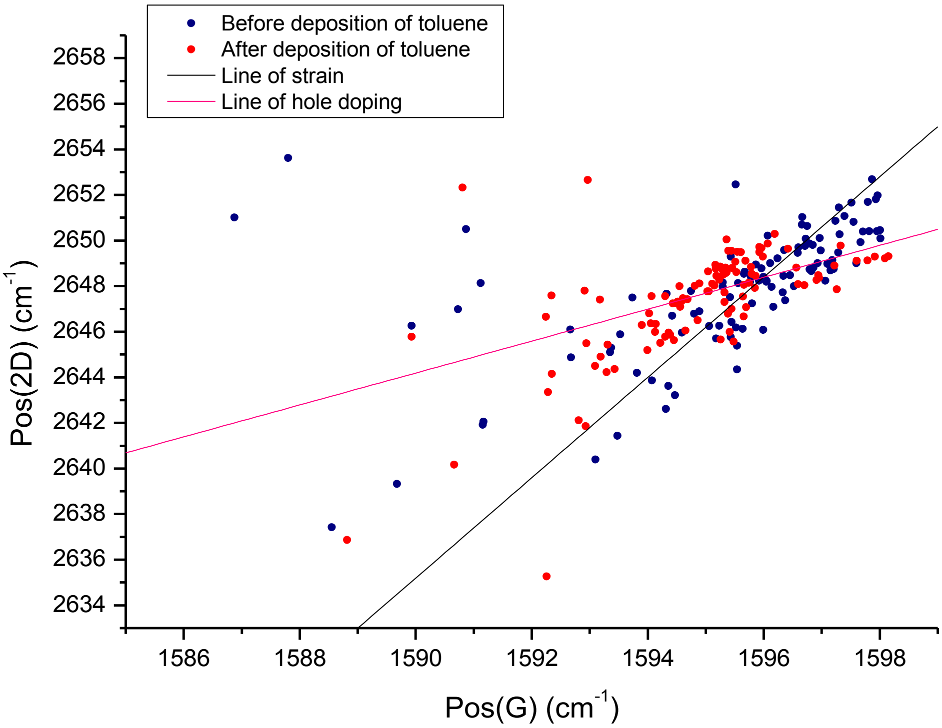

Figure 3.17. *Plot of Pos(2D) vs. Pos(G) for one graphene flake before and after drop-casting 4 drops of toluene. Only minor changes in the data are observed after deposition of toluene.*

Finally, the doping exerted by ODA on C_{50}-functionalized flakes was evaluated. Raman maps of two flakes were obtained before deposition of the C_{50} layer, after deposition of the C_{50} layer and after addition of ODA on the C_{50}-functionalized flakes. C_{50} was deposited by dip-coating the sample in a 500x dilution of a saturated toluene solution and ODA was deposited by drop-casting 4 drops of a 5 x 10^{-5} M ethanol solution. The results of the Raman measurements are summarized in Table 3.1.

Comparing the data before and after deposition of the C_{50} layer indicates a small redshift of the G peak and 2D peak, together with a strong increase of the I_{2D}/I_G ratio. These changes correspond very well to those observed in the control experiment where only toluene was deposited. Therefore, it is assumed that the changes in the Raman spectra after addition of C_{50} are caused by toluene. This is further confirmed by the plot shown in Figure 3.18. Only minor changes are observed after addition of C_{50}, comparable to those in Figure 3.17. Hence, it can be concluded that C_{50} does not cause charge transfer doping of graphene and thus preserves its pristine electronic characteristics.

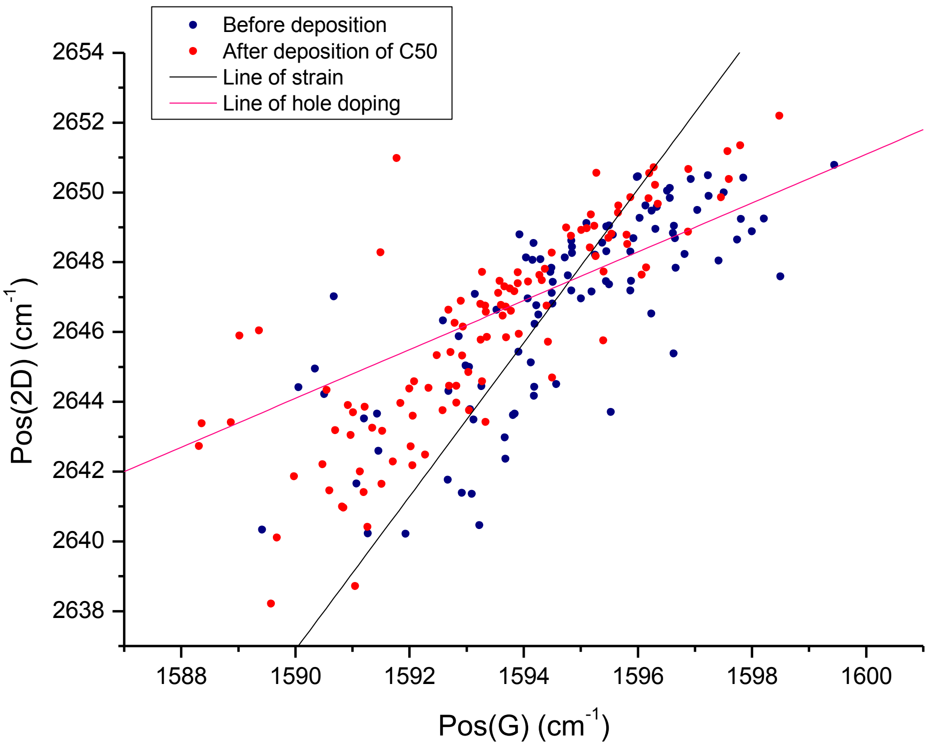

Figure 3.18. *Plot of Pos(2D) vs. Pos(G) for a total of two graphene flakes before and after deposition of a* C_{50} *layer from toluene. Only minor changes in the data are observed after deposition, comparable to the changes in Figure 3.17. Therefore, these changes are assumed to be caused by toluene and not by the* C_{50} *layer.*

Finally, the addition of ODA on C_{50}-functionalized flakes is evaluated. As shown in Table 3.1, after correcting the data for the effect imposed by ethanol, a redshift of the G and 2D peak is observed. However, this redshift is much smaller than what was observed after deposition of ODA on bare graphene flakes. Combined with the fact that the intensity ratio I_{2D}/I_G does not shift after deposition of ODA on C_{50}-functionalized flakes, it can be concluded that almost no doping by ODA occurred. This is further corroborated by the plot depicted in Figure 3.19, which demonstrates that the addition of ODA on C_{50}-functionalized flakes did not lead to major changes in the Raman data (compare with Figure 3.16). It seems though, that while most of the data remained close to the original values, some data points have spread out along the line corresponding variations in hole concentration. This could be the result of local n-doping effect by ODA where the C_{50} layer is defected and would explain the small redshift of the G and 2D peak. It should be noted that this strongly reduced doping effect by ODA on C_{50}-functionalized flakes must be interpreted in the perspective of a low affinity of ODA for C_{50}. Because the experiments on HOPG showed that the surface coverage of ODA on C_{50}-functionalized HOPG is lower than on bare HOPG, a reduced doping effect is to be expected. Furthermore, the graphene flakes are surrounded by SiO_2 and there is no information at hand concerning the affinity of ODA for SiO_2. If, for instance, ODA shows the following affinity for different substrates: graphene > SiO_2 > C_{50}, then it is to be expected that ODA avoids self-assembly on C_{50} by settling down on the SiO_2 surface. This as well could contribute to a reduced doping effect. However, the fact that doping by ODA on C_{50}-functionalized flakes is almost totally precluded, indicates that C_{50} forms a suitable surface passivation layer for graphene.

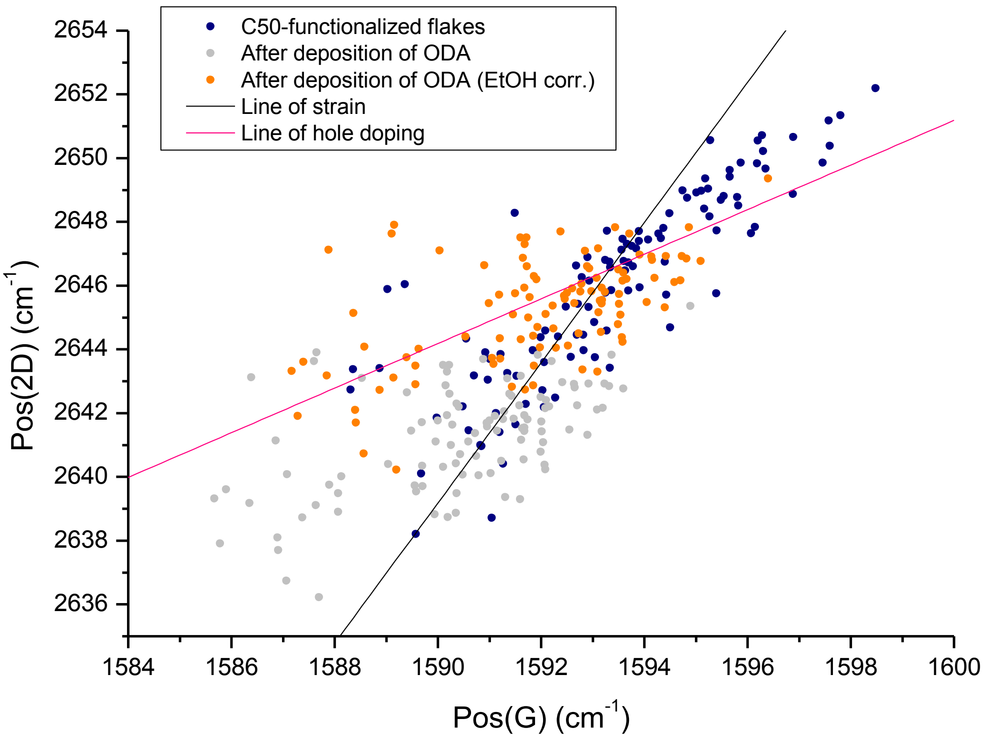

Figure 3.19. *Plot of Pos(2D) vs. Pos(G) for a total of two C_{50}-functionalized graphene flakes before and after deposition of 4 drops of ODA from a 5 x 10^{-5} M ethanol solution. While some data points have moved along the line corresponding to hole doping, most of the data points remained close to the original values. Comparing these data to those in Figure 3.16 indicates that the n-doping effect by ODA is strongly reduced upon passivation of the graphene flakes with a C_{50} layer.*

Despite the good coherence of the Raman data presented above, they should be interpreted with some precaution. The main issue is the fact that there is a rather large initial flake-to-flake variation before deposition. It is very likely that this influences the effects that are observed, although it is not known to what extent this influence takes place. Furthermore, as discussed in Appendix 1, even for a single flake there is a certain degree of inhomogeneity, *i.e.* edge versus center of the flake. Therefore, it is expected that also the size and shape of the flakes will influence the effects that are observed. Hence, statistical analysis of a large number of flakes is needed to confirm the validity of the Raman results that have been discussed in this section.

In order to support the Raman data presented above, all of the samples have been characterized by AFM. However, it proved to be very challenging to image self-assembly on graphene flakes. This is presumably due to an increased roughness of the flakes compared to HOPG and/or due to contamination on the flakes. Only for the sample where ODA was deposited on C_{50}-functionalized flakes, AFM images were obtained that show the presence of lamellae, as shown in Figure 3.20. The FFT is not very sharp and yields a lamellar width between ~ 5 and ~ 6 nm. From these data it is not possible to attribute the lamellae to either C_{50} or ODA. Based on the AFM experiments on HOPG, it is more likely that lamellae of C_{50} have been imaged, what would prove that also on graphene flakes a self-assembled C_{50} layer can be formed.

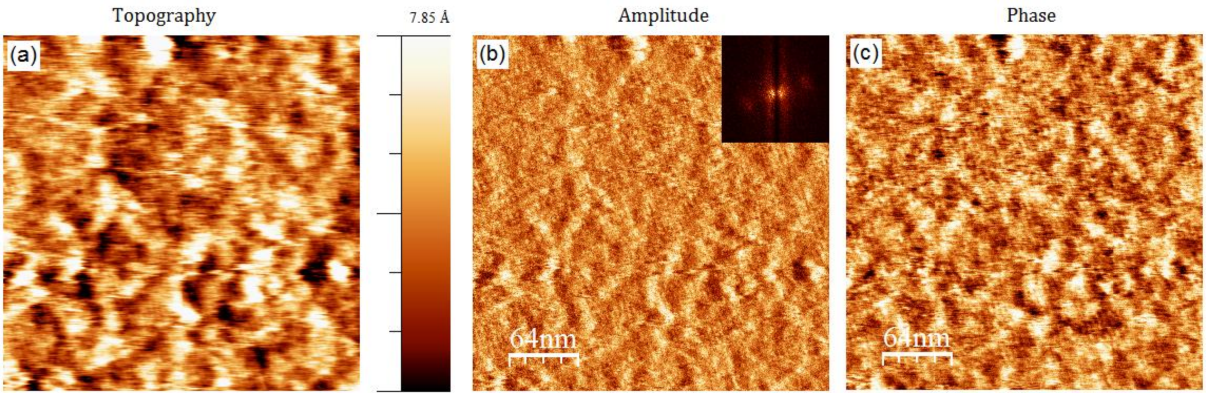

Figure 3.20. *320 x 320 nm^2 AFM images of ODA on C_{50}-functionalized flakes: (a) topography image, (b) amplitude image (FFT in inset), and (c) phase image. The FFT yields a lamellar width between ~ 5 and ~ 6 nm.*

Table 3.1. *Overview of the Raman data. All data correspond to mean values obtained from Raman maps on one or more flakes.*

Overview Raman data		**Pos(G) (cm^{-1})**	**FWHM(G) (cm^{-1})**	**Pos(2D) (cm^{-1})**	**FWHM(2D) (cm^{-1})**	**I(2D)/I(G) (-)**
Deposition of EtOH	*Before EtOH*	1593.6 ± 1.9	10.6 ± 1.5	2645.5 ± 3.6	30.2 ± 1.9	1.5 ± 0.1
	After EtOH	1592.1 ± 1.9	10.6 ± 1.3	2641.5 ± 3.5	30.9 ± 1.7	1.4 ± 0.1
Deposition of ODA	*Before ODA*	1598.1 ± 1.6	10.5 ± 1.1	2650.1 ± 2.5	31.0 ± 1.3	1.5 ± 0.2
	After ODA	1590.5 ± 1.5	12.7 ± 1.5	2643.0 ± 1.8	32.4 ± 1.5	1.8 ± 0.3
	After ODA (EtOH corr.)	1592.0 ± 3.1	12.7 ± 2.5	2647.0 ± 5.3	31.7 ± 2.9	1.9 ± 0.3
Deposition of toluene	*Before toluene*	1595.4 ± 2.2	10.4 ± 2.7	2647.9 ± 2.8	30.2 ± 1.6	1.4 ± 0.1
	After toluene	1594.8 ± 1.7	10.1 ± 1.3	2647.4 ± 2.6	30.0 ± 2.6	1.9 ± 0.2
Deposition of C_{50} and ODA	*Before*	1594.7 ± 2.0	11.2 ± 1.4	2646.8 ± 2.7	31.1 ± 1.6	1.4 ± 0.1
	After C_{50}	1593.4 ± 2.2	11.7 ± 1.4	2646.1 ± 3.0	31.2 ± 1.6	1.7 ± 0.2
	After C_{50} + ODA	1590.5 ± 2.0	11.8 ± 2.2	2641.3 ± 1.7	31.8 ± 2.9	1.6 ± 0.2
	After C_{50} + ODA (EtOH corr.)	1592.0 ± 3.4	11.8 ± 3.0	2645.3 ± 5.3	31.1 ± 3.8	1.7 ± 0.2

3.2.2 Electrical characterization

Electrical measurements on graphene field effect devices were performed in order to corroborate the Raman data. 4 devices were produced. Unfortunately, only one device worked properly. The main issue was that the devices were heavily p-doped by the lengthy forming gas anneal, such that very high back-gate voltages (> 60 V) were needed to measure the charge neutrality point (CNP). At these high voltages, the oxide breaks down because a local conductive path in the oxide is formed. However, the forming gas treatment is necessary to remove photoresist residues on the graphene surface, thus a compromise must be made between cleanliness and hole doping level. Therefore, an alternative device production process is highly desired.

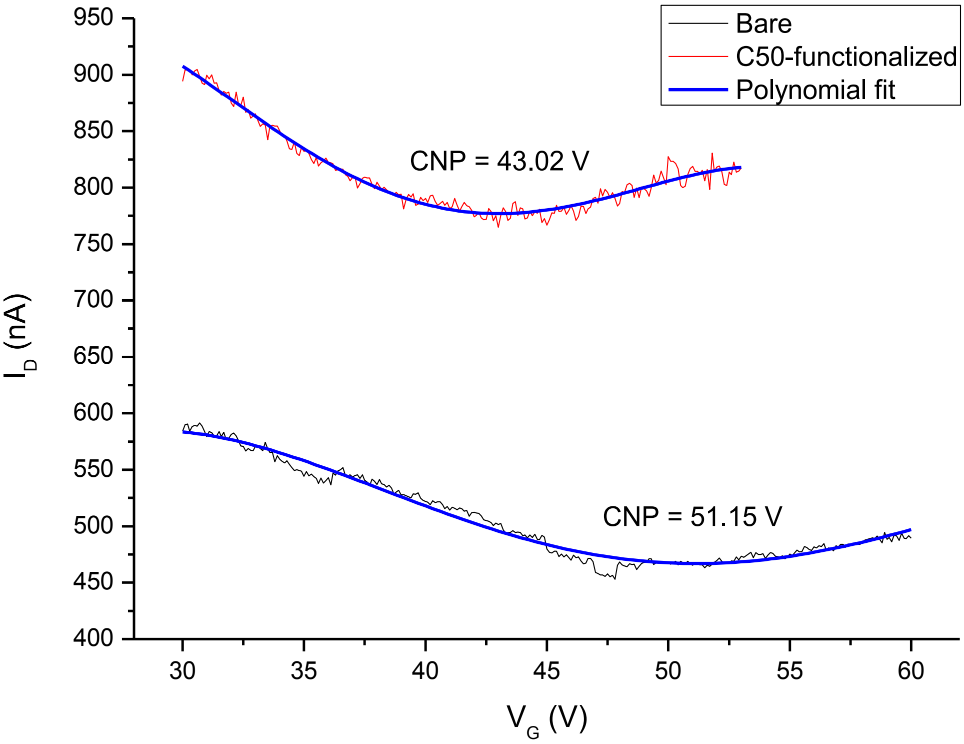

Figure 3.21. *Transfer characteristics for a graphene field effect device before and after deposition of a C_{50} layer. After deposition, the transfer curve shifted by -8.13 V and the hole mobility increased by a factor 1.84. These changes indicate a cleaning effect caused by toluene.*

The single working device was used to assess the effect of depositing a C_{50} layer, which was deposited by dip-coating the device in a 500x dilution of a saturated toluene solution. The transfer curves that were obtained before and after functionalization are given in Figure 3.21. In fact, in order to reduce the noise, the transfer curves shown in Figure 3.21 correspond to an average of 5 transfer curves that were obtained subsequently. The CNP was extracted by fitting a 4th order polynomial to the transfer curves. Comparison of the two curves shows that after deposition, the CNP has shifted by -8.13 V, what corresponds to a reduction of the hole concentration from 1.22 x 10^{13} cm^{-2} to 1.03 x 10^{13} cm^{-2}. This reduction in hole concentration is most likely caused by a cleaning or intercalation effect by toluene. The hypothesis that toluene causes cleaning or intercalation is further confirmed by the fact that the hole mobility increased by a factor 1.84 after deposition of the C_{50} layer. Hence, it is assumed that toluene removes some of the resist residues or reduces the degree of substrate coupling, thereby reducing the doping level and reducing Coulomb scattering at charged impurities. However, a control experiment using only toluene is needed to confirm this.

AFM images were obtained to check the formation of a C_{50} layer on the graphene channel. The results are shown in Figure 3.22, and as can be seen no C_{50} lamellae are observed. What is observed though are photoresist residues all over the surface. It is very likely that these residues hinder the formation of a continuous C_{50} layer. Hence, despite the lengthy forming gas anneal, the devices are not clean enough to be used in self-assembly experiments.

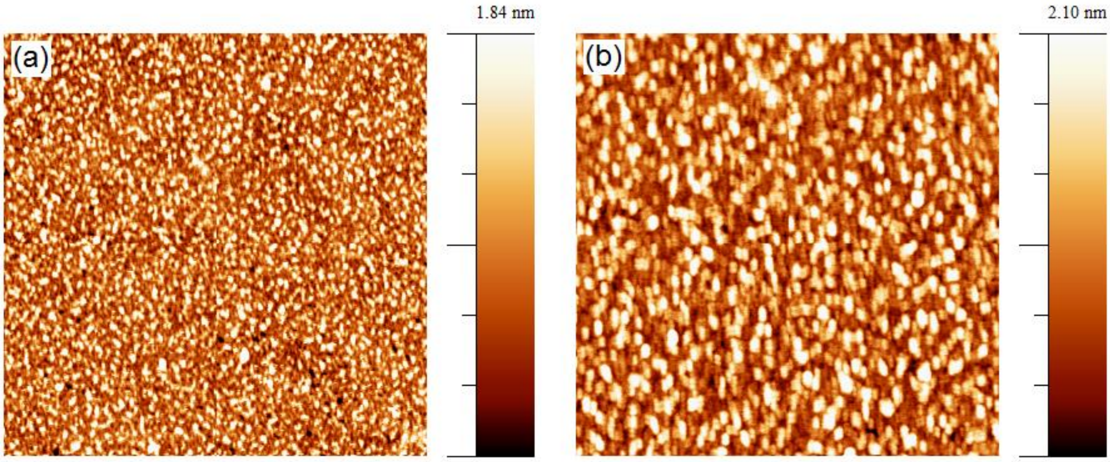

Figure 3.22. *AFM topography images of a graphene field effect device after functionalization with* C_{50}*: (a) 2 x 2* μm^2*; (b) 1 x 1* μm^2*.* C_{50} *was dip-coated from a 500x dilution of a saturated toluene solution. The device is contaminated by photoresist residues and no* C_{50} *lamellae can be observed.*

Chapter 4: Conclusion and future work

The main goal of this thesis was to prove the feasibility of using a C_{50} layer as a surface passivation layer for graphene against atmospheric dopants. This required the deposition of a high quality C_{50} monolayer on graphene. Optimization of the C_{50} layer was investigated on HOPG. In order to evaluate the robustness of the C_{50} passivation layer against other sorts of dopants, ODA was deposited on both bare and C_{50}-functionalized flakes and the doping was compared. Again, control experiments on HOPG were performed to compare the self-assembly behavior of ODA on C_{50}-functionalized HOPG to the self-assembly on bare HOPG.

With the aid of SPM, it was demonstrated that a homogeneous C_{50} layer, comprising ultra-large domains can be formed on HOPG. The formation of such ultra-large domains was shown to be favored by using dip-coating at low concentrations. This C_{50} layer was subsequently shown to affect the self-assembly behavior of ODA: on bare HOPG, ODA readily forms lamellar structures covering the whole surface, while on C_{50}, ODA prefers to form multi-layered clusters rather than a monolayer. This was attributed to a higher affinity of ODA for graphite-like surfaces than for C_{50}.

The shielding potential of a C_{50} layer against atmospheric dopants/ODA was investigated using Raman spectroscopy. Unfortunately, atmospheric doping could not be detected due to technical limitations, or because Raman spectroscopy is not sensitive enough for its detection. In the case of ODA, on the other hand, almost no doping was observed for C_{50}-functionalized flakes while a strong n-doping effect was observed for bare flakes. This indicates that a C_{50} layer can form a suitable surface passivation layer for graphene. Moreover, the Raman data showed that C_{50} does not cause doping of graphene, thereby preserving its pristine electronic characteristics.

Graphene field effect devices were produced in order to support the Raman data. Unfortunately, a tradeoff between device cleanliness and hole doping level hindered the production of functional devices. A single working device was functionalized with C_{50} and showed a decreased p-doping level, what was attributed to a cleaning or intercalation effect by toluene.

Thus, in conclusion, the results in this thesis indicate that a homogeneous C_{50} film shows great potential to be used as a surface passivation layer for graphene, protecting it from surface charge transfer doping and preserving its pristine electronic properties. However, more experiments are needed to confirm the results that were obtained in this work.

Future work involves reproducing the Raman data and corroborating these Raman data with electrical measurements on field effect devices. First of all, a statistical analysis of Raman measurements on a large number of graphene flakes is highly desired due to flake-to-flake variations. Next, in order to improve the electrical characterization, the production of field effect devices needs to be optimized. More specifically, a process is needed that produces clean devices, without having to perform a lengthy forming gas anneal treatment. A possible approach would be to use stencil lithography instead of photolithography or EBL. This technique does not involve the use of a resist, thus no cleaning of resist residues is needed [102], [103]. However, it must be noted that the production of graphene flakes, as performed in this work, also required a forming gas anneal and therefore, it would be useful to look at other cleaning procedures for the flakes as well. Finally, AFM and ultimately STM images of self-assembly on graphene flakes are desired in order to support the Raman and electrical measurements. Only when all of these requirements are fulfilled, it will be possible to univocally conclude on the feasibility of using a C_{50} layer as a surface passivation layer for graphene.

Bibliography

[1] J. E. Lilienfeld, “Method and apparatus for controlling electric currents,” 28-Jan-1930.

[2] G. E. Moore, “Cramming more components onto integrated circuits,” *Electronics*, vol. 38, no. 8, 1965.

[3] P. Wallace, “The band theory of graphite,” *Phys. Rev.*, vol. 71, no. 9, pp. 622–634, May 1947.

[4] R. Peierls, “Quelques propriétés typiques des corps solides,” *Ann. l’institut Henri Poincaré*, vol. 5, no. 3, pp. 177–222, 1935.

[5] L. Landau, “Zur Theorie der phasenumwandlungen II,” *Phys. Z. Sowjetunion*, vol. 11, pp. 26 – 35, 1937.

[6] K. S. Novoselov, A. K. Geim, S. V Morozov, and D. Jiang, “Electric field effect in atomically thin carbon films,” *Science*, vol. 306, no. 5696, pp. 666–669, 2004.

[7] “The Nobel Prize in Physics 2010.” [Online]. Available: http://www.nobelprize.org/nobel_prizes/physics/laureates/2010/. [Accessed: 16-May-2015].

[8] A. K. Geim and K. S. Novoselov, “The rise of graphene,” *Nat. Mater.*, vol. 6, no. 3, pp. 183–191, 2007.

[9] U. K. Sur, “Graphene: a rising star on the horizon of materials science,” *Int. J. Electrochem.*, vol. 2012, 2012.

[10] K. S. Novoselov, V. I. Fal’ko, L. Colombo, P. R. Gellert, M. G. Schwab, and K. Kim, “A roadmap for graphene,” *Nature*, vol. 490, no. 7419, pp. 192–200, 2012.

[11] J. C. Meyer, A. K. Geim, M. I. Katsnelson, K. S. Novoselov, T. J. Booth, and S. Roth, “The structure of suspended graphene sheets,” *Nature*, vol. 446, no. 7131, pp. 60–63, 2007.

[12] J. H. Warner, F. Schaffel, M. Rummeli, and A. Bachmatiuk, *Graphene: fundamentals and emergent applications*. 2012.

[13] S. Reich, J. Maultzsch, C. Thomsen, and P. Ordejón, “Tight-binding description of graphene,” *Phys. Rev. B*, vol. 66, no. 3, 2002.

[14] L. Wang, I. Meric, P. Y. Huang, Q. Gao, Y. Gao, H. Tran, T. Taniguchi, K. Watanabe, L. M. Campos, D. A. Muller, J. Guo, P. Kim, J. Hone, K. L. Shepard, and C. R. Dean, “One-dimensional electrical contact to a two-dimensional material,” *Science*, vol. 342, no. 6158, pp. 614–617, 2013.

[15] Y. Zhang, Y.-W. Tan, H. L. Stormer, and P. Kim, “Experimental observation of the quantum Hall effect and Berry’s phase in graphene,” *Nature*, vol. 438, no. 7065, pp. 201–204, 2005.

[16] C. Berger, Z. Song, X. Li, X. Wu, N. Brown, C. Naud, D. Mayou, T. Li, J. Hass, A. N. Marchenkov, E. H. Conrad, P. N. First, and W. A. de Heer, “Electronic confinement and coherence in patterned epitaxial graphene,” *Science*, vol. 312, no. 5777, pp. 1191–1196, 2006.

[17] C. R. Dean, a F. Young, I. Meric, C. Lee, L. Wang, S. Sorgenfrei, K. Watanabe, T. Taniguchi, P. Kim, K. L. Shepard, and J. Hone, “Boron nitride substrates for high-quality graphene electronics,” *Nat. Nanotechnol.*, vol. 5, no. 10, pp. 722–726, 2010.

[18] X. Du, I. Skachko, A. Barker, and E. Y. Andrei, “Approaching ballistic transport in suspended graphene,” *Nat. Nanotechnol.*, vol. 3, no. 8, pp. 491–495, 2008.

[19] E. Hwang, S. Adam, and S. Sarma, “Carrier transport in two-dimensional graphene layers,” *Phys. Rev. Lett.*, vol. 98, no. 18, 2007.

[20] J.-H. Chen, C. Jang, S. Xiao, M. Ishigami, and M. S. Fuhrer, “Intrinsic and extrinsic performance limits of graphene devices on SiO2,” *Nat. Nanotechnol.*, vol. 3, no. 4, pp. 206–209, 2008.

[21] S. Morozov, K. Novoselov, M. Katsnelson, F. Schedin, D. Elias, J. Jaszczak, and A. Geim, “Giant intrinsic carrier mobilities in graphene and its bilayer,” *Phys. Rev. Lett.*, vol. 100, no. 1, 2008.

[22] K. S. Novoselov, A. K. Geim, S. V Morozov, D. Jiang, M. I. Katsnelson, I. V Grigorieva, S. V Dubonos, and A. A. Firsov, “Two-dimensional gas of massless Dirac fermions in graphene,” *Nature*, vol. 438, no. 7065, pp. 197–200, 2005.

[23] Y. Tan, Y. Zhang, K. Bolotin, Y. Zhao, S. Adam, E. H. Hwang, S. Das Sarma, H. L. Stormer, and P. Kim, “Measurement of scattering rate and minimum conductivity in graphene,” *Phys. Rev. B*, vol. 99, no. 24, pp. 10–13, 2007.

[24] B. Partoens and F. M. Peeters, “From graphene to graphite: Electronic structure around the K point,” *Phys. Rev. B*, vol. 74, no. 7, 2006.

[25] D. C. Elias, R. R. Nair, T. M. G. Mohiuddin, S. V Mozorov, P. Blake, and K. S. Novoselov, “Control of graphene’s properties by reversible hydrogenation: evidence for graphane,” *Science*, vol. 323, no. 5914, pp. 610–613, 2009.

[26] C. Lee, X. Wei, J. W. Kysar, and J. Hone, “Measurement of the elastic properties and intrinsic strength of monolayer graphene,” *Science*, vol. 321, no. 5887, pp. 385–388, 2008.

[27] S. Weng, W. Lin, W. Su, E. Hwu, P. Chen, T. Tsai, and C. Chang, “Estimating Young’s modulus of graphene with Raman scattering enhanced by micrometer tip,” *Nanotechnology*, vol. 25, no. 25, 2014.

[28] A. A. Balandin, “Thermal properties of graphene and nanostructured carbon materials,” *Nat. Mater.*, vol. 10, no. 8, pp. 569–581, 2011.

[29] F. Bonaccorso, Z. Sun, T. Hasan, and A. C. Ferrari, “Graphene photonics and optoelectronics,” *Nat. Photonics*, vol. 4, no. 9, pp. 611–622, 2010.

[30] P. Li, C. Chen, J. Zhang, S. Li, B. Sun, and Q. Bao, “Graphene-based transparent electrodes for hybrid solar cells,” *Front. Mater.*, vol. 1, no. 26, pp. 1–7, 2014.

[31] J. Wu, M. Agrawal, H. A. Becerril, Z. Bao, Z. Liu, Y. Chen, and P. Peumans, “Organic light-emitting diodes on solution-processed graphene transparant electrodes,” *ACS Nano*, vol. 4, no. 1, pp. 43–48, 2010.

[32] F. Schedin, A. K. Geim, S. V Morozov, E. W. Hill, P. Blake, M. I. Katsnelson, and K. S. Novoselov, “Detection of individual gas molecules adsorbed on graphene,” *Nat. Mater.*, vol. 6, no. 9, pp. 652–655, 2007.

[33] F. Schwierz, “Graphene transistors,” *Nat. Nanotechnol.*, vol. 5, no. 7, pp. 487–496, 2010.

[34] T. Ytterdal, Y. Cheng, and T. A. Fjeldly, *Device modeling for analog and RF CMOS circuit design*. 2003.

[35] F. Schwierz, “Graphene transistors : status , prospects , and problems,” *Proc. IEEE*, vol. 101, no. 7, pp. 1567–1584, 2013.

[36] D. Reddy, L. F. Register, G. D. Carpenter, and S. K. Banerjee, “Graphene field-effect transistors,” *J. Phys. D. Appl. Phys.*, vol. 45, no. 1, 2011.

[37] M. C. Lemme, T. J. Echtermeyer, M. Baus, and H. Kurz, “A graphene field-effect device,” *IEEE Electron Device Lett.*, vol. 28, no. 4, pp. 282–284, 2007.

[38] L. Liao, J. Bai, Y. Qu, Y. Lin, Y. Li, Y. Huang, and X. Duan, “High-kappa oxide nanoribbons as gate dielectrics for high mobility top-gated graphene transistors,” *Proc. Natl. Acad. Sci. U. S. A.*, vol. 107, no. 15, pp. 6711–6715, 2010.

[39] L. Yang, C. Park, Y. Son, M. Cohen, and S. Louie, “Quasiparticle energies and band gaps in graphene nanoribbons,” *Phys. Rev. Lett.*, vol. 99, no. 18, 2007.

[40] X. Li, X. Wang, L. Zhang, S. Lee, and H. Dai, “Chemically derived, ultrasmooth graphene nanoribbon semiconductors,” *Science*, vol. 319, no. 5867, pp. 1229–1232, 2008.

[41] M. C. Lemme, “Current status of graphene transistors,” *Solid State Phenom.*, vol. 156–8, pp. 499–509, 2010.

[42] L. Liao, J. Bai, R. Cheng, Y. Lin, S. Jiang, Y. Qu, Y. Huang, and X. Duan, “Sub-100 nm channel length graphene transistors,” *Nano Lett.*, vol. 10, no. 10, pp. 3952–3956, 2010.

[43] D. Jiang and Z. Chen, *Graphene chemistry: theoretical perspectives*, 1st ed. John Wiley & Sons, Ltd, 2013.

[44] L. Zhao, R. He, K. T. Rim, T. Schiros, K. S. Kim, H. Zhou, C. Gutiérrez, S. P. Chockalingam, C. J. Arguello, L. Pavlova, D. Nordlund, M. S. Hybertsen, D. R. Reichman, T. F. Heinz, P. Kim, A. Pinczuk, G. W. Flynn, and A. N. Pasupathy, “Visualizing individual nitrogen dopants in monolayer graphene,” *Science*, vol. 333, no. 6045, pp. 999–1003, 2011.

[45] O. Leenaerts, B. Partoens, and F. Peeters, “Adsorption of H2O, NH3, CO, NO2, and NO on graphene: a first-principles study,” *Phys. Rev. B*, vol. 77, no. 12, 2008.

[46] K. S. Mali, J. Greenwood, J. Adisoejoso, R. Phillipson, and S. De Feyter, “Nanostructuring graphene for controlled and reproducible functionalization,” *Nanoscale*, vol. 7, no. 5, pp. 1566–1585, 2015.

[47] T. O. Wehling, K. S. Novoselov, S. V Morozov, E. E. Vdovin, M. I. Katsnelson, A. K. Geim, and A. I. Lichtenstein, “Molecular doping of graphene,” *Nano Lett.*, vol. 8, no. 1, pp. 173–177, 2008.

[48] V. Chakrapani, J. C. Angus, A. B. Anderson, S. D. Wolter, B. R. Stoner, and G. U. Sumanasekera, “Charge transfer equilibria between diamond and an aqueous oxygen electrochemical redox couple,” *Science*, vol. 318, no. 5855, pp. 1424–1430, 2007.

[49] P. L. Levesque, S. S. Sabri, C. M. Aguirre, J. Guillemette, M. Siaj, P. Desjardins, T. Szkopek, and R. Martel, “Probing charge transfer at surfaces using graphene transistors,” *Nano Lett.*, vol. 11, no. 1, pp. 132–137, 2011.

[50] Z. Li, Y. Wang, A. Kozbial, G. Shenoy, F. Zhou, R. Mcginley, P. Ireland, B. Morganstein, A. Kunkel, S. P. Surwade, L. Li, and H. Liu, “Effect of airborne contaminants on the wettability of supported graphene and graphite,” *Nat. Mater.*, vol. 12, no. 10, pp. 925–931, 2013.

[51] C. M. Aguirre, P. L. Levesque, M. Paillet, F. Lapointe, B. C. St-Antoine, P. Desjardins, and R. Martel, “The role of the oxygen/water redox couple in suppressing electron conduction in field-effect transistors,” *Adv. Mater.*, vol. 21, no. 30, pp. 3087–3091, 2009.

[52] W. Kim, A. Javey, O. Vermesh, Q. Wang, Y. Li, H. Dai, and S. U. V, “Hysteresis caused by water molecules in carbon nanotube field-effect transistors,” *Nano Lett.*, vol. 3, no. 2, pp. 193–198, 2003.

[53] M. Lafkioti, B. Krauss, T. Lohmann, U. Zschieschang, H. Klauk, K. Klitzing, and J. H. Smet, “Graphene on a hydrophobic substrate : doping reduction and

hysteresis suppression under ambient conditions," *Nano Lett.*, vol. 10, no. 4, pp. 1149–1153, 2010.

[54] C. Riedl, C. Coletti, and U. Starke, "Structural and electronic properties of epitaxial graphene on SiC(0 0 0 1): a review of growth, characterization, transfer doping and hydrogen intercalation," *J. Phys. D. Appl. Phys.*, vol. 43, no. 37, 2010.

[55] H. E. Romero, N. Shen, P. Joshi, H. R. Gutierrez, S. A. Tadigadapa, J. O. Sofo, and P. C. Eklund, "n-Type behavior of graphene supported on Si/SiO2 substrates," *ACS Nano*, vol. 2, no. 10, pp. 2037–2044, 2008.

[56] R. H. Miwa, T. M. Schmidt, W. L. Scopel, and a. Fazzio, "Doping of graphene adsorbed on the a-SiO2 surface," *Appl. Phys. Lett.*, vol. 99, no. 16, pp. 13–16, 2011.

[57] R. A. Nistor, M. A. Kuroda, A. A. Maarouf, and G. J. Martyna, "Doping of adsorbed graphene from defects and impurities in SiO2 substrates," *Phys. Rev. B*, vol. 86, no. 4, pp. 1–5, 2012.

[58] M. Ishigami, J. H. Chen, W. G. Cullen, M. S. Fuhrer, and E. D. Williams, "Atomic structure of graphene on SiO2," *Nano Lett.*, vol. 7, no. 6, pp. 1643–1648, 2007.

[59] S. Ryu, L. Liu, S. Berciaud, Y. Yu, H. Liu, P. Kim, W. George, and L. E. Brus, "Atmospheric oxygen binding and hole doping in deformed graphene on a SiO2 substrate," *Nano Lett.*, vol. 10, no. 12, pp. 4944–4951, 2010.

[60] A. Pirkle, J. Chan, A. Venugopal, D. Hinojos, C. W. Magnuson, S. McDonnell, L. Colombo, E. M. Vogel, R. S. Ruoff, and R. M. Wallace, "The effect of chemical residues on the physical and electrical properties of chemical vapor deposited graphene transferred to SiO2," *Appl. Phys. Lett.*, vol. 99, no. 12, pp. 28–31, 2011.

[61] Y. Dan, Y. Lu, N. J. Kybert, Z. Luo, and A. T. C. Johnson, "Intrinsic response of graphene vapor sensors," *Nano Lett.*, vol. 9, no. 4, pp. 1472–1475, 2009.

[62] Z. Cheng, Q. Zhou, C. Wang, Q. Li, C. Wang, and Y. Fang, "Toward intrinsic graphene surfaces: a systematic study on thermal annealing and wet-chemical treatment of SiO2-supported graphene devices," *Nano Lett.*, vol. 11, no. 2, pp. 767–771, 2011.

[63] J. Moser, A. Barreiro, and A. Bachtold, "Current-induced cleaning of graphene," *Appl. Phys. Lett.*, vol. 91, no. 16, 2007.

[64] Y. D. Lim, D. Y. Lee, T. Z. Shen, C. H. Ra, J. Y. Choi, and W. J. Yoo, "Si-compatible cleaning process for graphene using low-density inductively coupled plasma," *ACS Nano*, vol. 6, no. 5, pp. 4410–4417, 2012.

[65] C. Mattevi, F. Colléaux, H. Kim, Y.-H. Lin, K. T. Park, M. Chhowalla, and T. D. Anthopoulos, “Solution-processable organic dielectrics for graphene electronics,” *Nanotechnology*, vol. 23, no. 34, 2012.

[66] Z. Liu, A. A. Bol, and W. Haensch, “Large-scale graphene transistors with enhanced performance and reliability based on interface engineering by phenylsilane self-assembled monolayers,” *Nano Lett.*, vol. 11, no. 2, pp. 523–528, 2011.

[67] D. Shin, H. M. Lee, S. M. Yu, K. Lim, J. H. Jung, M. Kim, S. Kim, J. Han, R. S. Ruoff, and J. Yoo, “A facile route to recover intrinsic graphene over large scale,” *ACS Nano*, vol. 6, no. 9, pp. 7781–7788, 2012.

[68] C. G. Kang, Y. G. Lee, S. K. Lee, E. Park, C. Cho, S. K. Lim, H. J. Hwang, and B. H. Lee, “Mechanism of the effects of low temperature Al2O3 passivation on graphene field effect transistors,” *Carbon*, vol. 53, pp. 182–187, 2013.

[69] A. A. Sagade, D. Neumaier, D. Schall, M. Otto, A. Pesquera, A. Centeno, A. Z. Elorza, and H. Kurz, “Highly air stable passivation of graphene based field effect devices,” *Nanoscale*, vol. 7, no. 8, pp. 3558–3564, 2015.

[70] J. Lee, L. Tao, K. N. Parrish, Y. Hao, R. S. Ruoff, and D. Akinwande, “Multi-finger flexible graphene field effect transistors with high bendability,” *Appl. Phys. Lett.*, vol. 101, no. 25, 2012.

[71] L. Wang, Z. Chen, C. R. Dean, T. Taniguchi, K. Watanabe, L. E. Brus, and J. Hone, “Negligible environmental sensitivity of graphene in a hexagonal boron nitride/graphene/h-BN sandwich structure,” *ACS Nano*, vol. 6, no. 10, pp. 9314–9319, 2012.

[72] H. G. Jee, J. H. Han, H. N. Hwang, B. Kim, H. S. Kim, Y. D. Kim, and C. C. Hwang, “Pentacene as protection layers of graphene on SiC surfaces,” *Appl. Phys. Lett.*, vol. 95, no. 9, pp. 57–60, 2009.

[73] B. Long, M. Manning, M. Burke, B. N. Szafranek, G. Visimberga, D. Thompson, J. C. Greer, I. M. Povey, J. MacHale, G. Lejosne, D. Neumaier, and A. J. Quinn, “Non-covalent functionalization of graphene using self-assembly of alkane-amines,” *Adv. Funct. Mater.*, vol. 22, no. 4, pp. 717–725, 2012.

[74] M. C. Prado, R. Nascimento, L. G. Moura, M. J. S. Matos, M. S. C. Mazzoni, L. G. Cancado, H. Chacham, and B. R. a Neves, “Two-dimensional molecular crystals of phosphonic acids on graphene,” *ACS Nano*, vol. 5, no. 1, pp. 394–8, 2011.

[75] B. Li, A. V Klekachev, M. Cantoro, C. Huyghebaert, A. Stesmans, I. Asselberghs, S. De Gendt, and S. De Feyter, “Toward tunable doping in graphene FETs by molecular self-assembled monolayers,” *Nanoscale*, vol. 5, no. 20, pp. 9640–9644, 2013.

[76] L. Piot, A. Marchenko, J. Wu, K. Müllen, and D. Fichou, “Structural evolution of hexa-peri-hexabenzocoronene adlayers in heteroepitaxy on n-pentacontane template monolayers,” *J. Am. Chem. Soc.*, vol. 127, no. 46, pp. 16245–16250, 2005.

[77] B. Xu, S. Yin, C. Wang, X. Qiu, Q. Zeng, and C. Bai, “Stabilization effect of alkane buffer layer on formation of nanometer-sized metal phthalocyanine domains,” *J. Phys. Chem. B*, vol. 104, no. 45, pp. 10502–10505, 2000.

[78] C. Rohr, M. Balbás Gambra, K. Gruber, C. Höhl, M. S. Malarek, L. J. Scherer, E. C. Constable, T. Franosch, and B. A. Hermann, “Predicting the influence of a p2-symmetric substrate on molecular self-organization with an interaction-site model,” *Chem. Commun.*, vol. 47, no. 6, pp. 1800–1802, 2011.

[79] D. Grosso, “How to exploit the full potential of the dip-coating process to better control film formation,” *J. Mater. Chem.*, vol. 21, no. 43, pp. 17033–17038, 2011.

[80] G. Binnig, H. Rohrer, C. Gerber, and E. Weibel, “Surface studies by scanning tunneling microscopy,” *Phys. Rev. Lett.*, vol. 49, no. 1, pp. 57–61, 1982.

[81] C. Van Haesendonck, “Course material: scanning probe microscopy.” .

[82] L. C. Giancarlo, H. Fang, L. Avila, L. W. Fine, and G. W. Flynn, “Molecular photography in the undergraduate laboratory: identification of functional groups using scanning tunneling microscopy,” *J. Chem. Educ.*, vol. 77, no. 1, pp. 66–71, 2000.

[83] G. Binnig and H. Rohrer, “Scanning tunneling microscopy,” *IBM J. Res. Dev.*, vol. 44, no. 1–2, pp. 279–293, 2000.

[84] G. Binnig, C. Quate, and C. Gerber, “Atomic force microscope,” *Phys. Rev. Lett.*, vol. 56, no. 9, pp. 930–933, 1986.

[85] “File:AFM schematic (EN).svg - Wikimedia Commons.” [Online]. Available: http://commons.wikimedia.org/wiki/File:AFM_schematic_(EN).svg. [Accessed: 30-Apr-2015].

[86] N. Jalili and K. Laxminarayana, “A review of atomic force microscopy imaging systems: application to molecular metrology and biological sciences,” *Mechatronics*, vol. 14, pp. 907–945, 2004.

[87] Y. Seo and W. Jhe, “Atomic force microscopy and spectroscopy,” *Reports Prog. Phys.*, vol. 71, no. 1, 2008.

[88] R. Garcia and R. Pérez, “Dynamic atomic force microscopy methods,” *Surf. Sci. Rep.*, vol. 47, pp. 197–301, 2002.

[89] P. Blake, E. W. Hill, A. H. Castro Neto, K. S. Novoselov, D. Jiang, R. Yang, T. J. Booth, and A. K. Geim, “Making graphene visible,” *Appl. Phys. Lett.*, vol. 91, no. 6, 2007.

[90] A. C. Ferrari, J. C. Meyer, V. Scardaci, C. Casiraghi, M. Lazzeri, F. Mauri, S. Piscanec, D. Jiang, K. S. Novoselov, S. Roth, and A. K. Geim, “Raman spectrum of graphene and graphene layers,” *Phys. Rev. Lett.*, vol. 97, no. 18, 2006.

[91] E. Smith and G. Dent, *Modern Raman spectroscopy - a practical approach*. John Wiley & Sons, Ltd, 2004.

[92] C. N. Banwell and E. McCash, *Fundamentals of molecular spectroscopy*, 4th ed. 1994.

[93] L. M. Malard, M. A. Pimenta, G. Dresselhaus, and M. S. Dresselhaus, “Raman spectroscopy in graphene,” *Phys. Rep.*, vol. 473, no. 5–6, pp. 51–87, 2009.

[94] A. V. Klekachev, I. Asselberghs, C. Huyghebaert, M. Vanbel, M. A. Van der Veen, A. L. Stesmans, M. M. Heyns, S. De Gendt, and T. Verbiest, “SHG/2PF microscopy of single and multi-layer graphene,” in *Optical Processes in Organic Materials and Nanostructures*, 2012, vol. 8474.

[95] Y. Wang, Z. Ni, T. Yu, Z. X. Shen, H. Wang, Y. Wu, W. Chen, A. Thye, and S. Wee, “Raman studies of monolayer graphene : the substrate effect,” *J. Phys. Chem.*, vol. 112, no. 29, pp. 10637–10640, 2008.

[96] A. Das, S. Pisana, B. Chakraborty, S. Piscanec, S. K. Saha, U. V Waghmare, K. S. Novoselov, H. R. Krishnamurthy, A. K. Geim, A. C. Ferrari, and A. K. Sood, “Monitoring dopants by Raman scattering in an electrochemically top-gated graphene transistor,” *Nat. Nanotechnol.*, vol. 3, no. 4, pp. 210–215, 2008.

[97] M. Bruna, A. K. Ott, M. Ijäs, D. Yoon, U. Sassi, and A. C. Ferrari, “Doping dependence of the Raman spectrum of defected graphene,” *ACS Nano*, vol. 8, no. 7, pp. 7432–7441, 2014.

[98] J. E. Lee, G. Ahn, J. Shim, Y. S. Lee, and S. Ryu, “Optical separation of mechanical strain from charge doping in graphene,” *Nat. Commun.*, vol. 3, no. 1024, 2012.

[99] E. P. Gilbert, J. W. White, and T. J. Senden, “Evidence for perpendicular n-alkane orientation at the liquid/graphite interface,” *Chem. Phys. Lett.*, vol. 227, no. 4–5, pp. 443–446, 1994.

[100] S. L. Lee, Z. Yuan, L. Chen, K. S. Mali, K. Müllen, and S. De Feyter, “Forced to align: flow-induced long-range alignment of hierarchical molecular assemblies from 2D to 3D,” *J. Am. Chem. Soc.*, vol. 136, no. 11, pp. 4117–4120, 2014.

[101] D. M. Cyr, B. Venkataraman, G. W. Flynn, a. Black, and G. M. Whitesides, "Functional group identification in scanning tunneling microscopy of molecular adsorbates," *J. Phys. Chem.*, vol. 100, no. 32, pp. 13747–13759, 1996.

[102] W. Bao, G. Liu, Z. Zhao, H. Zhang, D. Yan, A. Deshpande, B. LeRoy, and C. N. Lau, "Lithography-free fabrication of high quality substrate-supported and freestanding graphene devices," *Nano Res.*, vol. 3, no. 2, pp. 98–102, 2010.

[103] O. Vazquez-Mena, L. Gross, S. Xie, L. G. Villanueva, and J. Brugger, "Resistless nanofabrication by stencil lithography: a review," *Microelectron. Eng.*, vol. 132, pp. 236–254, 2015.

Summary

Graphene is a two-dimensional material consisting of only carbon atoms arranged in a honeycomb network. Since its discovery in 2004, it has attracted worldwide interest from the scientific community, mainly because of its peculiar electronic properties. Many applications have been proposed of which graphene field effect transistors have been most intensively studied. However, integration of graphene in field effect transistors also elicits severe challenges**.** A major issue are the unstable device characteristics when operating graphene devices in ambient conditions. This has been attributed to the presence of atmospheric oxygen and water near the graphene sheet, causing charge transfer doping and forming charge traps. Therefore, a proper surface passivation layer of graphene is highly desired.

In this thesis, a self-assembled layer of pentacontane was investigated as a potential surface passivation layer. It was shown that a high quality pentacontane monolayer can be formed on graphite by dip-coating in strongly diluted toluene solutions. The potential of such a pentacontane layer to shield graphene from atmospheric dopants was investigated using Raman spectroscopy. Unfortunately, atmospheric doping could not be detected due to technical limitations, or because Raman spectroscopy is not sensitive enough for its detection. Electrical measurements on graphene field effect devices are therefore more desired, but the production of clean and working devices remains very challenging. In a second set of experiments, the robustness of a pentacontane layer against strong n-type dopants, in this case octadecylamine, was investigated. Raman measurements showed that the strong n-type doping effect exerted by octadecylamine on graphene can almost totally be precluded by passivating the graphene surface with a pentacontane layer. Moreover, it was concluded from the Raman data that the deposition of a C_{50} layer on graphene does not cause charge transfer doping, thereby preserving its pristine electronic properties.

Thus, in conclusion, the results in this thesis indicate that a homogeneous pentacontane film shows great potential to be used as a surface passivation layer for graphene, protecting it from surface charge transfer doping and preserving its pristine electronic properties. However, more experiments are needed to confirm the feasibility of this approach.

Samenvatting

Grafeen is een tweedimensionaal materiaal bestaande uit enkel koolstofatomen gerangschikt in een honinggraatstructuur. Sinds de ontdekking ervan in 2004, heeft het wereldwijd de aandacht getrokken van de wetenschappelijke gemeenschap, vooral vanwege zijn bijzondere elektronische eigenschappen. Vele toepassingen werden voorgesteld, waarvan grafeenveldeffecttransistoren meest intensief bestudeerd zijn. De integratie van grafeen in veldeffecttransistoren vormt echter ook ernstige uitdagingen. Een groot probleem zijn de onstabiele eigenschappen wanneer deze apparaten gebruikt worden onder natuurlijke omgevingscondities. Dit wordt toegeschreven aan de aanwezigheid van zuurstof en water in de buurt van het grafeenoppervlak, die dopering veroorzaken en ladingsvangst-centra vormen. Daarom is een geschikte oppervlaktepassiveringslaag voor grafeen zeer gewenst.

In dit proefschrift werd een zelf-geassembleerde laag van pentacontaan onderzocht als een potentiële oppervlaktepassiveringslaag. Er werd aangetoond dat een pentacontaanmonolaag van hoge kwaliteit gevormd kan worden op grafiet door onderdompelen van het substraat in sterk verdunde tolueenoplossingen. Het potentieel van dergelijke pentacontaanlaag om grafeen te beschermen tegen atmosferische dopeermiddelen werd onderzocht met behulp van Raman spectroscopie. Atmosferische dopering kon helaas niet worden waargenomen door technische beperkingen, of omdat Raman spectroscopie niet voldoende gevoelig is om dit waar te nemen. Elektrische metingen op grafeenveldeffecttransistoren zijn daarom gewenst, maar de productie van schone en werkende apparaten blijft zeer moeilijk. In een tweede set experimenten werd de robuustheid van een pentacontaanlaag tegen sterk n-doperende moleculen, nl. octadecylamine, onderzocht. Raman metingen toonden aan dat het sterke n-doperingseffect van octadecylamine op grafeen bijna volledig verhinderd kan worden door het passiveren van grafeen met een pentacontaanlaag. Bovendien kon uit de Raman data besloten worden dat het aanbrengen van een pentacontaanlaag op grafeen geen dopering veroorzaakt, waardoor de oorspronkelijke elektronische eigenschappen van grafeen behouden blijven.

Er kan dus geconcludeerd worden dat de resultaten in dit onderzoek aantonen dat een homogene pentacontaanlaag een groot potentieel vertoont om gebruikt te

worden als oppervlaktepassiveringslaag voor grafeen, waarbij het het grafeen beschermt tegen dopering en z’n oorspronkelijke elektronische eigenschappen bewaart. Er zijn echter meer experimenten nodig om de haalbaarheid van deze aanpak te bevestigen.

Appendices

Appendix 1: Effect of cleaning procedure on graphene flakes

In order to assess the effect of the cleaning procedure on the graphene flakes, two flakes on two different samples were characterized with Raman spectroscopy before and after the cleaning procedure. The changes in the Raman spectra are summarized in Table A1.1 and indicate a strong p-type doping effect. This p-type doping must be attributed to the annealing step, which results in an increased coupling of the graphene sheet to the underlying Si/SiO_2 substrate [62]. To evaluate strain levels before and after the cleaning procedure, a plot of the 2D peak position *vs.* the G peak position is given in Figure A1.1. For reference, a point corresponding to freestanding graphene has been added (taken from ref. [98]). This plot shows that before cleaning, the flakes are close to the value for freestanding graphene. However, after cleaning, it is clear that both p-type doping and compressive strain are induced. The induction of compressive strain must be attributed to a difference in thermal expansion coefficient between graphene and the underlying substrate [98]. The plot given in Figure A1.1 also demonstrates that after cleaning, the spread in the data points has increased. This increased spread is the result of the annealing effects occurring non-homogeneously over the area of the flake. In general, the center of the flakes is more p-doped than the edges, as demonstrated in Figure A1.2. A clear understanding of this non-homogeneity is still lacking. Finally, Figure A1.1 clearly demonstrates the initial flake-to-flake variation, which is always present after production of the flakes.

In short, it can be concluded that the forming gas anneal employed to clean the graphene flakes induces both p-type doping and compressive strain. Furthermore, these effects seem to occur non-homogeneously over the area of the flake, resulting in an increased spread in the data after annealing.

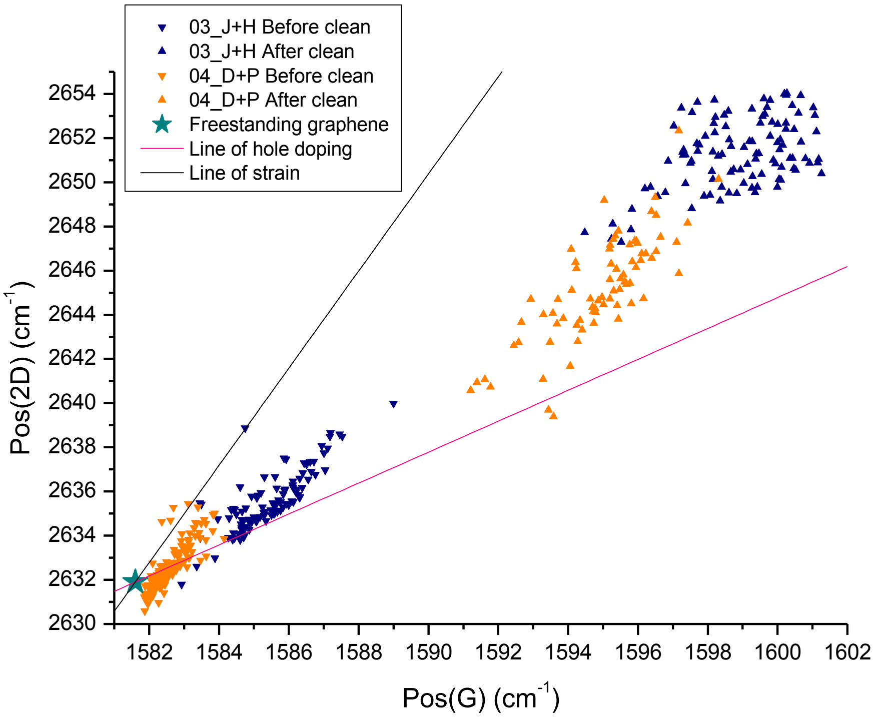

Figure A1.1. *Plot of Pos(2D) vs. Pos(G) for two different flakes before and after cleaning. The green star corresponds to a data point obtained for freestanding graphene (taken from ref.* [98]*). Data points were obtained from a Raman map on each flake.*

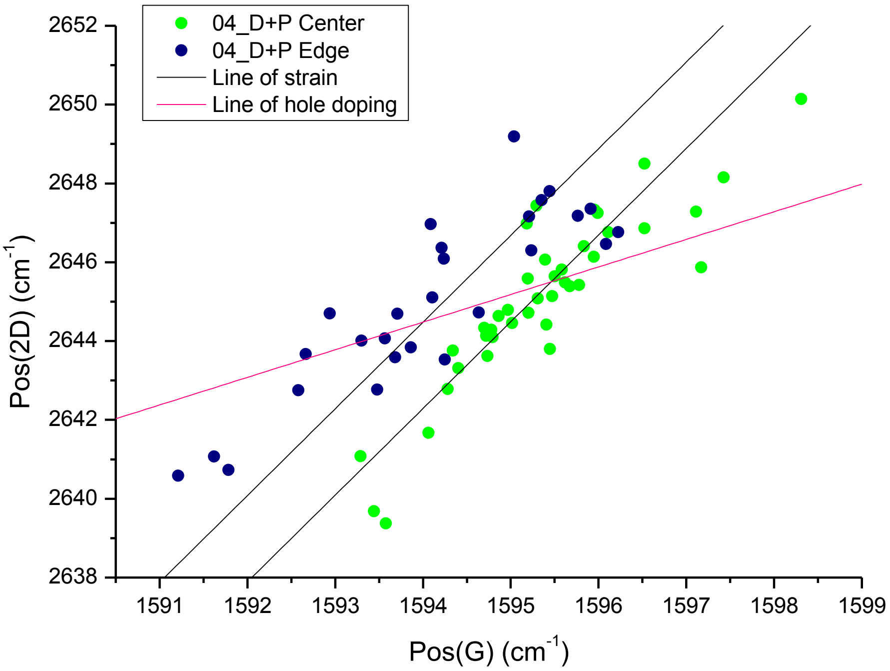

Figure A1.2. *Plot of Pos(2D) vs. Pos(G) for flake 04_D+P after cleaning. The data demonstrate that the center of the flake is more p-doped than the edge. Data points were obtained from a Raman map on the flake.*

Table A1.1. *Raman features of two different flakes before and after cleaning. The data are mean values deduced from a Raman map on each flake.*

Effect of cleaning procedure		**Pos(G) (cm^{-1})**	**FWHM(G) (cm^{-1})**	**Pos(2D) (cm^{-1})**	**FWHM(2D) (cm^{-1})**	**I(2D)/I(G) (-)**
Flake 03_J+H	*Before clean*	1585.4 ± 1.0	11.1 ± 0.6	2635.6 ± 1.4	26.7 ± 1.1	2.5 ± 0.3
	After clean	1598.9 ± 1.5	10.5 ± 1.0	2651.3 ± 1.6	31.2 ± 1.4	1.5 ± 0.2
Flake 04_D+P	*Before clean*	1582.5 ± 0.5	13.1 ± 0.3	2632.5 ± 0.9	26.0 ± 0.8	3.2 ± 0.3
	After clean	1594.9 ± 1.4	10.7 ± 0.8	2645.2 ± 2.4	30.5 ± 1.0	1.5 ± 0.1
Total	*Before clean*	1583.6 ± 1.6	12.4 ± 1.1	2633.6 ± 1.9	26.2 ± 1.0	3.0 ± 0.5
	After clean	1597.2 ± 2.4	10.6 ± 0.9	2648.7 ± 3.6	30.9 ± 1.3	1.5 ± 0.1

Appendix 2: Safety, health and environmental issues

Chemicals

- 1-Phenyloctane

This substance is considered to be little hazardous (E1). It is believed to cause long-term adverse effects on aquatic organisms. Therefore, appropriate measures of disposal should be taken. It should be disposed of as non-halogenated organic liquids (category 3).

H&P statements: H413, P273, P501

- Acetone

This substance is considered to be hazardous (E3). It is highly flammable and it should be kept at a safe distance from all sorts of ignition sources. It can cause severe eye irritation and can cause sleepiness and dizziness. Therefore, appropriate personal protective equipment[10] is required and the substance should only be handled in a fume hood. It should be disposed of as non-halogenated organic liquids (category 3).

H&P statements: H225, H319, H336, P210, P240, P242, P243, P261, P264, P271, P280, P312, P303+P361+P353, P304+P340, P305+P351+P338, P337+P313, P370+P378, P405, P403+P233, P403+P235, P501

- Ethanol

This substance is considered to be hazardous (E3). It is highly flammable and it should be kept at a safe distance from all sorts of ignition sources. It should be disposed of as non-halogenated organic liquids (category 3).

H&P statements: H225, P210, P243, P241, P242, P240, P280, P233, P303+P361+P353, P370+P378, P403+P235, P501

- Isopropylalcohol

This substance is considered to be hazardous (E3). It is highly flammable and it should be kept at a safe distance from all sorts of ignition sources. It can cause severe eye irritation and can cause sleepiness and dizziness. Therefore, appropriate personal

---

[10] Standard personal protective equipment includes: lab coat, safety goggles and disposable gloves.

protective equipment is required and the substance should only be handled in a fume hood. It should be disposed of as non-halogenated organic liquids (category 3).

H&P statements: H225, H319, H336, P210, P243, P241, P242, P240, P280, P261, P271, P264, P312, P304+P340, P303+P361+P353, P305+P351+P338, P337+P313, P370+P378, P403+P235, P403+P233, P405, P501

- IX 845

The specific contents of this substance are unknown. Therefore, special care must be taken when using it. It is highly flammable and it should be kept at a safe distance from all sorts of ignition sources. It can cause severe eye damage and can cause irritation to the respiratory system. Therefore, appropriate personal protective equipment is required and the substance should only be handled in a fume hood.

No H&P statements are available.

- Octadecylamine

This substance is considered to be moderately hazardous (E2). It can cause severe skin irritation and it can cause severe eye damage. Therefore, appropriate personal protective equipment is required. It is believed to cause long-term adverse effects on aquatic organisms. Therefore, appropriate measures of disposal should be taken. It should be disposed of as non-halogenated organic liquids (category 3).

H&P statements: H315, H318, H411, P264, P273, P280, P310, P321, P391, P302+P352, P305+P351+P338, P501

- OPD 5262

The specific contents of this substance are unknown. Therefore, special care must be taken when using it. It is harmful upon contact with the skin or upon ingestion. It can cause severe burning wounds and eye damage. It can cause damage to organs upon long-term or repeated exposure. Therefore, appropriate personal protective equipment is required and the substance should only be handled in a fume hood.

No H&P statements are available.

- Pentacontane

Insufficient data are available to classify this substance as hazardous. Therefore, special care must be taken when using it. It should be disposed of as non-halogenated organic liquids (category 3).

No H&P statements are available.

- Toluene

This substance is considered to be hazardous (E3). It is highly flammable and it should be kept at a safe distance from all sorts of ignition sources. It is believed to cause damage to the unborn child. It can be lethal upon ingestion or upon inhalation. It can cause damage to organs upon long-term or repeated exposure. It causes irritation of the skin. It can cause sleepiness or dizziness. Therefore, appropriate personal protective equipment is required and the substance should only be handled in a fume hood. It should be disposed of as non-halogenated organic liquids (category 3).

H&P statements: H225, H361d, H304, H373, H315, H336, P201, P202, P210, P243, P241, P242, P240, P280, P281, P260, P261, P271, P264, P309+P311, P314, P321, P304+P340, P332+P313, P302+P352, P303+P361+P353, P362, P301+P310, P331, P370+P378, P403+P233, P403+P235, P405, P501

Equipment

- STM

STM measurements are not considered to be dangerous when performed properly.

- AFM

AFM measurements are not considered to be dangerous when performed properly.

- Raman

Raman measurements involve the use of a class 3B laser. This laser is hazardous if the eye is exposed directly, but diffuse reflections are not harmful. In general, no protective eyewear is required, unless direct exposure is to be expected.

- Electrical characterization

Electrical measurements can cause electrocution. Therefore, a grounded wrist strap must always be worn when handling the tool.

MOLECULAR IMAGING AND PHOTONICS
Celestijnenlaan 200 F – bus 2404
3000 LEUVEN, BELGIË
tel. + 32 16 00 00 00
fax + 32 16 00 00 00
www.kuleuven.be